





## โครงการวิจัย

## การวิเคราะห์พลศาสตร์ของการไหลและการถ่ายเทความร้อน ในการไหลแบบปั่นป่วนในท่อที่มีลอนภายใน โดยใช้แบบจำลองแบบลาร์จเอ้ดดี้

โดย

ดร.อาภิรักษ์ หกพันนา

สิงหาคม 2563

## รายงานวิจัยฉบับสมบูรณ์

## โครงการการวิเคราะห์พลศาสตร์ของการไหลและการถ่ายเทความร้อน ในการไหลแบบปั่นป่วนในท่อที่มีลอนภายใน โดยใช้แบบจำลองแบบลาร์จเอ็ดดี้

ผู้วิจัย ดร.อาภิรักษ์ หกพันนา สังกัด มหาวิทยาลัยเทคโนโลยีพระจอมเกล้าธนบุรี

สนับสนุนโดยสำนักงานคณะกรรมการการอุดมศึกษา และสำนักงานกองทุนสนับสนุนการวิจัย (ความเห็นในรายงานนี้เป็นของผู้วิจัย สกอ. และ สกว. ไม่จำเป็นต้องเห็นด้วยเสมอไป)

### บทคัดย่อ

รหัสโครงการ: MRG5380279

ชื่อโครงการ : การวิเคราะห์พลศาสตร์ของการไหลและการถ่ายเทความร้อนในการไหลแบบปั่นป่วนในท่อที่มีลอนภายในโดยใช้

แบบจำลองแบบลาร์จเอ้ดดี้

ชื่อนักวิจัย: ดร.อาภิรักษ์ หกพันนา

อีเมลล์ : arpiruk.hok@eng.cmu.ac.th

ระยะเวลาโครงการ : 15 มีนาคม 2554 - 14 มีนาคม 2556 (เสร็จสิ้นโครงการ สิงหาคม 2563)

### บทคัดย่อ:

โครงการวิจัยนี้พัฒนาวิธีการในการรศึกษาการถ่ายเทความร้อนภายในท่อขรุขระด้วยวิธีการจำลองเชิงตัวเลข โดยในช่วงแรกของการวิจัย ได้มีการศึกษาการถ่ายเทความร้อนในท่อขรุขระด้วยการจำลองแบบลาร์จเอัดดี้ ระเบียบวิธีที่ใช้ประกอบด้วยวิธีไฟในต์โวลุ่มลำดับสูงและ วิธีอิมเมอร์สเบาดารี่ โดยได้ทำการศึกษาการไหลภายในช่องเรียบ ที่ค่าชมิดท์ 0.3-10 ที่ค่าเรย์โนลดส์ 5,600 การศึกษาพบว่าระเบียบวิธี ที่พัฒนาขึ้นมีความแม่นยำสูง เมื่อเทียบกับวิธีดั้งเดิม โดยการจำลองใหม่ สามารถใช้กริดที่หยาบขึ้นแต่ยังคงให้ผลเฉลยที่ใกล้เคียงกับ วิธี เดิม การศึกษาการไหลแบบปั่นป่วนภายในท่อขรุขระพบว่ามีความปั่นป่วนเพิ่มขึ้นอย่างมากเมื่อเทียบกับการไหลผิวเรียบ อย่างไรก็ตาม ในระหว่างการวิจัย ระบบคอมพิวเตอร์ของไทยกริด ไม่สามารถทำงานได้อย่างมีเสถียรภาพ ทำให้การจำลองขนาดใหญ่ที่มีค่าเรย์โนลดส์ และชมิดท์ สูงพอที่จะทำการตีพิมพ์ได้นั้น ไม่สามารถกระทำได้ ผู้วิจัยจึงได้เบนเป้าการวิจัยไปที่การพัฒนาแนวทางใหม่ในการจำลอง การไหลแบบปั่นป่วน ซึ่งในโครงการวิจัยนี้ได้พัฒนาระเบียบวิธีแบ่งวิยุต (discretization) วิธีใหม่ที่เรียกว่า Finite Surface method ซึ่ง วิธีนี้พบว่าในระเบียบวิธีปกติ จะมีความเร็วในการจำลอง สูงกว่า ชอฟท์แวร์วิจัยการไหลแบบปั่นป่วนดั้งเดิมถึง 28 เท่า และหากมีการปรับ ให้เหมาะสมในตัวโปรแกรมบางส่วน จะเพิ่มสมรรถนะเป็น 80 เท่า ซึ่งระเบียบวิธีนี้ จะช่วยให้การจำลองด้านการไหล และ การถ่ายเท ความร้อนแบบปั่นป่วนในประเทศไทยมีความเป็นไปได้ ถึงแม้ว่าจะมีทรัพยากรการคำนวณจำกัดก็ตาม

คำหลัก: การถ่ายเทความร้อนในท่อ, การจำลองลาร์จเอ้ดดี้, ระเบียบวิธีไฟในต์โวลุ่ม, ระเบียบวิธีลำดับสูง, ระเบียบวิธีไฟในต์เซอร์เฟส

### Abstract

Project Code: MRG5380279

Project Title: Analysis of flow dynamics and heat transfer inside corrugated tube by mean of Large-eddy simulation

Investigator : Dr.-Ing. Arpiruk Hokpunna E-mail Address : arpiruk.hok@eng.cmu.ac.th

Project Period: 15 March 2012 - 14 March 2014 (Project concluded in August 2020)

### Abstract:

This project developed a framework for heat transfer analysis in corrugated pipe. First, the research is directed at the simulation of heat transfer in corrugated pipe using large eddy simulation. The numerical method is a combination of fourth-order finite volume method and the immersed boundary method. The investigation of heat transfer in channel flow at Schmidt number 0.3 - 10 has been carried out at Reynolds number 5,600. The developed method is proven to be effective and efficient when compared with the literature. The simulation result of corrugated pipe show enhance turbulence. However, due to the limitation of computational resource and the unreliability of ThaiGrid infrastructure, a large-scale simulation could not performed and therefore a new method that can deliver an even better performance is needed to carried out turbulence research in Thailand. To this end, the second part of the research is redirected at the fundamental algorithm for fluid flow simulation. The novel discretization called Finite Surface Method (FSM) was developed. This method, in the standard setting, is found to be 28-times faster than a traditional research code. After optimization in some part of the code, the performance increases to 80-times. This new methods allows a turbulence research to be carried out using the limited computing resource we have in Thailand, whereas it would be impossible using the simulation technology prior to this research.

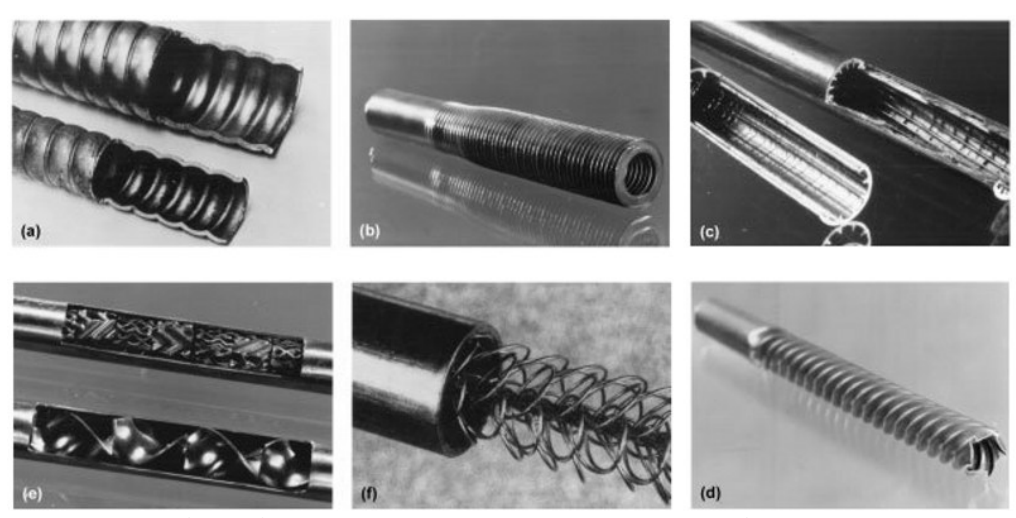
Keywords: heat transfer in pipe, large-eddy simulation, finite volume method, higher order method, finite surface method

## 1. บทสรุปผู้บริหาร (Executive Summary)

## 1. ความสำคัญและที่มาของปัญหา

การถ่ายเทความร้อนภายในท่อของอุปกรณ์แลกเปลี่ยนความร้อน (heat exchanger) เป็นปัญหาพื้นฐานที่มีความสำคัญต่ออุตสาหกรรม หลายๆชนิด อาทิเช่น เครื่องปรับอากาศ เครื่องทำความเย็น อุปกรณ์ถ่ายเทความร้อน อุตสาหกรรมการกลั่นน้ำมัน และอุตสาหกรรม อาหาร ในปี 2551 การส่งออกของอุตสาหกรรมเครื่องปรับอากาศและเครื่องทำความเย็นของไทยมีมูลค่ากว่า 140,000 ล้านบาท และมี การส่งออกเป็นอันดับสองของโลก การถ่ายเทความร้อนภายในท่อเป็นปัจจัยหนึ่งที่มีความสำคัญอย่างยิ่งในการกำหนดขนาดและ ประสิทธิภาพของอุปกรณ์แลกเปลี่ยนความร้อน หากการถ่ายเทความร้อนดังกล่าวสามารถทำได้อย่างมีประสิทธิภาพ ขนาดของอุปกรณ์ก็ จะสามารถลดลงได้ ซึ่งนำไปสู่การลดค่าใช้จ่าย และพลังงานที่ใช้ในการผลิต รวมไปถึงพลังงานที่ใช้ในการขับเคลื่อนสารทำความเย็น การ เพิ่มความสามารถในการถ่ายเทความร้อนภายในท่อจึงมีความสำคัญอย่างยิ่งต่อความสามารถในการแข่งขันของอุตสาหกรรมปรับอากาศ และเครื่องทำความเย็น และอุตสาหกรรมเกี่ยวเนื่องต่างๆ ของไทย

การเพิ่มความสามารถในการถ่ายเทการถ่ายเทความร้อนภายในท่อส่งสารทำความเย็นนั้นสามารถทำได้หลายแบบดังแสดงในภาพที่ 1 ซึ่ง ท่อที่มีลอนภายใน (corrugated pipe) มีการใช้วัสดุน้อยกว่าวิธีอื่นๆ และสามารถทำความสะอาดได้ง่ายกว่าท่อสอดไส้ตัวช่วยผสมแบบ สถิตย์ (static mixer insert) ทว่ารายงานในวารสารวิชาการแบบเปิดเกี่ยวกับการศึกษาท่อที่มีลอนภายในด้วยการทดลองนั้น ส่วนใหญ่ เป็นการทดลองในลักษณะการศึกษาภาพรวมของระบบ ทำให้ความรู้เกี่ยวกับกลไกสำคัญที่ช่วยเพิ่มความสามารถในการถ่ายเทความร้อน ยังไม่กระจ่าง การประยุกต์ใช้องค์ความรู้ที่มีอยู่กับท่อรูปแบบอื่นและสารทำความเย็นชนิดต่างๆจึงทำได้อย่างจำกัด



รูปที่ 1 รูปแบบท่อที่มีการเพิ่มความสามารถในการถ่ายเทความร้อน [4]: (a) ท่อที่มีลอนภายใน (corrugated pipe), (b) ท่อแบบมีครีบ ภายนอก (externally fin pipe), (c) ท่อแบบมีครีบภายใน(integral internal fin pipe), (d) ท่อแบบขูด (deep fluted pipe หรือ groove pipe), (e) ท่อสอดไส้ตัวช่วยผสมแบบสถิตย์ (static mixer insert), (f) ท่อแบบสอดด้ายโลหะ (wire-wound insert).

วิธีศึกษาอีกวิธีหนึ่งที่จะช่วยเพิ่มความเข้าใจในกลไกเหล่านี้ได้ ก็คือการใช้แบบจำลองทางคอมพิวเตอร์ซึ่งปัจจุบันยังมีการทำกันอยู่ใน วงจำกัด อีกทั้งบทความส่วนใหญ่ในวารสารวิชาการที่ใช้แบบจำลองทางคอมพิวเตอร์นั้นเป็นการจำลอง สมการของเรย์โนลดส์ (Reynolds Averaged Navier-Stokes equations: RANS) ซึ่งในระบบการไหลแบบปั่นป่วนสามมิติที่มีการไหลแบบซับซ้อน เช่น การ ไหลแบบแยกตัว (separation), บรรจบตัว (reattachment) และ หมุนวน (Recirculation) นั้น เป็นที่ทราบกันดีว่าผลการจำลองที่ได้ จาก RANS จะแตกต่างกันไปขึ้นอยู่กับ แบบจำลองการไหลแบบปั่นป่วนที่ใช้ และการตั้งค่าคงที่ของแบบจำลอง ทำให้เราไม่สามารถ

เชื่อถือผลลัพธ์ที่ได้จนกว่าจะได้มีการเลือกแบบจำลองและค่าควบคุมของแบบจำลองโดยการเปรียบเทียบกับการทดลอง จากนั้นจึง วิเคราะห์ผลลัพธ์ที่ได้ การขยายผลการจำลองเพื่อทำนายระบบอื่นๆ ที่ไม่ได้ทำการทดลองไว้จึงไม่สามารถเชื่อถือได้อย่างเต็มที่ งานวิจัยนี้มีจุดประสงค์เพื่อศึกษากลไกพื้นฐานและสร้างโมเดลทำนายสมบัติเชิงความร้อนของท่อที่มีลอนภายใน ที่สามารถประยุกต์ใช้กับ สถานการณ์ต่างๆที่กว้างขึ้น โดยวิธีการที่ใช้ศึกษาเป็นการแก้สมกาสมการของนาเวียร์สโตกส์ (Navier-Stokes equations) โดยใช้การ จำลองความปั่นป่วนแบบลาร์จเอ้ดดี้ (Large-Eddy Simulation: LES) ความรู้ที่ได้จากงานวิจัยนี้จะทำให้เราสามารถออกแบบท่อที่มีลอน ภายในให้มีประสิทธิภาพสูงขึ้น และช่วยลดระยะเวลาและขั้นตอนในการออกแบบท่อที่ชนิดนี้ในเงื่อนไขต่างๆ

### 2. วัตถุประสงค์งานวิจัย

- 2.1. เพื่อศึกษาพลศาสตร์ของไหลแบบแยกชั้น (laminar flow) และการไหลแบบปั่นป่วน (turbulent flow) ภายในท่อที่มีลอน ภายใน
- 2.2. เพื่อศึกษาความไม่เสถียร (instabilities) และ โครงสร้างภายในการไหล (flow structure) อันนำไปสู่การลดความหนาของ ชั้นขอบ (boundary layer) ซึ่งเป็นปัจจัยสำคัญในการเพิ่มความสามารถถ่ายเทความร้อนในท่อที่มีลอนภายใน
- 2.3. เพื่อศึกษากลไกการถ่ายเทความร้อนสู่ของไหลภายในท่อที่มีลอนภายใน แบบหนึ่งสถานะและแบบสองสถานะ
- 2.4. เพื่อพัฒนาระเบียบวิธีสำหรับการจำลองการไหลแบบปั่นป่วนที่มีประสิทธิภาพ

### 3. ระเบียบวิธีวิจัย

ระเบียบวิธีวิจัยสามารถแบ่งเป็น 4 ส่วนหลักๆได้ดังนี้

### 3.1.Problem formulation

เนื่องจากการถ่ายเทความร้อนภายในท่อ ที่เงื่อนไขการทำงานจริงประกอบไปด้วยกลไกที่ซับซ้อน โครงการนี้จึงวางแผนที่จะ ทำการศึกษาอย่างมีระบบเพื่อให้เข้าใจผลที่เกิดจากปัจจัยต่างๆได้อย่างถูกต้อง โครงการนี้ทำการศึกษาของไหลแบบนิวตัน (Newtonian fluid) และจำกัดการศึกษาอยู่ใน 3 ระบบ กล่าวคือ

- (i) การไหลแบบไม่ยุบตัวหนึ่งสถานะที่อุณหภูมิคงที่ (isothermal incompressible single phase flow)
- (ii) การไหลแบบไม่ยุบตัวหนึ่งสถานะแบบอุณหภูมิไม่คงที่ (non-isothermal incompressible single phase flow)
- (iii) การไหลไม่ยุบตัวแบบสองสถานะที่อุณหภูมิไม่คงที่ (non-isothermal incompressible two-phase flow) สมการควบคุมของระบบที่ (i) และ (ii) บน Cartesian coordinate สมการควบคุมของระบบที่ (i) และ (ii) ใน Cartesian coordinate ที่ใช้ในโครงการนี้คือ

$$\frac{\partial \rho u_i}{\partial x_i} = 0 \tag{1}$$

$$\frac{\partial \rho u_i}{\partial t} + \frac{\partial \rho u_j u_i}{\partial x_i} = \frac{\partial}{\partial x_i} \left( \mu \frac{\partial u_i}{\partial x_i} \right) - \frac{\partial p}{\partial x_i} + \rho g_i$$
 (2)

$$\frac{\partial \rho H}{\partial t} + \frac{\partial \rho H u_j}{\partial x_j} = \frac{\partial}{\partial x_j} \left( K \frac{\partial T}{\partial x_j} \right)$$
 (3)

ระบบที่ (iii) จากัดการศึกษาอยู่ที่ระบบของไหลสองสถานะที่ไม่ละลายปนกัน (immiscible fluids) และไม่มีการเปลี่ยนสถานะ ถึงแม้ว่าระบบดังกล่าวจะแตกต่างจากปรากฏการณ์ที่เกิดขึ้นจริงใน evaporator ของเครื่องทาความเย็น ระบบนี้จะเป็นก้าวแรกในการ สร้างแบบจาลองที่ใกล้เคียงความเป็นจริงมากขึ้น สมการควบคุมระบบที่ (iii) แบบเวกตอเรียลภายใต้สมมติฐานข้างต้นคือ

$$\begin{split} \frac{\partial \varphi_{k}}{\partial t} + \nabla (\mathbf{u}_{k} \varphi_{k}) &= 0 \\ \frac{\partial \rho_{k} \mathbf{u}_{k}}{\partial t} + \nabla (\rho_{k} \mathbf{u}_{k}) &= \varphi_{k} (-\nabla p + \nabla \cdot \tau) + \rho_{k} \mathbf{g} + (-1)^{k} \mathbf{F} \end{split} \tag{5}$$

$$\frac{\partial \rho_{\mathbf{k}} \mathbf{u}_{\mathbf{k}}}{\partial t} + \nabla(\rho_{\mathbf{k}} \mathbf{u}_{\mathbf{k}}) = \Phi_{\mathbf{k}} (-\nabla p + \nabla \cdot \tau) + \rho_{\mathbf{k}} \mathbf{g} + (-1)^{\mathbf{k}} \mathbf{F}$$
 (5)

$$\frac{\partial \Phi_{\mathbf{k}}}{\partial \mathbf{t}} + \nabla (\mathbf{u}_{\mathbf{k}} \Phi_{\mathbf{k}}) = \Phi(\nabla \mathbf{v}) \tag{6}$$

$$\begin{split} &\frac{\partial \varphi_{k}}{\partial t} + \nabla (\boldsymbol{u_{k}} \varphi_{k}) = \varphi(\nabla \boldsymbol{v}) \\ &\frac{\partial \rho_{k} E_{k}}{\partial t} + \nabla \big(\boldsymbol{u_{k}} (\rho_{k} E_{k} + \boldsymbol{p}) \big) = \nabla (\boldsymbol{K_{k}} \nabla T) + \boldsymbol{F} \cdot \big(\boldsymbol{u_{mod(k+1,2)}} - \boldsymbol{u_{k}} \big) \end{split} \tag{6}$$

$$\mathbf{v} = \frac{1}{2} \sum_{k=1}^{2} \mathbf{u_k} \tag{8}$$

สมการข้างต้นบรรยายถึงการอนุรักษ์ของปริมาณเชิงฟิสิกส์ สี่ประการคือ มวล (4) แรงดล (5) สัดส่วนปริมาตร(volume fraction) (6) และพลังงาน (7) สมการที่ (8) เป็นการคานวณหาค่าความเร็วเฉลี่ยที่ใช้ในสมการที่ (6) F ในคือแรงที่เกิดคือปฏิสัมพันธ์ระหว่างสารทั้งสอง สถานะที่เกิดขึ้น ณ ผิวแบ่งระหว่างสถานะ (phase interface) k คือดัชนีสถานะ 0 คือ ของเหลว และ 1 คือ ก๊าซ

ระบบที่ (iii) จำกัดการศึกษาอยู่ที่ระบบของไหลสองสถานะที่ไม่ละลายปนกัน (immiscible fluids) และไม่มีการเปลี่ยนสถานะ ถึงแม้ว่าระบบดังกล่าวจะแตกต่างจากปรากฏการณ์ที่เกิดขึ้นจริงใน evaporator ของเครื่องทำความเย็น ระบบนี้จะเป็นก้าวแรกในการ สร้างแบบจำลองที่ใกล้เคียงความเป็นจริงมาก

### 2. Solution methodology

ในระบบที่ (i) มีการตั้งสมมติฐานว่าค่าความหนาแน่นและอุณหภูมิมีค่าคงที่ ในระบบที่ (ii) สมบัติดังกล่าวสามารถเปลี่ยนค่าได้ ผู้ ดำเนินโครงการจะใช้โปรแกรม MGLET [22] เพื่อการจำลองระบบที่ (i) และ (ii) โดยในส่วนของไหลนั้นจะประยุกต์ระเบียบวิธีที่ผู้ดำเนิน โครงการประดิษฐ์ขึ้น [23] ซึ่งระเบียบวิธีดังกล่าวสามารถทำงานได้กว่าระเบียบวิธีพื้นฐานถึงสิบเท่า ณ ความถูกต้องของผลเฉลยที่ ใกล้เคียงกัน ในโครงการนี้ผู้ดำเนินโครงการจะทำการเพิ่มเติมความสามารถในการจำลองการเปลี่ยนแปลงของค่าความหนืดด้วยการใช้ ฟังก์ชันในรูป \mu=f(T) และผลจากการเปลี่ยนอุณหภูมิของจะจำลองด้วย Bounissque approximation

เนื่องจากปัญหาที่ต้องการศึกษาสำหรับระบบทั้งสองข้างต้นนั้น เป็นการไหลที่ค่าเรย์โนลดส์ค่อนข้างสูง และต้องใช้กริดจำนวนมาก ซึ่ง กริดชนิดที่ไม่มีโครงสร้าง (unstructured grid) ที่สามารถเข้ารูปกับวัตถุซับซ้อนได้ดี จึงไม่ใช้ตัวเลือกที่เหมาะสม เนื่องจากกริดชนิดนี้ ใช้หน่วยความจำต่อกริดสูงและมีการเข้าถึงหน่วยความจำได้ช้า ในโครงการนี้จะใช้ Cartesian grid กับ Immersed Boundary Method [24] ซึ่งมีความแม่นยำเป็นอันดับสองในการแสดงรูปร่างของวัตถุ สำหรับระบบที่ (iii) นั้นจะใช้ OpenFOAM ในการจำลองโดยใช้ วิธี Volume of Fluid [25] และเนื่องจากโปรแกรมนี้ยังทำงานได้ค่อนช้า ปัญหาที่ศึกษาในขั้นนี้จะจำกัดอยู่ที่การไหลที่เลขเรย์โนลด์ไม่สูงนัก และจะมีการใช้ GPGPU มาเป็นตัวช่วยในการคำนวณ

### 3. Validation

เพื่อตรวจสอบความแม่นยำของระเบียบวิธีที่พัฒนาขึ้น software จะได้รับการทดสอบเปรียบเทียบกับ ข้อมูลในวารสารวิชาการที่ เกี่ยวข้องกับการไหลภายในท่อที่มีการถ่ายเทความร้อน เช่น [Kawamura; INT J HEAT FLUID FL 19(5):482] และ ฐานข้อมูลของ มหาวิทยาลัยโตเกียว http://www.thtlab.t.u-tokyo.ac.jp/DNS/dns database.html ซึ่งผลที่ได้จากการเปรียบเทียบจะแสดงถึงความแม่นยำของระเบียบวิธีที่พัฒนาขึ้น และถ้าผลการจำลองคลาดเคลื่อนไปจากข้อมูลอ้างอิง มาก ผลจากการตรวจสอบนี้จะสามารถนำมาใช้ในการค้นหาข้อผิดพลาดที่อาจเกิดขึ้นในขั้นตอนต่างๆ ของการพัฒนาโปรแกรม

### 4.Analysis

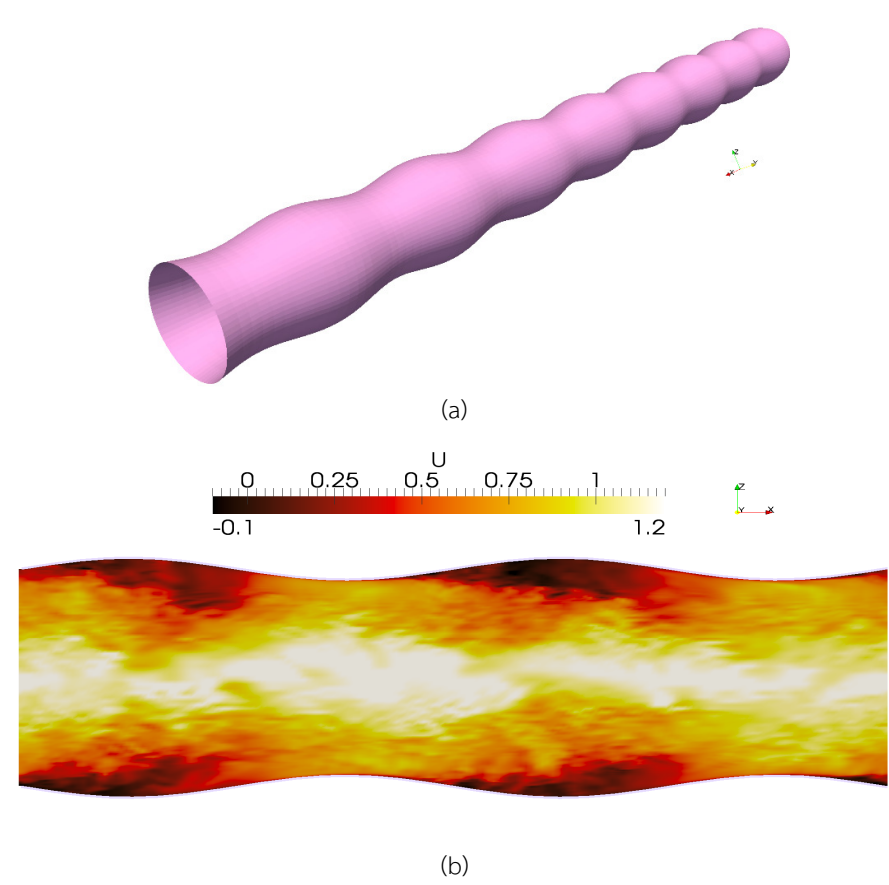
ในการวิเคราะห์ผลที่ได้จากการจำลองนั้น จะมีการศึกษาสถิติต่างๆของการไหลตั้งแต่สถิติลำดับที่หนึ่ง ถึงลำดับที่สี่ (mean, standard deviation, skewness และ flatness) จะมีการวิเคราะห์หากลไกและตำแหน่งที่ก่อให้ความปั่นป่วนโดยวิเคราะห์จาก ค่าการ สร้างความปั่นป่วน (turbulent production) สภาวะของการไหลแบบปั่นป่วนนั้นจะวิเคราะห์โดยใช้ Lumley's diagram และโครงสร้าง และองค์ประกอบของการไหลแบบต่างๆจะวิเคราะห์ด้วย Proper orthogonal decomposition ซึ่งจำเป็นต้องมีการเก็บข้อมูล timeseries snapshot ของสถานะของการไหลเป็นจำนวนมาก ข้อมูลที่สร้างขึ้นเพื่อการวิเคราะห์นี้จะถูกเก็บอยู่ใน Raid array system ที่จะ ทำการซื้อวัสดุมาประกอบเพิ่มใส่ในคอมพิวเตอร์ที่ภาควิชามีอยู่

### 3. ผลการวิจัย

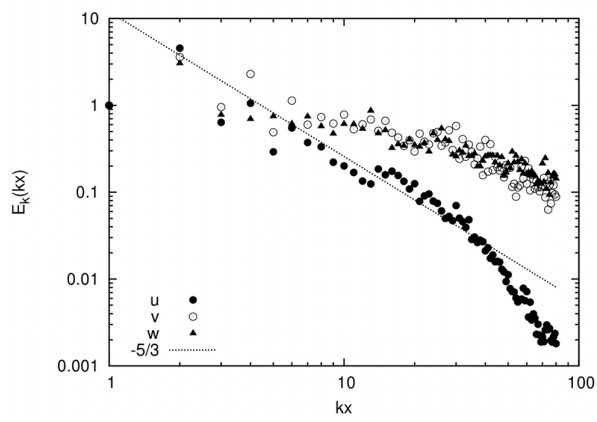
### 3.1 การวิจัยในแนวทางการถ่ายเทความร้อนในท่อขรุขระ

## 3.1.1.การพัฒนาระเบียบวิธีเชิงตัวเลขเพื่อจำลองการการไหลในรูปทรงที่ซับซ้อน : ในหัวข้อการวิจัยนี้

ผู้ดำเนินโครงการได้ร่วมมือกับ Prof.Manhart แห่งมหาวิทยาลัยเทคโนโลยีมิวนิก และ Dr.Schwertfirm จาก บริษัท Manhart-Kreuzinger Turbulenz เพื่อพัฒนาการถ่ายเทความร้อนในการไหลภายในรูปทรงที่มีความซับซ้อน ซึ่งในขั้นตอนสุดท้ายจะต้องประยุกต์ รวมวิธีในจุดประสงค์ที่ 2 เข้ากับการระเบียบวิธีที่พัฒนาขึ้นโดย Dr.Schwertfirm ซึ่งวิธีที่พัฒนาขึ้นจะใช้ศึกษาท่อกดแบบไซน์ ที่กำหน ด้วยสาการ  $R_0(1+\varepsilon\sin(nx))$  โดยผลการจำลองเพียงการไหลเพียงอย่างเดียวแสดงในรูปที่ 1 ซึ่งแสดงให้เห็นส่วนแกนของการ ไหลที่ศูนย์กลางท่อ การปะทะที่ยอดเนิน (จุดที่เส้นผ่าศูนย์กลางท่อเล็กที่สุด) และ(จุดที่เส้นผ่าศูนย์กลางท่อเล็กที่สุด) การไหลแบบแยกตัว และการไหลเข้าบรรจบ (flow separation and reattachment) จากการศึกษาสเปกตรัมของพลังงานจลน์ (รูปที่ 2 ) พบว่าการจำลอง ยังจำเป็นต้องใช้กริดที่ละเอียดขึ้น เนื่องจากกราฟของ ความเร็วแนวขวาง (v และ w) ไม่มีส่วนที่ เป็น dissipation range เนื่องจากกราฟ มีลักษณะ ที่แบบกว่าที่ควรจะเป็น



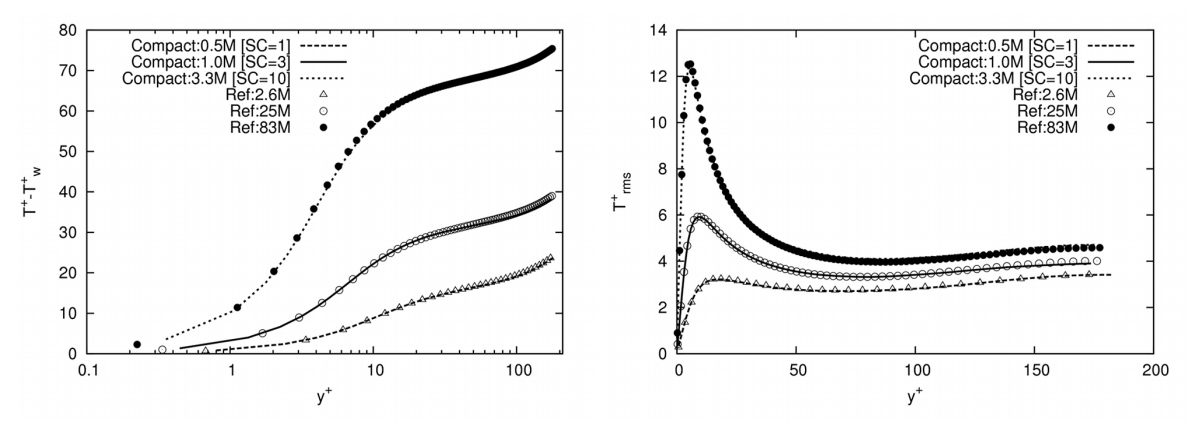
รูปที่ 2 รูปทรงท่อลอนที่ใช้ศึกษา (a) และภาพนิ่งของความเร็วจากการจำลองในท่อลอน (b)



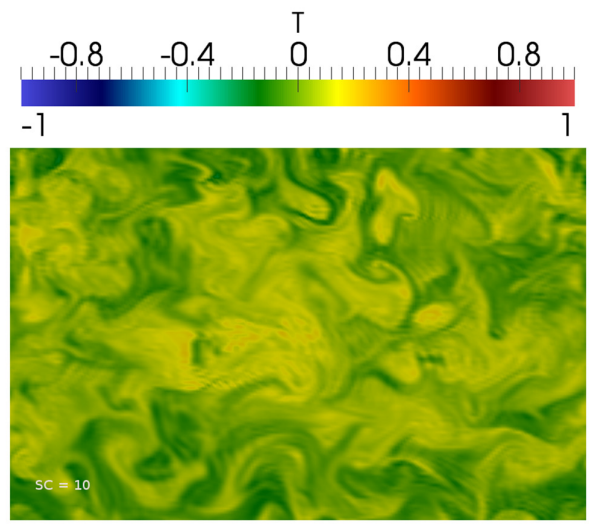
รู**ปที่** 3 สเปกตรัมของพลังงานจลน์ในแกน x, y และ z (u,v และ w ตามลำดับ)

3.1.2.การพัฒนาระเบียบวิธีเชิงตัวเลขสำหรับการถ่ายเทมวลและความร้อนบนกริดแบบเยื้องตัว : ในการหัวข้อการวิจัยนี้ ผู้ดำเนินการวิจัย ได้ประยุกต์ compact fourth-order finite volume method ของ [Kobayashi, Journal of Computational Physics 156(1999)] เข้ากับ Divergence-free convective fluxes ของ [Hokpunna, Journal of Computational Physics 229(2010)] ทำให้ได้วิธีเชิง ตัวเลขสำหรับ ซึ่งมีความแม่นยำอันดับสี่ (fourth-order) ในการจำลองการถ่ายเทมวลและความร้อน อาจจำเป็นต้องใช้สนามความเร็วที่มี ความแม่นยำมากกว่าการจำลองการไหลเพียงอย่างเดียว ในโครงการวิจัยนี้ได้มีการพัฒนาระเบียบวิธี Multigrid สำหรับ higher-order method โดยการใช้ Strongly Implicit Procedure ของ Stone [SIAM Journal of Numerical Analysis 5(1968)] เป็น Smoother และ ใช้กระบวนการ injection สำหรับการถ่ายเทข้อมูลไปยังกริดหยาบ และ second-order interpolation สำหรับการถ่ายเทข้อมูล ไปกริดละเอียด

3.การศึกษาการไหลแบบไม่ยุบตัวที่อุณหภูมิคงที่: ระเบียบวิธีที่พัฒนาขึ้นในวัตถุประสงค์ที่สองได้นำมาใช้เพื่อศึกษาการไหลระหว่างช่อง ซึ่งผู้วิจัยได้ทำการศึกษาการไหลแบบ passive transport ระหว่างช่อง (channel flow) ด้วยวิธี Direct Numerical Simulation ซึ่งทำการแก้สมการควบคุม (สมการนาเวียร์สโตกส์ และ สมการการทรงมวลของสารที่อยู่ในของไหล) โดยจำกัดการศึกษาที่เลขชมิดท์ ตั้งแต่ 1 ถึง 10 ซึ่งการจำลองการถ่ายเทมวลด้วยระเบียบวิธีที่พัฒนาขึ้นในโครงการนี้ มีความสามารถเทียบเคียงกับระเบียบวิธีอื่นๆ ที่ใช้อยู่ใน ปัจจุบัน รูปที่ 1 แสดงการเปรียบเทียบระหว่างผลการศึกษาในงานวิจัยนี้กับข้อมูลอ้างอิงในวารสารวิชาการ [Schwertfirm, International Journal of Heat and Fluid Flow 28(2007)] ในการศึกษานี้ การจำลองที่เลขชมิดท์ 1, 3 และ 10 นั้นใช้จำนวนกริด ในการจำลอง 0.5, 1 และ 3.3 ล้านกริด ตามลำดับ ซึ่งให้ผลเช่นเดียวกันกับการจำลองของ Schwertfirm ที่ใช้ 2.6 ล้านกริด, 24 ล้า นกริด และ 83 ล้านกริด โดยค่าเฉลี่ยของการไหล และ ค่า rms ของความแปรปรวนแสดงในรูปที่ 4 และรูปนี้แสดงให้เห็นว่าระเบียบวิธี ที่พัฒนาขึ้น สามรถทำนาย ค่าเฉลี่ยของความเข้มข้น ได้อย่างแม่นยำ ถึงแม้จะใช้กริดน้อยกว่า 4 -20 เท่า รูปที่ 5 แสดงโครงสร้างของ การไหลผ่านทางภาพถ่าย ณ เวลาหนึ่ง (snapshot) ในช่วงที่ทำการจำลอง



รูปที่ 4 ค่าเฉลี่ย(รูปซ้าย) และ ค่าเบี่ยงเบนมาตรฐานของ ความเข้มข้น เปรียบเทียบกับผลการจำลองของ Schwertfirm et. al. (International Journal of Heat and Fluid Flow 28(2007))



**รูปที่ 5** คอนทัวร์ของความเข้มข้น ที่ 0.8H จากพื้นลองของช่อง ของการจำลองที่ค่าชมิดท์ 10

### 3.2 การวิจัยในแนวทางใหม่ด้านการพัฒนา วิธีการดิสครีไตเซชันของสมการอนุพันธ์ด้วยวิธีไฟในต์เซอร์เฟส

จากการทำการวิจัยใน ช่วง 18 เดือนของโครงการนั้น ผู้วิจัยได้ใช้ทรัพยากรการคำนวณของไทยกริด ซึ่ง มีปัญหาด้านความเสถียรภาพของ ระบบอยู่เสมอ ทำให้ไม่สามารถทำการจำลองระยะยาวได้ และ การจำลองการไหลที่เลขชมิดท์สูง พอที่จะเป็นที่สนใจในวงวิชาการ นั้น จำเป็นต้องใช้ทรัพยากรที่ สูงเกินกว่าไทยกริดทำได้จริง โดยระบบคอมพิวเตอร์ที่ไทยกริดสามารถใช้งานได้จริงเพง 32 แกนการคำนวณ จาก ทั้งหมด 800 แกน โดยการจำลองที่มีค่าชมิดท์ และ ค่าเรย์โนลดส์ สูงพอจะเป็นที่สนใจ นั้น จำเป็นต้องใช้ 128 แกนการคำนวณ เป็นเวลาต่อเนื่อง กัน 1 -2 เดือน และการทำการวิจัยที่เลขเรย์โนลดส์และเลขชมิดท์ต่ำ นั้น ไม่สามารถตีพิมพ์ ในวารสารชั้นนำได้ โดยง่าย และการจำใช้งานระบบไทยกริด ไม่สามารถทำการจำลองได้ต่อเนื่อง ทำให้ไม่สามารถ เก็บข้อมูลสถิติการไหลได้ และผู้วิจัยไม่ สามารถหาซุปเปอร์คอมพิวเตอร์ที่สามารถทำการจำลองขนาดใหญ่ได้ และเป็นอุปสรรคส่งผลทำให้การวิจัยไม่สามารถทำเนินต่อไปได้

ดังนั้น เพื่อการการวิจัยด้านการไหลแบบสองเฟส และการถ่ายเทความร้อนด้วยการจำลองเชิงตัวเลขสามารถเป็นไปได้ในข้อจำกัดทาง ทรัพยากรการคำนวณในประเทศไทย ผู้วิจัยได้เน้นการวิจัยไปในทิศทางที่ 2 เพื่อพัฒนาเทคโนโลยีด้านการจำลองชนิดใหม่เพื่อ ให้การ แก้ปัญหาการจำลองเชิงพลศาสตร์ของไหลรวดเร็วและมีประสิทธิภาพมากยิ่งขึ้น โดย ระเบียบวิธี และ กระบวนการแบ่งย่อยกายภาพ (physical discretization) ที่พัฒนา ขึ้นใหม่นี้เรียกว่า finite surface method (FSM) โดย การคิดค้นระเบียบวิธีนี้ใช้เวลา นาน เป็น

สาเหตุให้การ ดำเนินการโครงการวิจัยนี้ ใช้เวลานานกว่าที่กำหนดไว้ อย่างไรก็ตาม วิธีที่คิดขึ้นใหม่นี้ มี ศักยาภาพสูงมากซึ่งมีศักยภาพ สามารถพัฒนาต่อไปในสาขาอื่นๆ ได้ ในระดับใกล้เคียงกับ Finite difference, Finite Volume และ Finite Element method รายละเอียดเชิงลึกนั้น สามารถอ่านได้ในบทความวิชาการ Hokpunna et. al. 2020 ในภาคผนวก โดยในส่วนเนื้อหาของรายงานนี้ จะ กล่าวถึงแนวคิด และ ผลการวิจัย โดยสังเขป

### 3.1.1 Concept

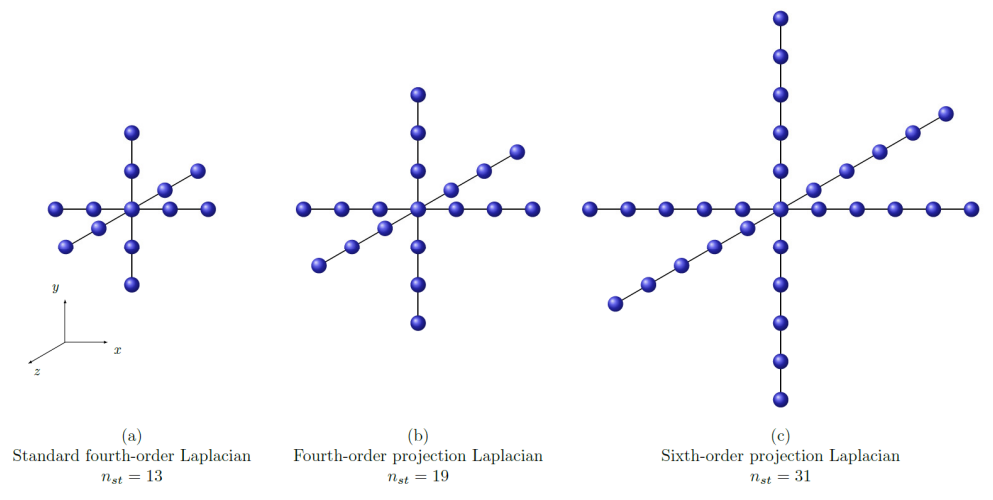
Finite volume (FVD) and finite difference (FDD) discretizations have been important instruments for turbulence research. Direct Numerical Simulation (DNS) using these two discretizations helped to achieve a better understanding of turbulence. However, even with the current fastest supercomputers, the complexity of the turbulent flows is still too much for us to tackle it directly, especially in the industry-relevant scales, prompting the 15 need for more efficient approaches. This can be done in many ways such as i.upgrading the numerical schemes in the discretization and ii.develop a new discretization. The first direction has been researched intensively in the past three decades, numerous higher-order methods have been developed among others. The second approach is rarely attempted. A new discretization may enable more flexibility such as the Finite 20 Element Method or provide more robustness such as the Discontinuous Galerkin Method(DGM), but they are not necessarily more efficient.

In the first direction, the computing cost increases as a linear function with the convergence order of the method, but the advantage from the grid density reduction is a quartic function (including the time-step). This advantage is well observed in convection-diffusion problems [5, 9, 10]. On the other hand, the early applications of higher-order methods to the Navier-Stokes equations (NSE) report notable improvements in the higher-order statistics and the energy spectra in turbulent flow simulations, but the improvements in the mean fields are almost negligible. One of the reasons is because the higher-order schemes are applied only to the momentum-conservation equation, but the approximations of mass and pressure fluxes are left at second-order. The enforcement of the mass-conservation and the solution of the new pressure, are usually done by the projection method. First the momentum equation is integrated in time and the result is treated as the provisional velocity. The divergence of this velocities is then checked. If the field is not divergence-free, the projection method then solves the Poisson equation formed by the multiplication of the discrete divergence and the discrete gradients. This requirement complicates the implementation of the higher-order method significantly requirement complicates the implementation of the higher-order method significantly requirement complicates the implementation of the higher-order method significantly.

Later, it has been widely accepted that an n-th order NSE solver must use an n-th order method in the approximation of the mass flux and pressure force . This translates to a special form of the Laplacian in the Poisson equation for the pressure. Figure 6 compares a fourth-order (19-point) and a sixth-order (31-points) projection Laplacians to an explicit fourth-order Laplacian (13-point). It can be seen that, this requirement greatly increases the cost of higher-order methods. Specifically, the cost ratio between the projection and the explicit Laplacians, at the same order of accuracy is

$$R = \frac{12n - 11}{6n + 1}$$

Thus, the projection Laplacian is asymptotically twice more expensive than the standard Laplacian. The extra large stencil is a consequence of the projection method. The projection Laplacian could be a full matrix if one of the discrete operators is implicit.

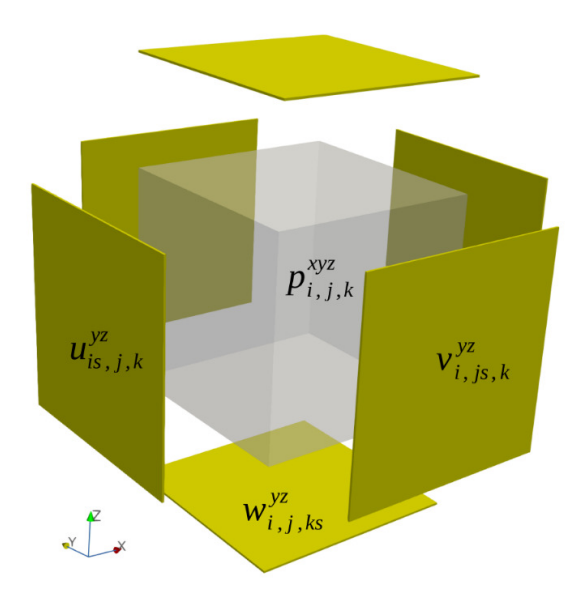


รูปที่ 6 A standard fourth-order approximation stencil of the Laplacian (a). The standard fourth- and sixth-order projection stencils needed by FDM and FVM on staggered grid (b and c). The proposed method can deliver a sixth-order convergence rate using the left stencil.

Furthermore, during the development of higher-order NSE solvers, the performance gains of higher-order methods on the collocated grids are small, unlike the staggered grid counterpart. On staggered grids, the compact fourth-order scheme is very accurate and it is ten times faster than the second-order scheme, at the same level of accuracy. The reason why higher-order NSE solvers work very well on staggered grids is investigated in . It is concluded that the advantage does not belong to the mathematical discretization of the NSE, but it belongs to the discretization of the physical domain and the arrangement of the flow variables which allow a better calculation of the mass conservation. Thus, if we step back and consider that FVD converts the continuous physical domain into a collection of interconnected volumes (or cells) while FDD discretizes the domain into a set of isolated points in space. Then, it is natural that we can also define the discrete space as a set of surfaces. In this paper, we present a new discretization decomposing the physical domain this way. We call it finite surface discretization (FSD). This approach has superior mass conservation properties compared to the existing methods and greatly reduces the complexity of the pressure treatment mentioned previously. Figure 7 shows the exploded control surfaces of the three velocities while the 80 pressure is kept as a volume in the transparent cube. The discrete physical domain where the velocities live is now just the outer shell of the pressure. The integral of the velocity divergence on this cell can be computed exactly by summing the respective fluxes on these faces. Setting up a spatial discretization this way renders the discrete mass conservation equation exact. The only equation left to approximate is the momentum conservation.

The newly developed discretization possesses the following unique properties

- It delivers the exact discrete mass conservation.
- The computation of the exact mass balance costs the same as in other second-order schemes.
- It enjoys the half-a-cell advantage in the pressure gradient calculation similar to staggered grid arrangement.
- It eliminates the extended stencil needed by the projection method.
- It can use a lower order approximation for the pressure and still support higher-order momentum approximations.



รูปที่ 7 Exploded view of the controlled-surfaces where FSD defines the velocities. Each surface contains only one normal velocity

### 3.1.2 Accuracy and the performance of the method

In this section, we verify the accuracy of the finite surface method using four standard test cases and focus on how the pressure treatment affects the overall accuracy of the compact sixth-order FSM. The convection and the viscous terms are approximated by sixth-order schemes in all test cases and the time-integration is third-order low-storage Runge-Kutta (RK). The approximations of the pressure gradient considered here are (i). the fourth-order explicit (PE4), (ii). the compact fourth-order (PCO4), and (iii). the compact sixth-order (PCO6) methods. The Poisson equations are solved by a direct FFT solver using a transfer function listed in Table 2. In the domain having both periodic and non-periodic, the eigendecomposition is employed where we solve a banded matrix for each pair of xy-eigenmode. All the simulations in two dimensions are computed with the sixth-order nonlinear correction without any filtering process. The method is implemented on MGLET developed at Technische Universität München where the principal investigator worked and helped develop the code.

First a Taylor-Green vortex (TGV) flow is used to investigate the accuracy of the individual components of the momentum equations including the pressure. Next, a double shear layer (DBL) flow is used to verify the convergence in a fully nonlinear flow. The boundary closures are then evaluated using an instability in plane channel flow a and

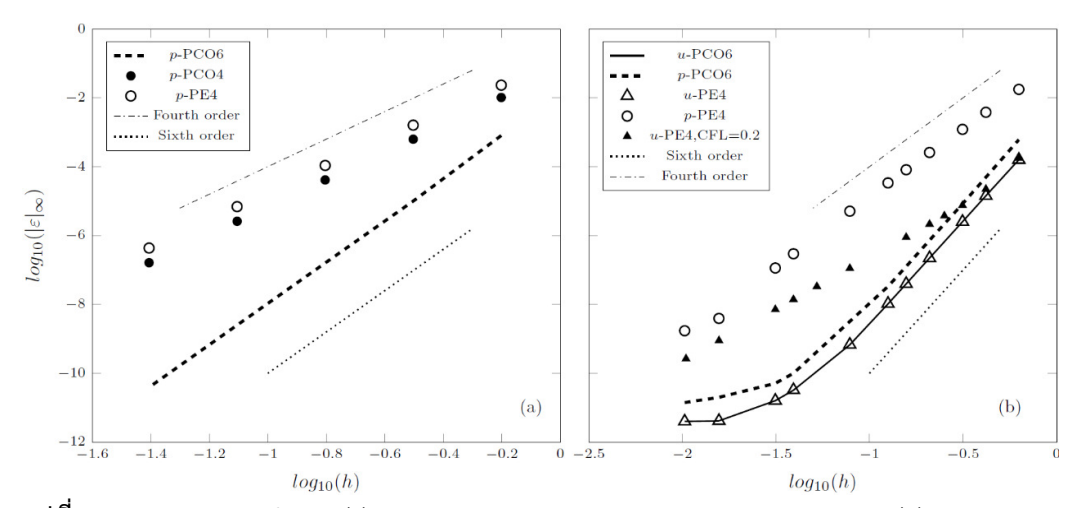
lid-driven cavity flow. The divergence error (div  $\cdot$  Lref /Uref ) is in the range of 1E-15 for the simple TGV flow and the instabilities in plane channel flow. In the DBL problem, the divergence is in the order of 1E-14 on the coarsest grid and 1E-13 on the finest grid (N =  $512^2$ ). In the lid-driven cavity flow, an iterative solver is used and the divergence is kept in the vicinity of 1E-11.

### Taylor-Green Vortex

In the first test, we use a family of Taylor-Green vortex flow to check the accuracy of the scheme. The initial condition for each test is prescribed by the equations below:

$$\begin{split} u(x,y,t,Re) &= c_x - \cos(x - c_x t) \sin(y) e^{\frac{-2t}{Re}} \\ v(x,y,t,Re) &= c_y + \sin(x - c_y t) \cos(y) e^{\frac{-2t}{Re}} \\ p(x,y,t,Re) &= -\frac{1}{4} (\cos(2(x - c_x t)) + \cos(2(y - c_2 t))) e^{\frac{-2t}{Re}} \end{split}$$

First, we check the accuracy of the pressure treatment using the stationary inviscid TGV: wit Cx = Cy = 0 by initializing the velocities with exact values but using the wrong pressure. The cell-averaged pressure value is replaced by the pointwise value at the cell center. This mimics the situation when the velocity field is accurately known, but the pressure is less accurate or unknown. This tests the ability to recover the pressure by the different treatments mentioned previously. All the approximations of the convection and diffusion terms are computed with full sixth-order except for the pressure gradient. We perform just a single time integration to check the recovered pressure. The convergence curves of the new pressures indicate that the explicit fourth-order treatment (PE4) is the least accurate (Fig.8(a)), as expected. Its error is 2.6 times larger than the compact fourth-order (PCO4) while the sixth-order.



รูปที่ 8 Convergence of FSM: (a) the initial projected pressure in the inviscid TGV, (b) the convergence of u and p in the traveling TGV at  $t = 2\pi$ . Every simulation is performed with CFL = 0:013 except for the addition test stated in the graph (CFL = 0:2). The y-axis is shared by both graphs.

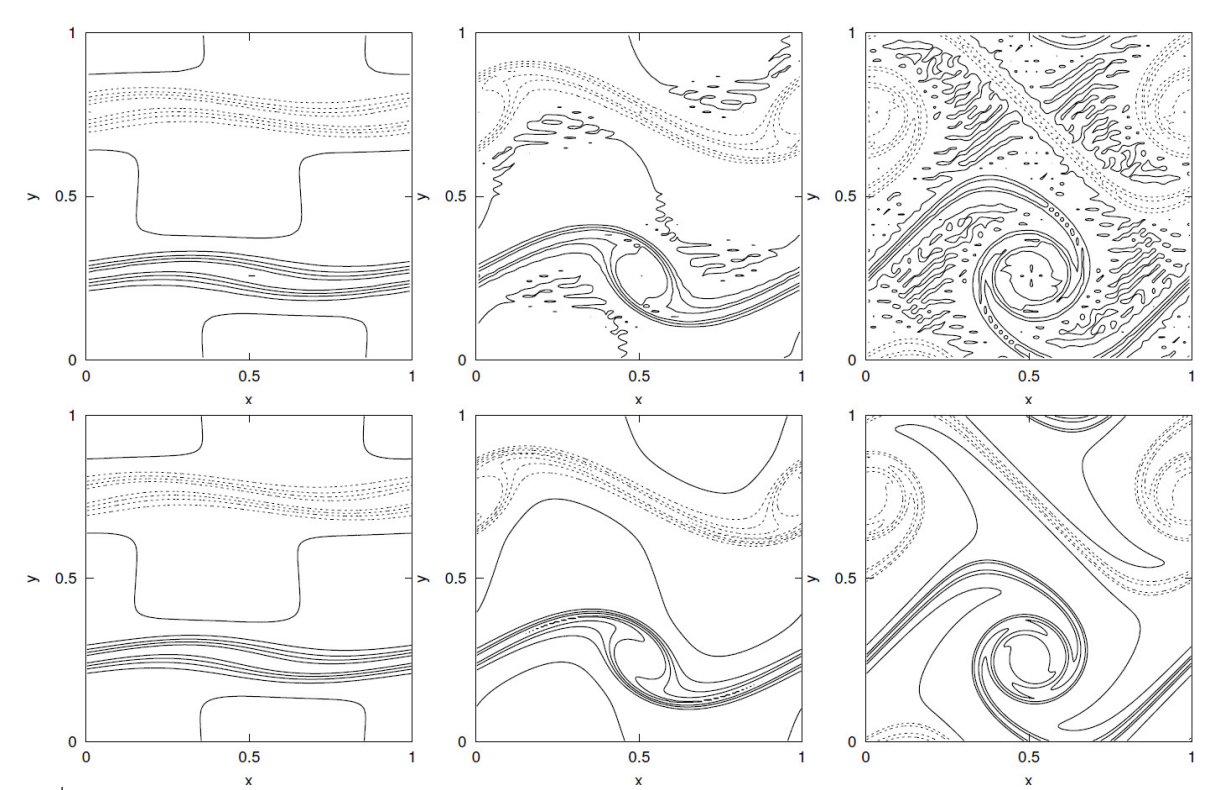
Next, we enable the convection and viscous terms by setting cx = 1:0; cy = 0; cy = 0. The time step is adapted such that CFL number is kept at 0:013 to ensure that the time—integration errors are smaller than the spatial approximation errors. The initial pressure is initialized exactly using the cell-averaged values. The new TGV is now moving along the x-axis and is scaled down with time. The pressure field is thus traveling and decays along with it. The maximum errors are plotted in Fig.8(b) at  $t = 2\pi$  when the flow has completed a round-trip and decayed by 12%. At this point, both convection and diffusion 550 have made substantial contributions to the velocity. The difference between the errors in the pressures of PE4 and PCO4 are the same as shown previously. However, their velocity are almost identical (We remove PCO4 for clarity). The number of grid points per wavelength (PPW) in the graph ranges from 10 on the right to 600 on the left. All treatments deliver a clear sixth-order convergence rates in the velocity. The aver aged rate from 10 to 160 PPW is 6:42. At 200 PPW, the error in the velocity at the first time step is 1:2E-15, which is just five times the machine accuracy.

### Doubly Periodic Double Shear Layer

This simple two-dimensional flow contains Kelvin-Helmholtz instabilities in which the shear layers are perturbed by a sinusoidal disturbance leading to a roll-up of the vortex 580 sheets into a cone-like shape. The periodic domain  $\Omega$ = [0; 1]<sup>2</sup> is taken for this study and the initial velocities are given by

$$u = \begin{cases} \tanh(\sigma(y - 0.25)) & \text{for } y \le 0.5, \\ \tanh(\sigma(0.75 - y)) & \text{for } y > 0.5. \end{cases}$$
$$v = \gamma \sin(2\pi x).$$

The Reynolds number based on the initial maximum velocity and the length of the computational domain is 10; 000. The shear layer parameter ( $\sigma$ ) and the perturbation magnitude ( $\gamma$ ) are set to 30 and 0:05, respectively. The overview of the simulations shown in Fig.9 illustrates how the shear layers get rolled up by the spanwise perturbations at a relatively fast pace. On the 64<sup>2</sup>-grid, the numerical artifacts appear everywhere, most notably on the level close to zero vorticity ( $\Omega$ z = 0). However, the tails of the vortex sheet are still clearly preserved. When the grid resolution is tripled in each direction, some artifacts can still be observed at t = 0:8, but they have completely disappeared at t = 1:2.



รูปที่ 9 An overview of the vorticity (-30:6:30) of the double shear layers flow with N =  $64^2$ (top) and  $192^2$  (bottom) at t = 0:4, 0:8 and 1:2, from left to right respectively. The solid lines represent the positive contours and the dashed line means negative vorticity.

### Turbulent Channel flow

In the first part of this section, we investigate  $Re_{\tau}$  = 180 and establish the relationship between the error in the bulk flow velocity and the normalized grid spacing. The grid resolution requirement found in this section is then used to design two new grids for the two additional Reynolds numbers,  $Re_{\tau}$  = 590 and 950.

Turbulent channel flows have been studied extensively and the shape of the mean profile in the viscous sublayer and the outer layer are well understood. Dean's correlations for the channel flow is very accurate and they agree well with many respectable direct numerical simulations. In Tab.1, we list two mean velocities ratios: the center line and bulk velocities per friction velocity,  $u_c/u_{\bar{\tau}}$  and  $u_b/u_{\bar{\tau}}$ . It is clear that the FSM converges to the spectral solution as the grid resolution increases. The ratio  $u_b/u_{\bar{\tau}}$  on the coarse grid is 1.146 and it is increased to 1.165 on 64<sup>3</sup>-grid which is within the 0:1% of the finalvalue (1:164) on 128<sup>3</sup>-grid. This final value is exactly same as KMM1987 [73]. Thus,FSM should already produce a correct shape of the mean velocity starting from N = 64<sup>3</sup> grid. According to the table, mean flow parameters are monotonically approaching the reference value until 100<sup>3</sup>-grid. However, for the finer grids, the parameters oscillate near the reference value. These small deviations (0:2%) can be attributed to the statistical uncertainty.

Simulation	Domain		Reynolds Number		255	Grio	Velocity ratio			
	$L_x$	$L_z$	$Re_b$	$Re_{\tau}$	$\triangle x^+$	$\triangle z^+$	$\triangle y_{wall}^+$	$\triangle y_{max}^+$	$u_c/u_{\tau}$	$u_b/u_{ au}$
$32^{3}$	$4\pi$	$4\pi/3$	5,127	177.53	69.7	23.2	5.4	18.4	16.87	14.94
$48^{3}$			5,323	177.90	46.6	15.5	3.0	13.6	16.87	14.96
$56^{3}$			5,402	180.05	40.4	13.5	2.5	11.9	17.39	15.00
$64^{3}$			5,472	178.24	35.0	11.7	2.2	10.5	17.86	15.39
$70^{3}$			5,529	178.01	31.9	10.6	1.8	10.3	17.94	15.53
$80^{3}$			5,562	179.24	28.0	9.3	1.6	9.1	18.12	15.52
$100^{3}$			5,624	178.05	22.4	7.5	1.2	7.5	18.36	15.75
$128^{3}$			5,605	178.25	17.5	5.8	0.89	5.2	18.30	15.69
$144^{3}$			5,606	178.50	15.6	5.2	0.40	5.2	18.27	15.73
KMM1987 [73]	$4\pi$	$2\pi$	5,600	180.00	11.8	7.1	0.054	4.4	18.20	15.63
MKM1999 [74]	$4\pi$	$4\pi/3$	5,529	178.13	17.7	5.9	0.054	4.4	18.30	15.52
VK2014 [76]	$4\pi$	$4\pi/3$	5,616	180.00	5.9	2.9	0.024	3.9	18.28	15.60

ตารางที่ 1 Grid parameters and mean flow variables of the standard grids used in this validation compared to the references. The domain sizes are normalized by the channel half-width H. Grid sizes are in wall-unit. The first 8 rows are the simulations using FSM presented in this research.

The key finding in the application of the newly proposed scheme is the relationship between the accuracy of the direct numerical simulation of turbulent flow with the grid resolution which is never reported in the literature before. The error in the mean flow as the function of grid spacing in the streamwise direction is

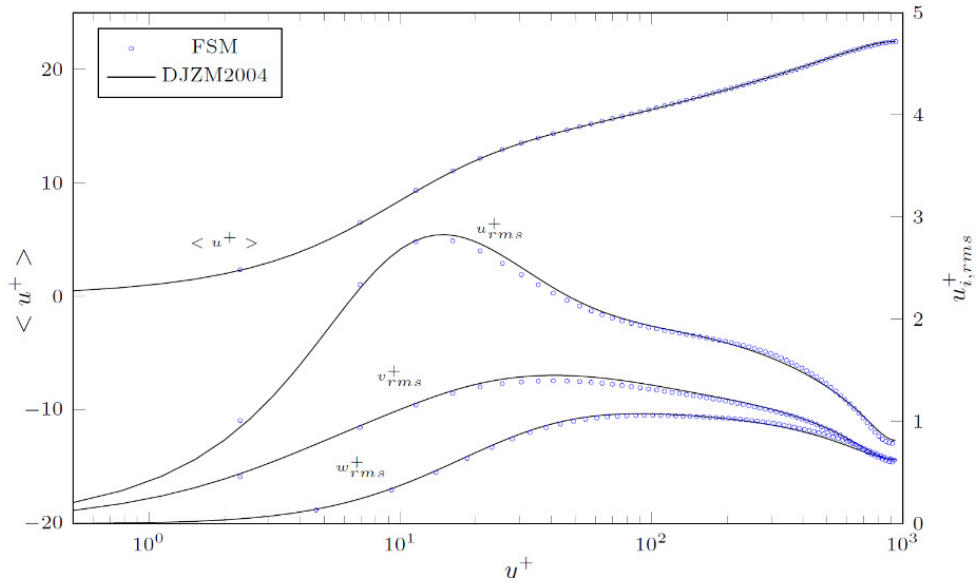
$$log_{10}\left(\frac{er_{ub}}{u_b}\right) = -9.342X_{l10p}^2 + 33.05X_{l10p} - 30.41,$$

Using this relationship, one knows exactly the accuracy of the simulation result w.r.t. the grid size and the simulation can be designed accordingly. Furthermore, this resolution lead to the following grid point requirement for the numerical simulation of turbulent channel flow

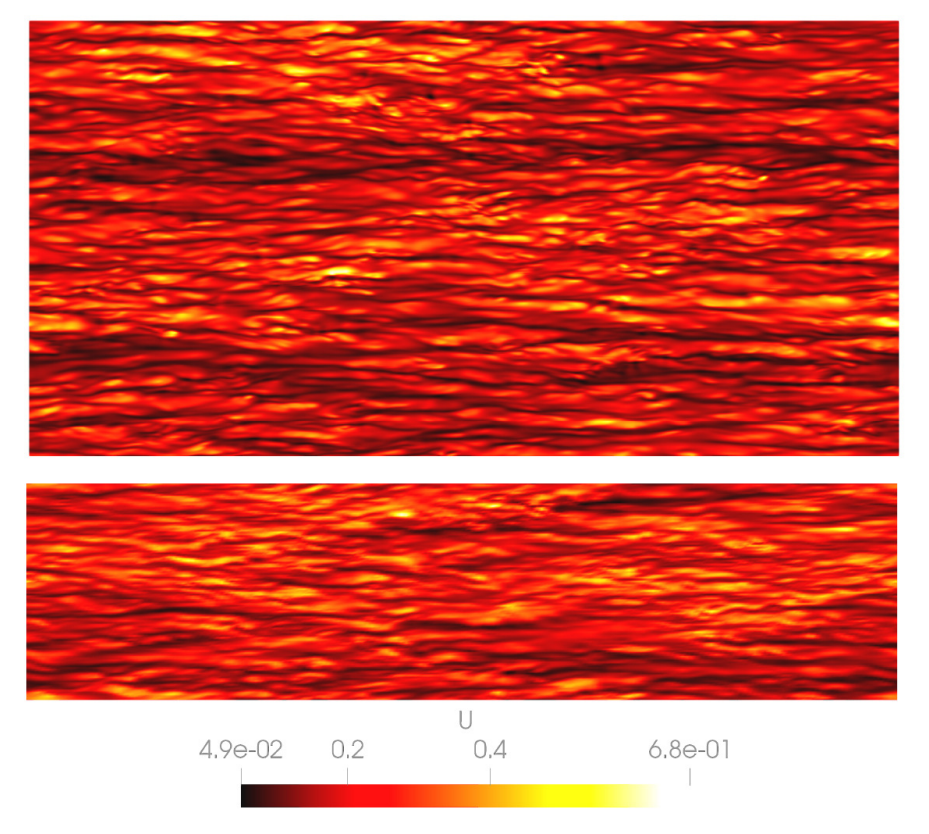
$$N = \left(\frac{Re_{\tau}}{22}\right)^3$$

This can be used a key performance index when comparing different Navier-Stokes solver. The investigator has applied this grid resolution and conducted DNS of two turbulent channel flow at two additional Reynolds number i.e.  $Re_{\tau} = 590$  and 950 and found the error prediction is accurate. The first- and second-order statistics are reported in Fig.10.

The finite surface discretization itself is a natural spatial discretization that sits between FVM and FDM. For coupled conservation problems, FSM is very competitive. The mass conservation equation in FSM is exact and it only approximates the momentum equations. Other coupled problems such as Magnetohydrodynamics and scalar transport should be greatly benefited from the FSM as well. The conserved quantities (mass, chemicals, magnetic fields) can be defined on the controlled volume while the transporting variables (momentums, velocities, ion fluxes) can live on the surface of the controlled volume. The surface-averaged flux can serve as a new type of DOF for existing methods. Effectively, a sixth-order FSM can deliver a comparable solution 28-times faster than the second-order FVM.



รูปที่ 10 Mean streamwise velocity and the RMS of velocities fluctuations on RE950 from the grid designed to meet 1% error in the mean profile:  $[4dx^{+};4dy^{+}_{wall};4dy^{+}_{max};4dz^{+}] = [34.5; 4.7; 27.1; 12.6]$ . The grid density used here is 42:5 less dense than the reference.



รูปที่ 11 A snapshot of u-contour at  $5y^+$  from RE950 (bottom) compared to the result from FVM on a larger domain (top). Similar structures can be seen on both simulations despite FSM having a grid density 11.4-times less. Note that the size of the wall cell with FSM simulation is  $4.7y^+$  and this plane is just above the top of this cell.

## 4. สรุปผลและอภิปรายผล

จากผลการวิจัยตลอดโครงการนั้น ผู้ทำการวิจัยได้พัฒนาเทคนิคด้านการจำลองเชิงตรง (Direct Numerical Simulation) เพื่อการจำลอง การถ่ายเทความร้อนในท่อทรงชรุชระ โดยมีความก้าวหน้าทางวิชาการดังนี้

- 1. ระเบียบวิธีการถ่ายเทความร้อนและมวลด้วยวิธีไฟในต์โวลุ่มลำดับสูง
- 2. พัฒนาวิธี Multigrid สำหรับการแก้สมการ Poisson ที่เกิดจากปัญหาทางการไหลแบบบีบอัดตัวไม่ได้
- 3. สร้างวิธีการไฟในต์เซอร์เฟส สำหรับการจำลองสมการคู่ควบ

โดยโครงสร้างด้านระเบียบวิธีเชิงตัวเลขที่สร้างขึ้น สามารถนำไปใช้แก้ปัญหาการถ่ายเทความร้อนในรูปทรงต่างๆ ได้ทันที และ ระเบียบ วิธีไฟในต์เซอร์เฟส (FSM) นั้น เป็นวิธีการจำลองแบบใหม่ ที่มีศักยภาพในการเข้ามาแทนที่ระเบียบวิธีไฟในต์โวลุ่ม (FVM) ได้ ซึ่งเมื่อ เปรียบเทียบระหว่าง วิธี FSM ความแม่นยำลำดับ 6 ที่พัฒนาขึ้นในโครงการวิจัยนี้ กับ ระเบียบวิธีไฟในต์โวลุ่ม ความแม่นยำลำดับ 4 ที่ ผู้วิจัยพัฒนาขึ้นระหว่างศึกษาปริญญาเอก นั้น ระเบียบวิธี FSM นี้ จะใช้เวลาการคำนวณใกล้เคียงกับวิธี FVM แต่เนื่องจากระเบียบวิธี FSM มีความแม่นยำสูงกว่า ทำให้ต้องการ กริด เพียง ครึ่งเดียวของ วิธี FVM ระเบียบวิธี FSM จึงให้การจำลองที่มีความแม่นยำเท่ากัน เร็วกว่า 2.8 เท่า และใช้ทรัพยากรการคำนวน (แกนการคำนวณ หน่วยความจำ) เพียงครึ่งเดียว ซึ่งทำให้สามารถทำการจำลองที่เลขเรย์ โนลดส์ และ เลขชมิดท์ สูง มีความเป็นไปได้ในทรัพยากรการคำนวณที่จำกัดของไทย

ผลวิจัย ต่อเนื่องจากโครงการนี้พบว่าการจัดการ aliasing error ที่เกิดใน convection term จะช่วยเพิ่มประสิทธิภาพการจำลองจาก 2.8 เท่า ขึ้นไปถึง ประมาณ 80 เท่า เมื่อเทียบกับซอฟท์แวร์การจำลองเดิมที่ใช้ ณ มหาวิทยาลัยเทคโนโลยีแห่งมิวนิก (Technische Universität München) ดังนั้นระเบียบวิธีที่พัฒนาขึ้นในโครงการวิจัยนี้ สามารถ เพิ่มความเร็วในการจำลองได้อย่างมาก ซึ่งจะช่วยให้ วิทยาการด้านการจำลองเพิ่งตัวเลของไทย ก้าวหน้าได้ทัดเทียมกับต่างประเทศ ถึงแม้ว่าทรัพยากรด้านการจำลองจะต่างกันอย่างมาก

การขายยผลของระเบียบวิธีไฟในต์เซอรเฟส ไปยังสมการอนุพันธุ์คู่ควบอื่นๆ จะช่วยเพิ่มผลกระทบของงานวิจัยนี้ และ ช่วยพัฒนา เทคโนโลยีการจำลองเชิงวิทยาศาสตร์ วิศวกรรม และ อุตสาหกรรมของไทย และ ของโลกให้ก้าวหน้าไปอีกระดับ

<sup>1</sup>A.Hokpunna. Dealiasing strategy for higher-order methods in turbulent flow simulations. in Suranaree Journal of Science and Technology (accepted)

### 5. ภาคผนวก ประกอบด้วย

1.Manuscript of "SIP-Multigrid method in Fourth-Order Finite Volume Method for Navier-Stokes Equations". Presented in the International Conference on Computational Methods (ICCM2012), 2012, Gold Coast, Australia.

- 2. Abstract of Presentation "Development of two dimensional Finite Surface Discretization for Fluid Flows" presented in the 7<sup>th</sup> International Conference on Advanced COmputational Methods in Engineering (ACOMEN2017). Ghent University, Ghent, Belgium.
- 3. Reprint of article "Finite surface discretization for incompressible Navier-Stokes equations and coupled conservation laws" Accepted for publication in Journal of Computational Physics (IF=2.99)

### 5.1 Manuscript of

### "SIP-Multigrid method in Fourth-Order Finite Volume Method for Navier-Stokes Equations"

Presented in the International Conference on Computational Methods (ICCM2012), Gold Coast, Australia

The International Conference on Computational Method (ICCM) is a small but focused conference on new method and analysis of numerical solution for physical problems. ICCM2012 is chaired by Prof. YuanTong Gu from School of Chemistry, Physics and Mechanical Engineering, Queensland University of Technology. The Conference handbook is still available online at <a href="https://eprints.usg.edu.au/23150/3/Documentation.pdf">https://eprints.usg.edu.au/23150/3/Documentation.pdf</a>

### 5.2 Abstract of

### "Development of two dimensional Finite Surface Discretization for Fluid Flows"

presented in the 7th International Conference on Advanced COmputational Methods in Engineering 2017,

Ghent University, Ghent, Belgium

The 7th International Conference on Advanced Computational Methods in Engineering is a relatively large Conference consisting of a variety of fields related to computational method in engineering. This is the first venue that the finite surface method is presented. The reception from the audience was interesting. Many participants linked the method with the hybridizible Galerkin Method where it define the edge polynomial to smooth out the diffusion problem. The reaction from the listener was added to the first revision of the FSM paer.

### 5.3 Reprint of

## "Finite surface discretization for incompressible Navier-Stokes equations and coupled conservation laws" (in Press)

This article has been accepted for publication in Journal of Computational Physics (IF=2.99) which is a top journal in the field of Mathematical Physics. The journal is ranked fourth by Web of Science in *Physics, Mathematical* category. In term of number of citations, it is ranked second, behind only the Physical Review E.

The first version of the manuscript was submitted in November 2017. The paper was rejected due to the reviewers did not understood the novelty of the method and thought that the method was similar to Van Leer's scheme. Also, the result was presented in two-dimensional flow and the reviewer suggested that it was not suitable for the journal. In 2019, the new revision was formed to highlight its novelty and included three-dimensional simulations. It was submitted and was given a major correction in March 2020. Due to its highly novel concept, the reviewers still see the method as a finite volume method and ask the author to readdress the difference from the finite volume method. The principal investigator then addressed the misconception and the reviewers recommended further improvement on the presentation of the method and then recommended the publication. The acceptance letter was issued in early August 2020 and the articled is published in the in-press form during the last week of the same month. The editorial process was overseen by Prof. Feng Xiao from Tokyo Institute of Technology in both submissions.

### 5.1 Manuscript of

### "SIP-Multigrid method in Fourth-Order Finite Volume Method for Navier-Stokes Equations"

Presented in the International Conference on Computational Methods (ICCM2012), Gold Coast, Australia

The International Conference on Computational Method (ICCM) is a small but focused conference on new method and analysis of numerical solution for physical problems. ICCM2012 is chaired by Prof. YuanTong Gu from School of Chemistry, Physics and Mechanical Engineering, Queensland University of Technology. The Conference handbook is still available online at <a href="https://eprints.usg.edu.au/23150/3/Documentation.pdf">https://eprints.usg.edu.au/23150/3/Documentation.pdf</a>



### SIP-Multigrid method in Fourth-Order Finite Volume Method for Navier-Stokes Equations

Arpiruk Hokpunna \*1

<sup>1</sup>Mechanical Engineering Department
King Mongkut's University of Technology Thonburi, Bangkok, Thailand
\*Corresponding author: arpiruk.hoku@kmutt.ac.th

### **Abstract**

Navier-Stokes equations (NSE) are a coupled equations of mass-conservation and momentum conservation equations. Time-integration of NSE usually use Fractional Time Stepping Method (FSTM). Under FSTM framework, fourth-order methods for NSE have to solve discrete Poisson equation which can be a 19-point stencil [Kampanis and Ekaterinaris, 2006, Hokpunna and Manhart, 2010a] or a 13-stencil approximations [Hokpunna, 2010b]. Unlike in second-order context, Jacobi and Gauss-Seidel are ineffective as a smoother in 3D. Efficient solution to these discrete Poisson equations are very limited in the literature. In this work, an efficient multigrid method for fourth-order method for NSE is presented. The Strongly Implicit Procedure (SIP) [Stone, 1968] is used as the smoother. Simple injection and second-order interpolation for restriction and prolongation are compared. The performance of the algorithm in direct numerical simulation of turbulent channel flow is presented in comparison with fast-fourier transform method on single processor. The result of this work demonstrates that SIP is an excellent smoother for fourth-order discrete Laplacian and the cost of the fourth-order scheme is not expensive when compare to second-order cheme. A single V-cycle with 3 iteration of SIP in each level is sufficient to keep the residual reduction rate at a constant value.

Keywords: Higher-order method, Poisson equation, multi-grid methods

### Introduction

In recent development of higher-order methods for solving Navier-Stokes Equations (NSE), the enforcement of mass-conservation is found to be a crucial part. The mass conservation and the approximation of pressure force have to be approximated with higher-order accuracy as well. The requirements necessitate the use of higher-order discrete Laplacian with a wider matrix bandwidth than what used in second-order scheme. When the NSE are solved in three dimensions together with projection method, the bandwidth of such of a discrete Laplacian can be 19 [Kampanis and Ekaterinaris, 2006, Hokpunna and Manhart, 2010a]. In comparison with 7-point stencil of the second-order Laplacian, this is very expensive. Suppose that a similar strategies like Gauss-Seidel or Successive Over Relaxation (SSOR) can be used and the number of iteration required to achieve the usual divergence is the same, the cost is almost triple. Relaxation schemes are a crucial part for multigrid method and they are also served very well as preconditioner for Krylov subspace method. In this work, we present application of Strongly Implicit Procedure (SIP) [3] together with a multigrid method for solving higher-order discrete Laplacian arises in the process of continuity. First the Laplacian operators consider in this work is outlined, then the smoothing analysis of several iterative solvers are discussed. Numerical results are presented next in comparison with

same scheme applied to second-order discrete Laplacian. This paper is then closed by the conclusion and the outlook for the research that that would be benefit to computational fluid dynamics communities.

### Higher-order discrete Laplacian in CFD

The Navier-Stokes equations are composed of two equations: (i) mass-conservation equation and (ii) momentum conservation equations. These equations are nonlinearly coupled and are usually solved by operator splitting method or Fractional Time Stepping Method (FSTM). One of the most successful method in the FSTM class is the projection method which first integrate the momentum in time neglecting the mass-conservation completely, then applies a projection operator to the resulting field. This projection guarantees that the outcome is divergence-free, if solved by a direct method. It is commonly agreed now that mass-conservation and pressure calculation must be done in the same order as those used for the momentum equations in order to achieve the same convergence rate. For example, a fourth-order code must compute mass balance and pressure gradient using fourth-order convergence methods. In the frame work of traditional projection method, one must solve a certain form of discrete Poisson equations. For fourth-order scheme on staggered Cartesian grids, there are two discrete Laplacians proposed recently. The first one is called fourth-order discrete Laplacian [Kampanis and Ekaterinaris, 2006, Hokpunna and Manhart, 2010a].

$$(f_{i+3} - 54f_{i+2} + 783f_{i+1} - 1460f_i)/576\Delta x^2.$$
 (1)

In three dimensions this constitutes a 19-point stencil. This operator arises from the multiplication of the fourth-order divergence and fourth-order gradient operators. Another one is called mixed-order discrete Laplacian which is used with approximate projection method [Hokpunna, 2010b]. This Laplacian reads:

$$(-f_{t\pm 2} + 28f_{t\pm 1} - 54f_t)/24(\Delta x)^2, \tag{2}$$

which is a product of the fourth-order divergence and second-order gradient operators. However, this approximate projection method uses a fourth-order approximation of the pressure gradient in the momentum equations which deviates from the usual concept of projection method and thus are called approximate projection method in contrast to the formal projection method which is also called exact projecion method [Almgren and Bell and William, 2000].

It was shown in [Hokpunna, 2010b] that the accuracy of the approximate projection method (solves 13-point Laplacian) is as accurate as the exact projection method (solves 19-point Laplacian) and is sufficient to maintain fourth-order convergence of the NSE solver. Fig.1 demonstrates the accuracy of the mixed-order Laplacian in turbulent channel flow simulation. The mean velocity profile and the profiles of velocity fluctuations collapse almost completely. Since the approximate projection method is less expensive and requires only two ghost cells, we chose this method as the standard method in our code. Therefore in this work we are reporting the result of the mixed-order operator.

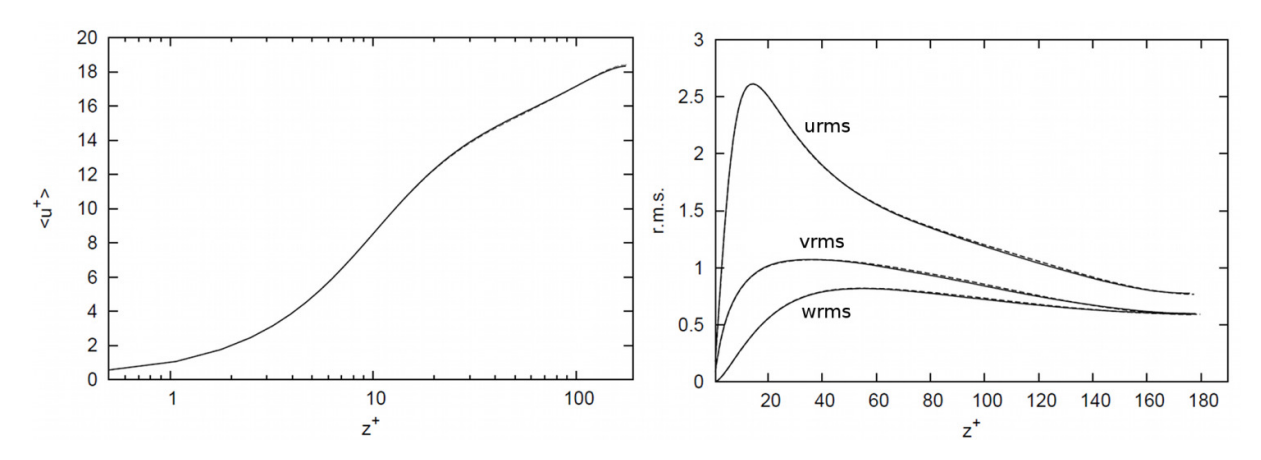


Figure 1 Comparison of mean velocity (left) and rms of velocity fluctuations between exact projection method and the approximate projection method. Solid line: exact projection method, dash-line: approximate projection method.

### **Smoothing Analysis of classic iterative scheme**

Here we consider the amplification factor of the Fourier modes. The Fourier analysis in this context is called local mode analysis. Note that this analysis does not include effects of the boundaries and the grid is assumed to be uniform. The amplification factor obtained from this analysis can be thought of as the best case scenario. For a linear algebriac system Ax = b, let A be split as A = M - N, then a basic iterative method corresponding to this splitting can be written as

$$y^{n+1} = Sy^n + M^{-1}h (3)$$

with  $S = M^{-1}N$ . Let the eigenfunction be  $\psi_l = exp(i(k_1 + k_2))$ , then the amplification of each Fourier mode is given by [Wesseling, 1992]

$$\lambda(\theta_1, \theta_2) = \sum N(k_1, k_2) exp(i(k_1 + k_2)) / \sum M(k_1, k_2) exp(i(k_1 + k_2))$$
(4)

Applying Eq.(4) leads to the amplification factor shown in Fig.1 which indicates a deterioration of the that the smoothing of the high frequencies. The smoothing factor  $(|\lambda|_{\infty}, (|k1|, |k2|) \ge \pi/2)$  was increased from 0.278 to 0.688. Nevertheless, The plot shows that the incomplete LU of the SIP works well as a smoother for the mixed-order discrete Laplacian. The function of the amplification factor when applying SIP to the fourth-order discrete Laplacian (Eq.(1)) looks similar to Fig.1(b) with the smoothing factor of 0.684. In the next section we present the convergence of the full-coarsening V-cycle multigrid method using SIP as the smoother. This method is called MG-SIP.

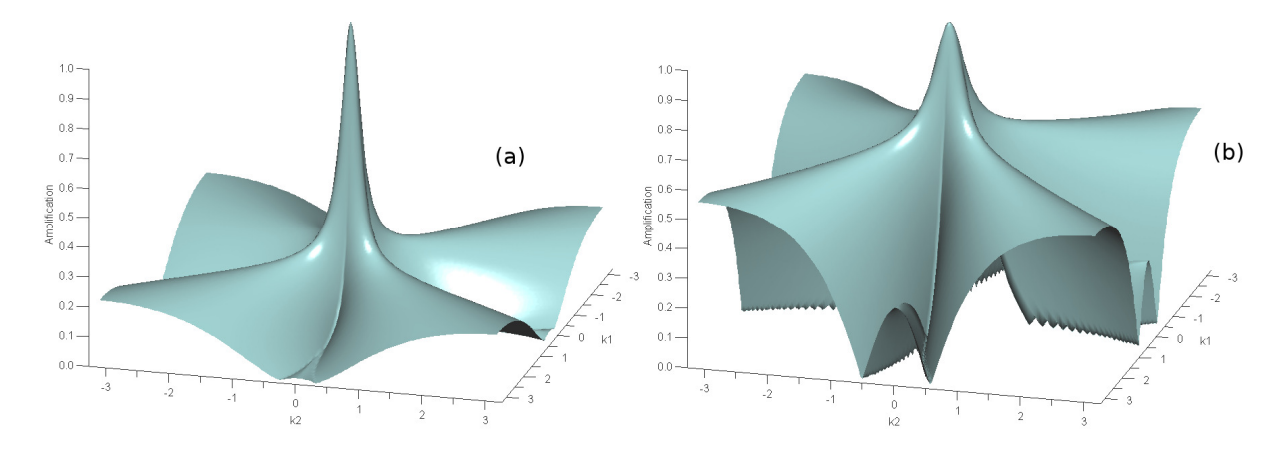


Figure 2 Amplification factors of SIP applied to the second-order (a) and mixed-order (b) Laplacian operators.

### Convergence of the SIP and the of MG-SIP method for higher-order scheme

In order to investigate the convergence of the MG-SIP in a realistic application, we consider a direct numerical simulation of turbulent channel flow. The number of grid cells used here are 64K, 262K and 2.1M where the number of grid cell in each direction is 32, 64 and 128 respectively. In practice, the convergence of the SIP is limited by the treatment of the boundaries. Therefore, the convergence rates of the SIP when applied to the second-order or the fourth-order Laplacian, do not differ much. Figure 3(a) demonstrates the convergence rates of SIP (without multigrid) applied to the Poisson equations generated by the projection methods. The strongly implicit procedure, when applied to the mixed-order Laplacian, converges even faster the rate seen with the second-order.

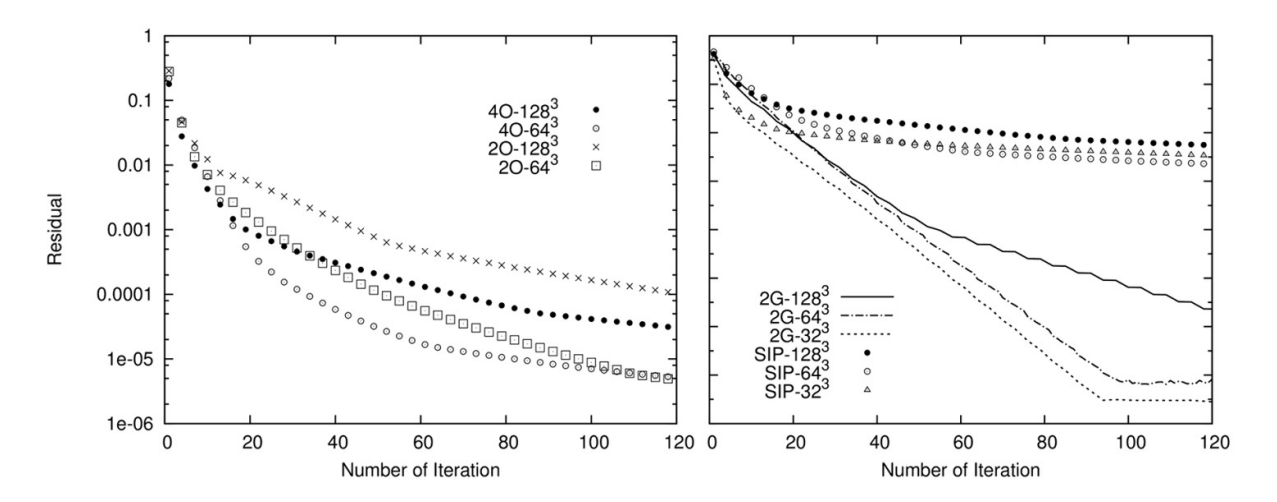


Figure 3 (a) Convergence of the SIP applied to the mixed-order discrete Laplacian (40) in comparison with that of the second-order (20). (b) Convergence of multigrid-SIP (2G) applied to mixed-order Laplacian using two level of coarsening. The numbers after the hyphen indicate the number of grid points. The residual display here and in all other graph is normalized by the initial residual.

Figure 3(b) displays the convergence rate of two-grid method, the multigrid method with only two coarsening levels. The restriction process was done exactly and the prolongation was performed with second-order method. For the two smallest cases, applying multigrid method for two level is sufficient to achieve the residual close to the machine accuracy. The multigrid-SIP method appears to converge at the same rate for all grids. A simple regression indicates that the reduction rate is 0.738. Exceptions are observed for the first fast drop on 32³-grid and the saturation after 40th iteration on 128³-grid. This saturation disappears when an additional level was added (see Fig.4(a)). However, a further coarsening (4-level) do not improve the convergence rate of the 2-level.

Different combinations of the restrictions and prolongations are studied in Fig.4(b) using 3-level grid. In finite volume context, the values stored in the cell is a volume averaged value. Thus the restriction by summing up the values in the eight sub cells is an exact operation. The first-order prolongation means that the 8 sub cells take the value of the coarse grid and the second-order prolongation use linear interpolation between the neighboring cells on the coarse grid. For the first-order restriction, the value of the lowest index on the fine grid is taken as the value of the respective coarse grid. Under this two-grid method, the first-order restriction (injection) decreases the convergence rate while the first-order prolongation has positive effects.

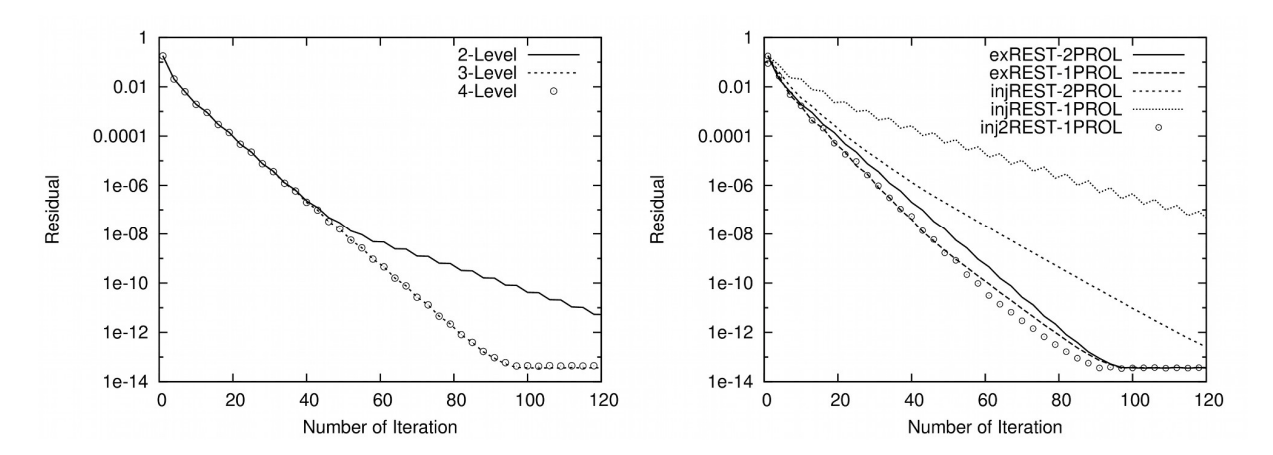


Figure 4 (a) Convergence of the MG-SIP applied to the mixed-order discrete Laplacian (40) on 128-grid with different numbers of coarsening using exREST-2PROL. (b) Convergence on the same grid but with 3-level MG-SIP and different combinations of restrictions (exact restriction (exREST) and prolongations (first-order (1PROL) and second-order (2PROL)). The cross restriction is named inj2.

Figure 4(b) indicates that the exact restriction with the first-order prolongation (exREST-1PROL) works surprisingly well. The overall convergence rate is the same as exREST-2PROL. This means attempt on reproducing the high-frequency content of the coarse grid solution fails to deliver, at least with the second-order approximation. Simple injection converges but at a slower rate. Thus the only thing left to optimize is how to restrict the data. It can be shown that picking one cell from eight cells create phase errors in all three directions. Therefore choosing the sub cells in such a way that the coarse grid get the phase information adequately in all directions should improve the convergence. We tried a cross restriction which sum the four opposite sub cells and it is found to be highly satisfactory. The convergence rate is even slightly faster than exREST-2PROL at low level of residual. Since the exREST-2PROL requires more work, this reflects in the CPU-TIME. The CPU-TIME of this algorithm is measured on Phenom II X6 1050T. The CPU-TIME requires per solution for the MG-SIP to achieve 10E-6 and 10E-10 is 2.43s and 8.42s for EXrest-2PROL. The

same values for inj2REST-2PROL are 2.26s and 6.08s, respectively. Consider that the direct solver (fast fourier transform) requires 1.34 to solve the same problem (with 2E-14 residual) the performance of the MG-SIP is very good.

#### Conclusion

The performance of the MG-SIP applied to the Poisson equation generated by the projection method of fourth-order finite volume discretization of the Navier-Stokes Equations was presented. The test case considered in this work is challenging for any iterative Poisson solver. It contains periodic conditions and highly stretched grid. The result showed that MG-SIP is powerful. It would be very interesting to investigate the convergence rate of other cycles. If one looks closely to the residual plot, the first few iteration has higher reduction, which are approximately 0.18, 0.4 and 0.5. At the moment, MG-SIP cannot achieve these reduction rates and only 0.738 was obtained. On 128-grid used in the test, the time integration of the momentum equation costs 1.3s and the direct solver costs about the same. Therefore the efficient solutions to higher-order discrete Poisson equation are highly demanded. A combination of restriction, prolongation and multigrid cycle that can capture the best residual reduction rate of the SIP is very valuable and the application of MG-SIP as the preconditioner for Krylov subspace method in higher-order context can also be an interesting alternative.

#### Acknoledgement

This research is funded by Thailand Research Fund under contract number MRG 5380279.

#### References

Kampanis, A.N. and A. Ekaterinaris, J. (2006), A staggered grid, high-order accurate method for the incompressible Navier–Stokes equations. *Journal of Computational Physics*, 215(2), pp. 589-613.

Hokpunna, A. and Manhart, M. (2010a) Compact fourth-order finite volume method for numerical solutions of Navier-Stokes equations on staggered grids. *Journal of Computational Physics*, 229(20), pp. 7545-7570.

Hokpunna, A. (2010b), Compact Fourth-order scheme for Numerical Simulations of Navier-Stokes Equations, in Fachgebiet Hydromechanik, Technische Universitaet Muenchen: Munich, Germany.

Stone, H. L. (1968), Iterative Solution of Implicit Approximations of Multidimensional Partial Differential Equations. SIAM Journal on Numerical Analysis, 5(3), pp. 530-538.

Almgren, A. S. and Bell, J. B. and William, Y. C. (2000), Approximate projection methods: Part i. inviscid analysis, SIAM Journal on Scientific Computing 22(4), pp.1139–1159.

Wesseling, P. (1992), An Introduction to Multigrid Methods, John Wiley & Sons

### 5.2 Abstract of

### "Development of two dimensional Finite Surface Discretization for Fluid Flows"

presented in the 7th International Conference on Advanced COmputational Methods in Engineering 2017,

Ghent University, Ghent, Belgium

The 7th International Conference on Advanced Computational Methods in Engineering is a relatively large Conference consisting of a variety of fields related to computational method in engineering. This is the first venue that the finite surface method is presented. The reception from the audience was interesting. Many participants linked the method with the hybridizible Galerkin Method where it define the edge polynomial to smooth out the diffusion problem. The reaction from the listener was added to the first revision of the FSM paer.



Book of abstracts of the 7<sup>th</sup> International Conference on Advanced Computational Methods in Engineering, ACOMEN 2017 18–22 September 2017.

# Development of two dimensional Finite Surface Discretization for Fluid Flows

### Arpiruk Hokpunna<sup>1</sup>

<sup>1</sup> Department of Mechanical Engineering, Faculty of Engineering, Chiang Mai University e-mails: a.Hokpunna@enq.cmu.ac.th

#### **Abstract**

The sixth-order accurate finite-surface discretization for the incompressible Navier-Stokes equations are presented. This discretization retains all the advantage of the staggered without needing to define the staggered cell or co-volume and it is 6X faster than the fourth-order compact finite volume method.

Key words: finite volume method, Navier-Stokes equations, finite surface method, staggered grid, high-order schemes

### 1 Introduction

The work on higher-order methods applied to turbulent flows on collocated grid were discourage at first as the early adopter found that the improvement over the second-order scheme were small [1, 2]. Later, a fourth-order compact scheme is reported to deliver the same predictions as the second-order scheme while using the total grid points 8X lesser [3]. At this comparable level of accuracy, the fourth-order deliver the result 10X faster. The reason why staggered grid is much better than the collocated grid at solving turbulent flow was further investigated in [4]. It was found that half-a-cell distance of the staggered is the reason which means it can resolve the high-frequency components better and thus the high-frequency components of the flow are kept at the momentum instead of diverted to the pressure by the fractional-time-stepping method. In another word, the staggered grid satisfies the mass-conservation better than the collocated one. Thus, what would happen if we could have the exact equation for the mass-conservation?

Consider the arrangement of the flow variables in staggered finite volume discretization (Fig.1(a)) showing the positions of the u and v momentums relative to the pressure cell. If we shrink the control volumes of the momentum cells towards the boundary of the pressure cell, the momentums become the surfaces defined on the faces of the pressure cell as the thicknesses approach zero. It is obvious that the sum of these momentum flux is the mass balance over the pressure cell. The finite surface method (FSM) defines the velocities as surfaced-averaged values living on a set of connected volumes where the mass is set to be conserved similar to finite volume method. The equation for the mass balance becomes an analytical discrete equation. Therefore the only equation left to approximate is the momentum equation. We present the sixth-order approximation of the FSM with three variants of pressure treatments and its validation in the next section.



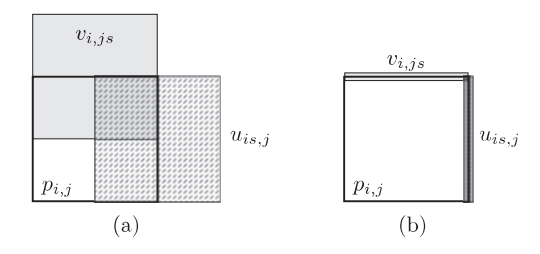


Figure 1: (a) Arrangement of flow variables on staggered grids consisting of pressure cells (clear), u-momentum (dash) and v-momentum (gray) cells. (b) The finite surface discretization constricts the momentum control volumes on to the surfaces of the pressure cell.

N	FSM6:PE4			FSM6:PCO <sub>4</sub>			FVM4:P4E			
	$t_m$	$t_p/n_{it}$	$n_{it}$	$t_m$	$t_p/n_{it}$	$n_{it}$	$t_m$	$t_p/n_{it}$	$n_{it}$	
128 <sup>2</sup> 256 <sup>2</sup>	21.1 78.1	1.07 7.24	88 41	21.6 86.4	1.78 10.26	55 46	31 130.2	0.94 11.96	406 96	
$512^{2}$	396.0	34.80	25	440.0	47.50	32	524.0	43.88	100	

Table 1: Number of iteration needed to reach  $10^{-6}$  relative volumetric imbalance, the CPU-time  $(t_m)$  in millisecond spent in the momentum equation and the time used for projection step per pressure iteration  $(t_p/n_{it})$ .

### 2 Results

In this work, we repeat the same doubly periodic shear layer widely used in the literature. The sixth-order FSM with  $170^2$  cells can match the result of the FVM on  $256^2$  cell. The proposed method, not only more accurate than the fourth-order FVM (which it should), it is also significantly faster than the fourth-order Tab.1. This table suggests that in two dimensions, the newly developed sixth-order FSM is 4.5X faster than the fourth-order FVM per time step which is translated to 6X times faster in a time-dependent problem.

### References

- [1] J. Gullbrand, An evaluation of a conservative fourth order DNS code in turbulent channel, Tech. rep., Center for Turbulence Research, Stanford University (2000).
- [2] O. Shishkina, C. Wagner, A fourth order finite volume scheme for turbulent flow simulations in cylindrical domains, Computers & Fluids 36 (2) (2007) 484–497.
- [3] A. Hokpunna, M. Manhart, Compact fourth-order finite volume method for numerical solutions of Navier–Stokes equations on staggered grids, Journal of Computational Physics 229 (20) (2010) 7545–7570.
- [4] W. Rojanratanangkule, A. Hokpunna, Performance of high-order schemes on collocated and staggered grids, Journal of Research and Applications in Mechanical Engineering 3 (1) (2015) 22–28.

### 5.3 Reprint of

## "Finite surface discretization for incompressible Navier-Stokes equations and coupled conservation laws" (in Press)

This article has been accepted for publication in Journal of Computational Physics (IF=2.99) which is a top journal in the field of Mathematical Physics. The journal is ranked fourth by Web of Science in *Physics, Mathematical* category. In term of number of citations, it is ranked second, behind only the Physical Review E.

The first version of the manuscript was submitted in November 2017. The paper was rejected due to the reviewers did not understood the novelty of the method and thought that the method was similar to Van Leer's scheme. Also, the result was presented in two-dimensional flow and the reviewer suggested that it was not suitable for the journal. In 2019, the new revision was formed to highlight its novelty and included three-dimensional simulations. It was submitted and was given a major correction in March 2020. Due to its highly novel concept, the reviewers still see the method as a finite volume method and ask the author to readdress the difference from the finite volume method. The principal investigator then addressed the misconception and the reviewers recommended further improvement on the presentation of the method and then recommended the publication. The acceptance letter was issued in early August 2020 and the articled is published in the in-press form during the last week of the same month. The editorial process was overseen by Prof. Feng Xiao from Tokyo Institute of Technology in both submissions.

Journal of Computational Physics ••• (••••) ••••••

3

a 10

11

12

13

14

15 16

17

18

19

20

21

22

25

26

27

28

29

30

31

32

33

34

35

36

37

38

39

45

48

**4**0

51

52

53

54

55

56

57

58

60

61

Contents lists available at ScienceDirect

### **Journal of Computational Physics**

www.elsevier.com/locate/jcp



## Finite surface discretization for incompressible Navier-Stokes equations and coupled conservation laws

Arpiruk Hokpunna <sup>a,b,\*</sup>, Takashi Misaka <sup>c</sup>, Shigeru Obayashi <sup>d</sup>, Somchai Wongwises e,f, Michael Manhart g

- a Department of Mechanical Engineering, Faculty of Engineering, Chiang Mai University (CMU), Chiang Mai 50200, Thailand
- <sup>b</sup> Advanced Research Center for Computational Simulation, Chiang Mai University (CMU), Chiang Mai 50200, Thailand
- <sup>c</sup> National Institute of Advanced Industrial Science and Technology (AIST), Tokyo 135-0064, Japan
- d Institute of Fluid Science, Tohoku University, Sendai 980-8577, Japan
- e Department of Mechanical Engineering, Faculty of Engineering, King Mongkut's University of Technology Thonburi (KMUTT), Bangkok 10140, Thailand
- <sup>f</sup> National Science and Technology Development Agency (NSTDA), Pathum Thani 12120, Thailand
- g Fachbebiet Hydromechanik, Technische Universität München (TUM), München 80333, Germany

#### ARTICLE INFO

### Article history. Received 20 December 2019

Received in revised form 12 August 2020 Accepted 16 August 2020

Available online xxxx

#### Keywords:

Finite surface method Navier-Stokes equations Incompressible flow High-order scheme Projection method

### ABSTRACT

We present a new Finite Surface Discretization (FSD) aiming at the incompressible Navier-Stokes Equations (NSE) and other coupled conservation laws. This discretization defines the velocities as surfaced-averaged values living on the faces of the pressure volumes in which the mass is set to be conserved. Consequently, the calculation of the mass balance on these control volumes is exact which allows more accurate information to be kept in the velocity field and produces a very accurate prediction of the pressure in the next time step. The proposed discretization reduces the stencil size of the Poisson equation in the projection method compared to the finite volume and finite difference discretizations. Due to highly accurate mass conservation, the compact sixth-order approximation of FSD can be used with an explicit fourth-order pressure treatment. This property greatly reduces the cost and complexity of the implementation. We present the discrete evolution equation of the surface-averaged velocities together with the enforcement of mass-conservation and the solution procedure for the pressure. The approximation of the NSE under this new discretization uses a combination of finite-difference and finite-volume methods. The proposed method is validated using standard laminar test cases. We identify the conditions under which a fourth-order pressure treatment can support the sixth-order and eighthorder approximations of the convection term using Fourier analysis. The performance of the method is evaluated on turbulent channel flows up to friction Reynolds number of 950. The quantitative relationships between the accuracy of the solution and grid size are identified. We present two performance indices for comparison with other methods. At the error level of 1 per mille, the proposed method is 28-times faster than the classic secondorder scheme.

© 2020 Elsevier Inc. All rights reserved.

https://doi.org/10.1016/j.jcp.2020.109790

0021-9991/© 2020 Elsevier Inc. All rights reserved.

Please cite this article in press as: A. Hokpunna et al., Finite surface discretization for incompressible Navier-Stokes equations and coupled conservation laws, J. Comput. Phys. (2020), https://doi.org/10.1016/j.jcp.2020.109790

3

10

11

12

13

16

17

18

19

20

21

22

23

25

26

27

28

29

30

31

32

33

34

35

36

37

38

39

40

42

43

44

45

46

47

48

49 50

51

52

53

54

55

56

57

58 59

60

61

Corresponding author at: Department of Mechanical Engineering, Faculty of Engineering, Chiang Mai University (CMU), Chiang Mai 50200, Thailand. E-mail address: arpiruk.hok@eng.cmu.ac.th (A. Hokpunna).

**Contents** 

#### A. Hokpunna et al. / Journal of Computational Physics ••• (••••) •••••

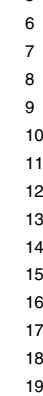
1.	Introd	uction		2
2.	The N	avier-Sto	kes equations and the finite surface discretization	5
	2.1.	Finite-s	urface discretization	5
		2.1.1.	Mass-conservation equation	6
		2.1.2.	Momentum-conservation equation	6
	2.2.	Distinct	ion of FSD from other methods	7
3.	Nume		roximations	7
	3.1.	Convect	ion in <i>x</i> -direction	8
	3.2.	Convect	ive flux in y- and z-directions	9
	3.3.		n in x-direction	9
	3.4.	Diffusiv	e flux in y- and z-direction	9
	3.5.		iform grids and boundary closures	
		3.5.1.	Boundary closures for convection	10
		3.5.2.	Boundary closures for diffusion	
	3.6.	Pressure	e gradient	11
	3.7.		mation of the nonlinear correction	
	3.8.		error management	
4.	Mass		nentum conservations decoupling	
	4.1.		Poisson operator	
5.			cts of the Laplacian and divergence operators	
6.	Valida			
	6.1.	Taylor-0	Green vortex flow	16
		6.1.1.	Stationary inviscid TGV	
		6.1.2.	Traveling-viscous TGV	
	6.2.		periodic double shear layers flow	
	6.3.		ty of plane channel flow	
	6.4.		en cavity flow	
7.			ge of <i>n</i> -th apparent convergence rate with lower-order pressure treatment	
8.	Applic		turbulent channel flow	
	8.1.	Friction	Reynolds number 180	25
		8.1.1.	Mean flow statistics	
		8.1.2.	Second- and third-order statistics	28
		8.1.3.	Wall-normal grid resolution effects	29
		8.1.4.	CPU-time	30
	8.2.	Friction	Reynolds number 590 and 950	31
9.	Conclu	ısion and	l outlook	32
CRediT	autho	rship coi	ntribution statement	33
Declar	ation o	f compet	ing interest	33
Ackno	vledge	ments		33

#### 1. Introduction

Finite volume (FVD) and finite difference (FDD) discretizations have been important instruments for turbulence research. Direct Numerical Simulation (DNS) using these two discretizations helped to achieve a better understanding of turbulence. However, even with the current fastest supercomputers, the complexity of the turbulent flows is still too much for us to tackle it directly, especially in the industry-relevant scales, prompting the need for more efficient approaches. This can be done in many ways such as *i. upgrading the numerical schemes in the discretization* and *ii. develop a new discretization*. The first direction has been researched intensively in the past three decades, numerous higher-order methods have been developed [1–7] among others. The second approach is rarely attempted. A new discretization may enable more flexibility such as the Finite Element Method or provide more robustness such as the Discontinuous Galerkin Method (DGM) [8], but they are not necessarily more efficient.

In the first direction, the computing cost increases as a linear function with the convergence order of the method, but the advantage from the grid density reduction is a quartic function (including the time-step). This advantage is well observed in convection-diffusion problems [5,9,10]. On the other hand, the early applications of higher-order methods to the Navier-Stokes equations (NSE) report notable improvements in the higher-order statistics and the energy spectra in turbulent flow simulations [11–13], but the improvements in the mean fields are almost negligible. One of the reasons is because the higher-order schemes are applied only to the momentum-conservation equation, but the approximations of mass and pressure fluxes are left at second-order. The enforcement of the mass-conservation and the solution of the new pressure, are usually done by the projection method [14,15]. First the momentum equation is integrated in time and the result is treated as the provisional velocity. The divergence of this velocity is then checked. If the field is not divergence-





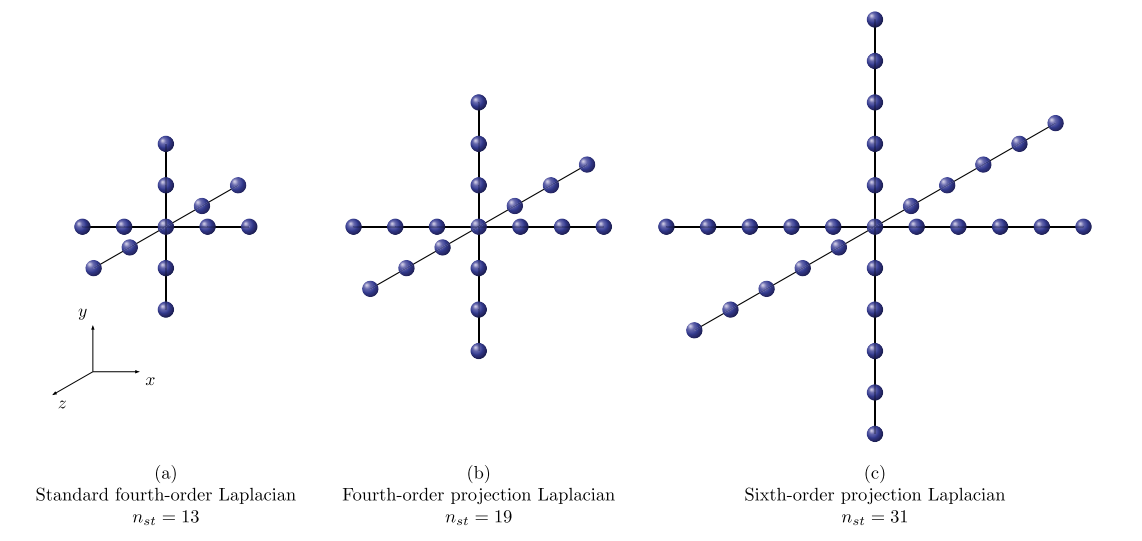


Fig. 1. A standard fourth-order approximation stencil of the Laplacian (a). The standard fourth- and sixth-order projection stencils needed by FDM and FVM on staggered grid (b and c). The proposed method can deliver a sixth-order convergence rate using the left stencil.

free, the projection method then solves the Poisson equation formed by the multiplication of the discrete divergence and the discrete gradients. This requirement complicates the implementation of the higher-order method significantly.

Later, it has been widely accepted that an n-th order NSE solver must use an n-th order method in the approximation of the mass flux and pressure force [2,4,16]. This translates to a special form of the Laplacian in the Poisson equation for the pressure. Fig. 1 compares a fourth-order (19-point) and a sixth-order (31-points) projection Laplacians to an explicit fourth-order Laplacian (13-point). It can be seen that, this requirement greatly increases the cost of higher-order methods. Specifically, the cost ratio between the projection and the explicit Laplacians, at the same order of accuracy is

$$R = \frac{12n - 11}{6n + 1}.\tag{1}$$

Thus, the projection Laplacian is asymptotically twice more expensive than the standard Laplacian. The extra large stencil is a consequence of the projection method. The projection Laplacian could be a full matrix if one of the discrete operators is implicit [17,18].

Later works recognized this limitation and turned to the pressure-Poisson approach. This approach uses a simpler Laplacian that is sufficiently close to the projection Laplacian. Demuren and Wilson [17] adopt the pressure-Poisson formulation and use a compact second-derivative approximation of the Laplacian instead of the full-matrix projection Laplacian. Knikker [4], and Piller and Stalio [19] use second-order Poisson equation. The residuals in the Poisson equation of the pressure-Poisson approach do not exactly reflect the actual mass-imbalance. Therefore, after solving the Poisson equation and correcting the velocities, the divergence must be rechecked. If a certain value of mass-conservation is required, the solver must recompute the divergence and repeat the process again, forming a dual inner-outer iteration loop.

Furthermore, during the development of higher-order NSE solvers, the performance gains of higher-order methods on the collocated grids are small [11,12,20], unlike the staggered grid counterpart. On staggered grids, the compact fourth-order scheme is very accurate [21] and it is ten times faster than the second-order scheme [2], at the same level of accuracy. The reason why higher-order NSE solvers work very well on staggered grids is investigated in [22]. It is concluded that the advantage does not belong to the mathematical discretization of the NSE, but it belongs to the discretization of the physical domain and the arrangement of the flow variables which allow a better calculation of the mass conservation. Thus, if we step back and consider that FVD converts the continuous physical domain into a collection of interconnected volumes (or cells) while FDD discretizes the domain into a set of isolated points in space. Then, it is natural that we can also define the discrete space as a set of <u>surfaces</u>. In this paper, we present a new discretization decomposing the physical domain this way. We call it finite surface discretization (FSD). This approach has superior mass conservation properties compared to the existing methods and greatly reduces the complexity of the pressure treatment mentioned previously.

Let us start from a finite volume discretization on a staggered Cartesian grid in Fig. 2(a). This is the arrangement of the velocities and the pressure cell in two dimensions. The horizontal velocity (u) is defined staggered by half-a-cell in the x-axis while the vertical velocity (v) is staggered in the y-axis. If we constrict these velocity cells towards the boundary of the pressure, the control volumes become control surfaces as the thicknesses approach zero (Fig. 2(b)). In two dimensions, the control surface is a line (or an edge) as shown in the figure. Fig. 3 shows the exploded control surfaces of the three velocities while the pressure is kept as a volume in the transparent cube. The discrete physical domain where the velocities live is now just the outer shell of the pressure. The integral of the velocity divergence on this cell can be computed exactly

A. Hokpunna et al. / Journal of Computational Physics ••• (••••) •••••

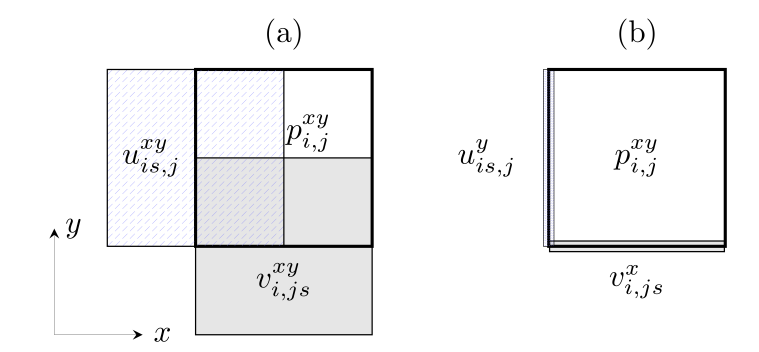


**Fig. 2.** (a) Arrangement of flow variables on 2D staggered grids of FVM. The variables are the pressure (clear), u-momentum (dash) and v-momentum (gray) cells. (b) Finite surface discretization constricts the momentum control volumes on to the surfaces of the pressure cell.

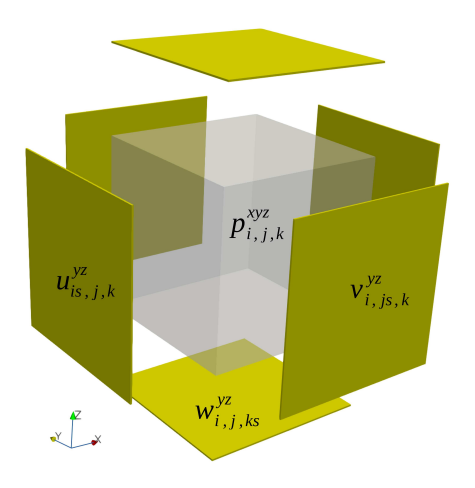


Fig. 3. Exploded view of the controlled-surfaces where FSD defines the velocities. Each surface contains only one normal velocity.

by summing the respective fluxes on these faces. Setting up a spatial discretization this way renders the discrete mass-conservation equation exact. The only equation left to approximate is the momentum-conservation.

A similar idea first appeared in electromagnetic simulations by the work of Vinokur and Yarrow [23,24] who coined the term finite-surface method. There are some follow-up works in the same field [25,26]. The main argument of the method is that the divergence of the electric and magnetic fluxes, computed by a simple flux summation, is the exact integral of the divergence. Unfortunately, the method has been presented in a second-order context where there is no distinction among pointwise, line-averaged, and volume-averaged quantities. Their final formulation looks the same as other second-order FD and FV methods. This even led them to mistake an FDM of [27] as an FSM in [23] which was corrected in the later work [24]. If the method had been presented in a higher-order context, it would be clear that the definitions and the approximation coefficients are different. Due to this, the method is almost unknown to the CFD community and we only found it during the early preparation of this paper.

Perhaps one of the reasons preventing the finite surface method to be widely used is that the method makes no sense without the coupled conservation laws. It is relatively more difficult to evolve the surface-averaged quantity than the pointwise or volumetric quantities because an FSM would contain FVM- and FDM-directions. Thereby, the method and the dimensions of the fluxes are not isotropic. Without the coupled conserved quantities, the finite surface discretization is not worth the additional efforts. However, if there are coupled conservation laws, the finite-surface discretization becomes very competitive, especially in the high-order context. We call the approximation of the FSD presented in this work as the Finite Surface Method (FSM), following the referral of finite difference and finite volume methods.

The proposed discretization enjoys the following advantages:

- It delivers the exact discrete mass conservation.
- The computation of the exact mass balance costs the same as in other second-order schemes.
- It enjoys the half-a-cell advantage in the pressure gradient calculation similar to staggered grid arrangement.
- It eliminates the extended stencil needed by the projection method.
- It can use a lower order approximation for the pressure and still support higher-order momentum approximations.

Please cite this article in press as: A. Hokpunna et al., Finite surface discretization for incompressible Navier-Stokes equations and coupled conservation laws, J. Comput. Phys. (2020), https://doi.org/10.1016/j.jcp.2020.109790

a

This new discretization bears some similarities with the scheme IV of Van Leer [28] in which he proposed to improve the accuracy of numerical simulations by adding the cell boundary values as the flow variables, in addition to the original cell average. This method is very popular in compressible flow solvers. The modern adaptation of this concept is called the active flux schemes (AF) [29,30]. This class of method defines the velocity as a pointwise value located at the boundary. The fluxes leaving the surface must be integrated from these flux points [30]. In the same spirit, Xiao developed the multi-moment method (MM) in [31,32] where both cell-averaged and face-averaged are used. The method later includes derivatives in [33]. The multi-moment method chooses to integrate the cell-averaged data in time, and then transfer the changes back to the surface average using interpolation in the second step. The hybridizable discontinuous Galerkin method (HDGM) [34–36] also defines extra boundary polynomials in addition to the cell polynomial and uses them to solve the instabilities in diffusion problems. At best, the mass imbalance of the cell is only exact up to the polynomial being used. In our approach, we define the normal velocities as a surface average on the faces of the pressure's control volume—one degree of freedom per face. The convection and the diffusion are directly exchanged through the surface and the edges of the control surface. We have not seen such a formulation of the momentum balance in the literature. To the best of our knowledge, this paper is the first work that evolves the discrete surface-averaged quantities directly.

The most distinct concept of the proposed discretization is that the velocity and the pressure are operating on a different dimension. The pressure is defined as a d-dimensional control volume while the velocity is defined as a (d-1)-dimensional hyperplane. This is completely different from FVD and FDD where the pressure and the velocity are defined on the same type of geometry. From the method of weighted residual's point of view, the other three methods (AF, MM, and HDGM) minimize the residual over the control volumes using different definitions of the local bases, the weighting functions, and the inherent variables. FSD, on the other hand, minimizes the residual over the surfaces of such volumes. Therefore, the method presenting here is a completely new class of its own.

This paper is organized as follows. First, the finite surface discretization of the NSE and a detailed comparison to other related methods are presented. The sixth-order approximations of the momentum equation are then introduced. After that, we address the advantages and quantify them for the projection method. It will be shown that an n-th order momentum approximation can be supported by an (n-2)-th or even (n-4)-th order treatment of the pressure. This means the sixth-order FSM can use the 13-point stencil in Fig. 1(a), instead of the 31-point of Fig. 1(c). After that, the proposed scheme is validated using the Taylor-Green vortex flow, a double shear layer flow, an instability in a plane channel flow, and a lid-driven cavity flow. We then identify the range in which the sixth- and eight-order FSM can be supported by the fourth-order approximations of the pressure using a model spectrum analysis. The performance of the method in turbulent flows is demonstrated using a turbulent channel flow up to the friction Reynolds number  $Re_{\tau} = 950$ . The CPU-time of the proposed method is presented and compared with a compact fourth-order FVM. The grid resolutions requirement is determined for arbitrary accuracy in the mean flow  $(10^{-4} < |error/u_b| < 10^{-1})$ . Finally, we present the concluding remarks and outlook in the last section.

#### 2. The Navier-Stokes equations and the finite surface discretization

The integral form of the Navier-Stokes equations for incompressible Newtonian fluid can be written as

$$\oint_{A} \mathbf{u} \cdot \mathbf{n} \, dA = 0 \tag{2}$$

$$\frac{\partial}{\partial t} \int_{\Omega} \mathbf{u} \, d\Omega + \oint_{A} (\mathbf{u} \cdot \mathbf{n}) \mathbf{u} \, dA = \nu \oint_{A} \mathbf{T} \, dA - \frac{1}{\rho} \oint_{A} p \mathbf{I} \cdot \mathbf{n} \, dA \tag{3}$$

Here, the variables and notations are velocity vector:  $\mathbf{u}$ , pressure: p, strain rate tensor:  $\mathbf{T}$ , identity matrix:  $\mathbf{I}$ , density:  $\rho$  and the kinematic viscosity:  $\nu$ . The unit vector ( $\mathbf{n}$ ) of an infinitesimal area dA is pointing outwards of the volume  $d\Omega$ .

#### 2.1. Finite-surface discretization

On Cartesian grids, a system of staggered grids (Fig. 2a) can be set up by putting *collocated grid points* along a real line x using a strictly increasing function  $\xi(i)$ ,  $x_i = \xi(i)$ , i = 0, ..., nx. We can then define *staggered grid points* using the same function if it is continuous, otherwise it can be defined by  $xs_i = \frac{1}{2}(x_{i-1} + x_i)$ , i = 1, ..., nx, with the following transfer property:  $xs_i = x_{i-1/2}$ . We define the boundary of the pressure cells on these the staggered grid points i.e.  $\Omega_i = [xs_{i-1}, xs_i]$ . In 3D,  $\Omega_{i,j,k}$  is defined by the Cartesian product  $\Omega_{i,j,k} = (x,y,z) \in [x_{i-1/2}, x_{i+1/2}] \times [y_{j-1/2}, y_{j+1/2}] \times [z_{k-1/2}, z_{k+1/2}]$ .

The pressure volume is defined as the cell-averaged value on the control volume  $\Omega_{i,j,k}$ 

$$[p]_{i,j,k}^{xyz} = \frac{1}{\Omega_{i,j,k}} \int_{x_{i-1/2}}^{x_{i+1/2}} \int_{y_{i-1/2}}^{y_{j+1/2}} \int_{z_{k-1/2}}^{z_{k+1/2}} p(x,y,z) dx \, dy \, dz. \tag{4}$$

.

A. Hokpunna et al. / Journal of Computational Physics ••• (••••) •••••

**Fig. 4.** The u-velocity on the west-face of the 3D pressure cell and the edge velocity fluxes responsible for the convection in y- and z-directions in Eq. (18). (For interpretation of the colors in the figure(s), the reader is referred to the web version of this article.)

The velocity is defined as a surface-averaged value. For example, the u-velocity on the west-face of the pressure cell (at  $x_{is} = x_{i-1/2}$ ) is given by

$$[u]_{is,j,k}^{yz} = \frac{1}{A_{j,k}} \int_{v_{j-1/2}}^{y_{j+1/2}} \int_{z_{k-1/2}}^{z_{k+1/2}} u(x_{is}, y, z) \, dy \, dz, \tag{5}$$

where  $A_{j,k} = [y_{j-1/2}, y_{j+1/2}] \times [z_{k-1/2}, z_{k+1/2}]$ . The other velocity components on the negative faces of the pressure cell are  $[v]_{i,js,k}^{xz}$  and  $[w]_{i,j,ks}^{xy}$ . The velocity variables are treated as continuous functions, and thus u on the east-face of  $[p]_{i,j,k}$  is equal to u on the west-face of  $[p]_{i+1,j,k}$ . Therefore, FSD only defines one u-momentum per pressure cell.

#### 2.1.1. Mass-conservation equation

The integral mass-conservation in Eq. (2) applied to the control volume  $\Omega_{i,i,k}$  of the pressure cell is

$$\oint_{A} [\mathbf{u}] \cdot \mathbf{n} \, dA = [\operatorname{div}]_{i,j,k}^{xyz} \triangle x_{i} \triangle y_{j} \triangle z_{k} = \left( [u]_{i+\frac{1}{2},j,k}^{yz} - [u]_{i-\frac{1}{2},j,k}^{yz} \right) \triangle y_{j} \triangle z_{k} + \left( [v]_{i,j+\frac{1}{2},k}^{xz} - [v]_{i,j-\frac{1}{2},k}^{xz} \right) \triangle x_{i} \triangle z_{k} + \left( [w]_{i,j,k+\frac{1}{2}}^{xy} - [w]_{i,j,k-\frac{1}{2}}^{xy} \right) \triangle x_{i} \triangle y_{j}, \tag{6}$$

where  $div = \partial u_i/\partial x_i$ .

This discretization of the mass-conservation equation is exactly the same as in the finite-volume method. However, in the FVM the fluxes must be deconvolved from the cell-averaged values while in the proposed FSM they are directly discretized and thus Eq. (6) is analytically exact. Using the fractional time-stepping method (FSTM) [14,15], we can apply this mass-conservation equation after the momentum was evolved. The mass imbalance will be eliminated by a projection method described later.

#### 2.1.2. Momentum-conservation equation

In three dimensions, we conserve  $\rho \mathbf{u} = (\rho[u]_{is,j,k}^{yz}, \rho[v]_{i,js,k}^{xz}, \rho[w]_{i,j,ks}^{xy})$ , the area-averaged momentum in x, y and z respectively. Let us consider the discrete form of the first component:

$$A_{j,k} \frac{\partial [u]_{\text{is},j,k}^{yz}}{\partial t} = -\mathcal{C}_{\text{is},j,k} + \nu \mathcal{D}_{\text{is},j,k} - \frac{1}{\rho} \mathcal{P}_{\text{is},j,k}$$

$$(7)$$

The velocity  $[u]_{is,j,k}^{yz}$  is located on the west-face of the pressure cell shown in Fig. 3. Fig. 4 illustrates this surface and the associated line-averaged velocities required for the convection term. The terms  $C_{is,j,k}$  and  $D_{is,j,k}$  are shorthand notations of the net convective and diffusive fluxes. The pressure force is represented by  $P_{is,j,k}$ . On Cartesian grids they are defined as follows:

$$C_{is,j,k} = \left[\frac{\partial uu}{\partial x}\right]_{is,j,k}^{yz} \triangle y_j \triangle z_k + \left(\left[vu\right]_{is,j+\frac{1}{2},k}^z - \left[vu\right]_{is,j-\frac{1}{2},k}^z\right) \triangle z_k + \left(\left[wu\right]_{is,j,k+\frac{1}{2}}^y - \left[wu\right]_{is,j,k-\frac{1}{2}}^y\right) \triangle y_j, \tag{8}$$

$$\mathcal{D}_{is,j,k} = \left[\frac{\partial^2 u}{\partial x^2}\right]_{is,j,k}^{yz} \triangle y_j \triangle z_k + \left(\left[\frac{\partial u}{\partial y}\right]_{is,j+\frac{1}{2},k}^z - \left[\frac{\partial u}{\partial y}\right]_{is,j-\frac{1}{2},k}^z\right) \triangle z_k + \left(\left[\frac{\partial u}{\partial z}\right]_{is,j,k+\frac{1}{2}}^y - \left[\frac{\partial u}{\partial z}\right]_{is,j,k-\frac{1}{2}}^y\right) \triangle y_j, \quad (9)$$

Please cite this article in press as: A. Hokpunna et al., Finite surface discretization for incompressible Navier-Stokes equations and coupled conservation laws, J. Comput. Phys. (2020), https://doi.org/10.1016/j.jcp.2020.109790

[m3G; v1.292; Prn:27/08/2020; 7:19] P.7 (1-36)

A. Hokpunna et al. / Journal of Computational Physics ••• (••••) •••••

 $\mathcal{P}_{is,j,k} = \left[\frac{\partial p}{\partial x}\right]_{is,j,k}^{yz} \triangle y_j \triangle z_k. \tag{10}$ 

The above discrete forms can be obtained by integrating the momentum equation in Eq. (3) over the control surface of  $[u]_{is,j,k}^{YZ}$ . In the *x*-direction, the convective term  $\partial uu/\partial x$  is formulated like in an FDM and integrated over the control surface (hatched blue in the figure). In *y*- and *z*-directions, the momentum is exchanged with the next cells through the edges of the face in an FVM formulation (blue and red lines in the figure). Note that the first term in the RHS of Eqs. (8) and (9), are the limit of the flux difference divided by  $\triangle xs_i$ . Numerical approximations for all the terms in the above equations can be picked directly from the schemes developed for FVM and FDM. Our choices of these approximations are described in section 3.

#### 2.2. Distinction of FSD from other methods

From a certain viewpoint, our approach shares some similarities with Van Leer's scheme IV [28], the active fluxes method [29], and the multi-moment method [31,32]. A distinction and the contributions of this work should be properly addressed. FSM can turn one of the coupled equations to an exact discrete form and eliminate the extended stencil in the Projection method. To the best of our knowledge, this is the first discretization achieving these two properties on an analytical level, unlike the pressure-Poisson formulation [15] or the approximate projection [37] in which the continuity is not satisfied exactly after the velocity correction. This property cannot be found in the Van Leer's scheme IV, active fluxes, and the multi-moment methods. These approaches are aiming at compressible flow problems that do not need the Poisson equation for the pressure. Thus, applying them directly to the incompressible flow will create a complicated Poisson equation. On the other hand, applying the FSD to compressible flows may be less beneficial as well. Nevertheless, a compressible flow solver can benefit from the exact mass computation by storing  $\rho \mathbf{u}_n$  at the surface and enjoy the exact cell-averaged pressure. Furthermore, the multi-moment method stores two types of velocities: the cell-averaged and the surface averaged values. The surface-averaged velocity is defined on every face of the cell (u, v, and w). On a 3D Cartesian grid, this method stores 12 DOFs per pressure cell. In contrast, our method stores only the normal velocity on each face. This means 3 velocities per pressure cell which is the same number as in the standard FVM and FDM. The proposed method does not store any other types of velocity, neither cell-averaged nor pointwise data. Therefore, the same convergence rate can be achieved using a much lower DOF, but at the expense of less data locality.

FSM can be criticized for not being as compact as DGM and the multi-moment method. However, having less unknown per cell is not actually a disadvantage. The method we present here can achieve a sixth-order convergence using 4 DOFs. Even though the standard DG and the HDG methods are shown to possess a global superconvergence for the pure convection problem [38] and the diffusion dominated problem [35]. The application of DGM and HDGM to NSE only obtains k+1 convergence rate [36,39–41], when used with a k-th order polynomial. Thus, DGM would need a fifth-order polynomial (35 DOF per cell in 3D) to achieve the same rate of convergence. This factor allows FSM to use a grid 3.3-times denser per direction if the complexities of the methods are comparable. Furthermore, the Courant-Friedrichs-Lewy (CFL) limit in DGM scales with  $O(\triangle x/k^2)$  [42] while that of FVM and FDM grows with  $O(\triangle x/k)$ . Thus DGM should cost much more than standard methods (FDM/FVM). A similar cost analysis is not yet applied to FSM. But since the approach we are proposing is based on FVM and FDM, we conjecture the cost to grow similarly.

We would like to emphasize that, the proposed discretization does not improve the accuracy in the approximation of the convection and diffusion terms directly. The staggered FVM, FDM, and FSM should be similarly accurate when they are used with the same class of approximation. For example, the compact FDM from Lele [1] and the compact FVM from Kobayashi [43] should give similar results. The key improvement of FSM is *the coupling with the mass-conservation equation*. Under the projection method, the divergence operator detects the non-solenoidal part of the provisional velocity field and the Poisson equation searches for a pressure that could eliminate this part. An approximate divergence operator will inevitably sense some of the divergence wrong (mistakes non-divergence part as a divergence one). This solenoidal part in the provisional velocity, will be washed out during the projection (see Chap. 5 in [44]). The finite-surface discretization minimizes this loss of information, and thereby improves the overall accuracy.

The basic concept of this discretization can be applied to any governing equations. However, the systems governed by conservation laws (contain divergence operator) would benefit most. For example, the velocity-vorticity formulation in [45, 46] would benefit from FSM more than the vorticity-velocity formulation in [47] and the vorticity-stream function [48,49].

Lastly, we would like stress that FSD is a spatial discretization that can be solved by any type of mathematical approximations e.g. spectral methods or method of least square. In the current work, we use a traditional approach similar to finite volume and finite difference methods. The numerical approximation is a reconstruction type. The detail of the discrete equations and the approximations are explained in the following sections.

#### 3. Numerical approximations

In this work, we use compact sixth-order schemes from Lele [1] and Kobayashi [43] as well as a nonlinear correction concept from [2] and [50]. The numerical approximations are presented here only for u. The applications to the rest are straightforward.

A. Hokpunna et al. / Journal of Computational Physics ••• (••••) •••••

#### 3.1. Convection in x-direction

The convective term in x-direction:  $[\partial uu/\partial x]_{is,j,k}^{yz}$  shown in Eq. (8) can be approximated in different ways such as; the divergence form:

$$\left[\frac{\partial uu}{\partial x}\right]_{is,i,k}^{yz} = \left[\frac{\partial uu}{\partial x}\right]_{is,i,k}^{yz} \tag{11}$$

the convective form:

$$\left[\frac{\partial uu}{\partial x}\right]_{is,j,k}^{yz} = 2\left[u\frac{\partial u}{\partial x}\right]_{is,j,k}^{yz} \tag{12}$$

the skew-symmetric form

$$\left[\frac{\partial uu}{\partial x}\right]_{is,j,k}^{yz} = \frac{1}{2} \left( \left[\frac{\partial uu}{\partial x}\right]_{is,j,k}^{yz} + 2 \left[u\frac{\partial u}{\partial x}\right]_{is,j,k}^{yz} \right)$$
(13)

The convective form is known to be unstable when applied in FDM to turbulent flows due to the strong aliasing errors [51]. The divergence form approximates a gradient having twice wave number and thus it usually underpredicts the convection. The skew-symmetric form balances the two errors and it can be made energy and mass-conserving [51–53]. In this work, we are not attempting to construct a fully-conservative scheme. Therefore, we select the standard convective form because it is the most accurate when it is stable. On a smooth field, this form can be used with the FSM directly, but when the field is rough, a slight filtering of the convective term is sufficient to stabilize the flow. This filtering is one of the common approaches used to control aliasing errors in higher-order schemes.

The convective form in FSM reads

$$\left[\frac{\partial uu}{\partial x}\right]_{is,j,k}^{yz} = \left[u\frac{\partial u}{\partial x} + u\frac{\partial u}{\partial x}\right]_{is,j,k}^{yz} = 2\left[u\frac{\partial u}{\partial x}\right]_{is,j,k}^{yz}$$
(14)

$$=2\left[u\right]_{is,j,k}^{yz}\left[\frac{\partial u}{\partial x}\right]_{is,i,k}^{yz}+NC1. \tag{15}$$

This convective flux is the convolution of the *transporting derivative*  $(\partial u/\partial x)$  and the *transported velocity* (u) over the controlled surface  $A_{is,j,k}$ . A direct multiplication of them is a *linearized convective flux* (LC) which is only a second-order approximation. The nonlinear correction NC1 compensates this deficiency and it will be discussed later.

The surface-averaged velocity  $[u]_{is,j,k}^{yz}$  in Eq. (15) is an inherent variable and can be used directly. The second term,  $[\partial u/\partial x]_{is,j,k}^{yz}$ , can be computed using one of the formulas from [1]. It can be rewritten in the following form:

$$\alpha_{1,1} \left[ \frac{\partial u}{\partial x} \right]_{is-1,j,k}^{yz} + \left[ \frac{\partial u}{\partial x} \right]_{is,j,k}^{yz} + \alpha_{1,2} \left[ \frac{\partial u}{\partial x} \right]_{is+1,j,k}^{yz} = \beta_{1,1} \left( [u]_{is-1,j,k}^{yz} - u_{is-2,j,k}^{yz} \right) + \beta_{1,2} \left( [u]_{is,j,k}^{yz} - u_{is-1,j,k}^{yz} \right) + \beta_{1,4} \left( [u]_{is+2,j,k}^{yz} - u_{is+1,j,k}^{yz} \right)$$

$$(16)$$

On a uniform grid, the sixth-order compact scheme uses  $\alpha_{1,1} = \alpha_{1,2} = 1/3$ ,  $\beta_{1,2} = \beta_{1,3} = 29/(36\Delta x)$  and  $\beta_{1,1} = \beta_{1,4} = 1/(36\Delta x)$ .

The coefficients for a higher order scheme can be rearranged from [1]. Alternatively, they can be obtained directly from [43] using the second fundamental theorem of calculus. (See section 2.4.3 in [2].) The latter approach makes the equation compatible with Eq. (19) and delivers conservative convective mass fluxes over the momentum control surface.

Our convective form above looks similar to FDM where the velocity variable (u) transports the changes of  $\partial u/\partial x$  along the x-direction and the variable u can be called *transporting velocity* or convective velocity. However, there are two differences that should be addressed. First, the convective form of FDM does not have the factor two which is achieved by the cancellation of the second  $u\partial u/\partial x$  by the convection in y- and z-direction (due to the continuity constraint), that is  $\partial (u_i u_j)/\partial x_j = u_j \partial u_i/x_j + u_i \partial u_j/x_j$ . In FSM, the other two directions are FVM-like and could not cancel the term. Second, we learned from the development of higher-order FVM that the convective velocity around the momentum cells should be divergence free in order to satisfy the Galilean invariance and the local mass conservation. This means, we have to transfer the mass fluxes surrounding the pressure cell to the momentum and use them as the convective fluxes. Integrating the divergence over the surface of  $[u]_{is,i,k}^{yz}$  gives

$$[div]_{is,j,k}^{xyz} = \left[\frac{\partial u}{\partial x}\right]_{is,j,k}^{yz} + \frac{1}{\Delta y_j} \left( [v]_{is,j+\frac{1}{2},k}^z - [v]_{is,j-\frac{1}{2},k}^z \right) + \frac{1}{\Delta z_k} \left( [w]_{is,j,k+\frac{1}{2}}^y - [w]_{is,j,k-\frac{1}{2}}^y \right)$$
(17)

Once the line-averaged velocities were determined, the velocity derivative here can be injected directly into Eq. (15). This derivative flux is thus the one doing the convection. Hence, we denote it as *the transporting derivative* earlier.

Please cite this article in press as: A. Hokpunna et al., Finite surface discretization for incompressible Navier-Stokes equations and coupled conservation laws, J. Comput. Phys. (2020), https://doi.org/10.1016/j.jcp.2020.109790

#### 3.2. Convective flux in y- and z-directions

Along the edges of the u-momentum in Fig. 4, the convection is a result of the line integral flux transfers. The net convective flux in y-axis is the difference between the convective flux at the top and the bottom edges. At the top edge of  $[u]_{is.i.k}^{yz}$ , the convective flux is given by

$$[vu]_{is, i+\frac{1}{2}, k}^{z} = [\overline{v}]_{is, i+\frac{1}{2}, k}^{z} [u]_{is, i+\frac{1}{2}, k}^{z} + NC2.$$
(18)

The surface-averaged u is deconvolved into a line-averaged on the edge of the control surface using this equation:

$$\alpha_{2,1}[u]_{is,is-1,k}^{z} + [u]_{is,is,k}^{z} + \alpha_{2,2}[u]_{is,i+1,k}^{z} = \beta_{2,1}[u]_{is,i-2,k}^{yz} + \beta_{2,2}[u]_{is,i-1,k}^{yz} + \beta_{2,3}[u]_{is,i,k}^{yz} + \beta_{2,4}[u]_{is,i+1,k}^{yz}$$
(19)

This process is sometimes called interpolation, however, deconvolution is a more correct name. It shares the same coefficients as Eq. (16), that is  $\alpha_{2,i} = \alpha_{1,i}$  and  $\beta_{2,i} = \beta_{1,i}$ . We denote it as *inter-cell deconvolution* because it recovers a line-averaged from the surface-averaged velocities, *at the interfaces between* the cells. It is the momentum flux that will be convected away by  $[\overline{\nu}]_{is\ is\ k}^2$ . See [2,43] for other approximation choices.

In general, the transporting velocity  $[\overline{v}]_{is,js,k}^z$  in Eq. (18) requires a special treatment such that the numerical scheme preserves the Galilean invariant and skew-symmetric property. We just use an overbar here to designate the transporting velocity (the one effectuating the convection). The same holds true for  $[\overline{u}]_{is,js,k}^z$  that has to transport  $[v]_{is,js,k}^z$ . In other works [2,54], these transporting velocities must be computed first at the pressure cell and then interpolated to the required locations in a conservative way. Therefore, even the transported u and the transporting  $\overline{u}$  share the same position, they are obtained differently. However, FSM can freely use the transported flux as the transporting fluxes for other velocities. This fact can be easily proved by injecting the approximation formula into Eq. (17). This feature saves significant computational resources. In three dimensions, Eq. (18) still requires a nonlinear correction NC2 to achieve higher-order accuracy. If the nonlinear correction is neglected, the formal accuracy of the approximation is reduced to second-order. In 2D, the line-averaged fluxes are reduced to point fluxes and require no correction. We present an approximation of NC2 later in section 3.7. The approximation of  $[w]_{is,i,k+1}^y$  for the convection in z-direction can be done accordingly.

#### 3.3. Diffusion in x-direction

The diffusion of u in the x-direction can be computed similar to FDM. Here the compact sixth-order approximation for the second derivatives is computed by

$$\alpha_{3,1} \left[ \frac{\partial^{2} u}{\partial x^{2}} \right]_{is-1,j,k}^{yz} + \left[ \frac{\partial^{2} u}{\partial x^{2}} \right]_{is,j,k}^{yz} + \alpha_{3,2} \left[ \frac{\partial^{2} u}{\partial x^{2}} \right]_{is+1,j,k}^{yz} = \beta_{3,1} [u]_{is-2,j,k}^{yz} + \beta_{3,2} [u]_{is-1,j,k}^{yz} + \beta_{3,3} [u]_{is,j,k}^{yz} + \beta_{3,4} [u]_{is+1,j,k}^{yz} + \beta_{3,5} [u]_{is+2,j,k}^{yz}.$$

$$(20)$$

On a uniform grid,  $\alpha_{3,1} = \alpha_{3,2} = 2/(11)$ ,  $\beta_{3,1} = \beta_{3,5} = 3/(44 \triangle x^2)$ ,  $\beta_{3,2} = \beta_{3,4} = 12/(11 \triangle x^2)$  and  $\beta_{3,3} = -51/(22 \triangle x^2)$ .

#### 3.4. Diffusive flux in y- and z-direction

The diffusive flux at the top edge of the u-control surface needs a line-averaged of  $\partial u/\partial y$  on the top edge which can be approximated to sixth-order accuracy by

$$\alpha_{4,1} \left[ \frac{\partial u}{\partial y} \right]_{is,js-1,k}^{z} + \left[ \frac{\partial u}{\partial y} \right]_{is,js,k}^{z} + \alpha_{4,2} \left[ \frac{\partial u}{\partial y} \right]_{is,js+1,k}^{z} = \beta_{4,1} [u]_{is,j-2,k}^{yz} + \beta_{4,2} [u]_{is,j-1,k}^{yz} + \beta_{4,3} [u]_{is,j,k}^{yz} + \beta_{4,4} [u]_{is,j+1,k}^{yz}.$$

$$(21)$$

with  $\alpha_{4,1} = \alpha_{4,2} = 2/11$ ,  $\beta_{4,1} = -\beta_{4,4} = 3/(44\triangle x)$ ,  $\beta_{4,3} = -\beta_{4,2} = 51/(44\triangle x)$ . The reader should note the difference of this approximation from Eq. (16). In that equation, the locations where the variables live are the same. This equation delivers a deconvoluted differentiation in which the surface-averaged value is converted to a line-averaged derivative. The diffusion in z-direction can be computed similarly.

### 3.5. Non-uniform grids and boundary closures

It is customary to provide approximation coefficients in an explicit form. However, this is impractical for higher-order schemes where the closed form is inevitably obtained form Cramer's rule. The final form is tedious and expensive to compute. A more efficient way to obtain the coefficients is to calculate them by solving the Taylor expansion matrix. Detail description of the method is given in [43] and [55]. The process is straightforward and it is not discussed here.

A. Hokpunna et al. / Journal of Computational Physics ••• (••••) •••••

 $LHS_1$   $LHS_2$  $RHS_1$  $RHS_2$  $LHS_1$ :  $[u]_4^{yz}$  $LHS_2$ :  $[u]_3^{yz}$  $[u]_{3s}^z$ boundary  $[u]_2^{yz}$  $[u]_{2s}^z$  $[u]_1^{yz}$  $[u]_{1e}^z$  $[u]_1^z$  $RHS_1$ :  $[u]_{2s}^{yz}$  $[u]_{3s}^{yz}$  $RHS_2$ :  $[u]_{2s}^{yz}$  $[u]_{4s}^{yz}$ 

Closures for convection term on Dirichlet B.C.

**Fig. 5.** Positioning of variables used in the boundary closure of the u-convection in x- and y-directions. The gray area is the pressure cell and the blue-surface is the surface-averaged u. The thick lines depict the line-averaged flux needed for the convection in y-direction. The derivative du/dx is needed for the convection in x-axis and it is defined on the same position as the u itself. The LHS and the RHS variables needed for the closure are shown in diagram. The known values are marked with the circles. On the left, the knowns and unknowns are collocated while they are staggered from each other on the right.

At boundaries, the approximation stencils are not available and the information outside the domain is missing. We need a certain closure to complete the approximation and keep it accurate. The most popular approaches are (i) shift the stencil into a deeper domain and maintain the same local truncation error (LTE), (ii) use the same stencil as if the missing value exists and apply certain assumptions on them [54,56], (iii) use a reduced-order stencil near the boundary [2,4,43,57], and (iv) assume a certain feature of the field and use the most appropriate function e.g. wall-modeling. The first method is known to be unstable. Applying an assumption mismatched with the actual physics could lead to a very poor result in the second and the fourth approach. Thus we recommend the third approach.

#### 3.5.1. Boundary closures for convection

The stencil for the boundary condition at the wall is shown in Fig. 5 for the approximation of the convective terms for u-momentum in x- and y-directions.

Convection in x-direction. Even though  $[u]_{1s,j,k}^{yz}$  is specified by the wall value,  $[\partial u/\partial x]_{1s,j,k}^{yz}$  is required for Eq. (16). We recommend the third-order approximation of the wall-normal derivatives at the wall:

$$\left[\frac{\partial u}{\partial x}\right]_{1s,j,k}^{yz} + 2\left[\frac{\partial u}{\partial x}\right]_{2s,j,k}^{yz} = \frac{5}{2\triangle x}\left([u]_{2s,j,k}^{yz} - f_{bc}\right) + \frac{1}{2\triangle x}\left([u]_{3s,j,k}^{yz} - [u]_{2s,j,k}^{yz}\right)$$
(22)

which is followed by the fourth-order formula for the next derivative

$$\frac{1}{10} \left[ \frac{\partial u}{\partial x} \right]_{1s,j,k}^{yz} + \left[ \frac{\partial u}{\partial x} \right]_{2s,j,k}^{yz} + \frac{1}{10} \left[ \frac{\partial u}{\partial x} \right]_{3s,j,k}^{yz} = -\frac{6}{5\triangle x} \left( [u]_{2s,j,k}^{yz} - [u]_{1s,j,k}^{yz} \right) + \frac{6}{5\triangle x} \left( [u]_{3s,j,k}^{yz} - [u]_{2s,j,k}^{yz} \right)$$
(23)

The approximation polynomials used for the derivation are reduced from a sixth-order polynomial ( $P_6$ ) in the inner-domain to  $P_4$  and  $P_3$  towards the wall. Note that the derivative at the wall is not actually needed ( $[u]_{is,1s,k}^{yz}$  is not evolved). We just compute it to satisfy the second closure.

Convection in y-direction. The wall-value of  $[u]_{is,1s,k}^z$  is given by the boundary condition and the closure for the second position can be closed by the compact fourth-order scheme

$$\frac{1}{4}[u]_{is,1s,k}^z + [u]_{is,2s,k}^z + \frac{1}{4}[u]_{is,3s,k}^z = \frac{3}{4}[u]_{is,1,k}^{yz} + \frac{3}{4}[u]_{is,2,k}^{yz}. \tag{24}$$

It is possible to use a fifth-order closure here. However, it could be less accurate if the grid is very coarse.

#### 3.5.2. Boundary closures for diffusion

The stencil for the diffusion closures differs slightly from the convection. We do not provide a schematic here, but it is sufficient to look at the position from the previous figure. The second derivative for the diffusion in *x*-direction at the wall needs 3 cells to achieve third-order:

A. Hokpunna et al. / Journal of Computational Physics ••• (••••) •••••

 $\left[\frac{\partial^2 u}{\partial x^2}\right]_{1s,j,k}^{yz} + 11 \left[\frac{\partial^2 u}{\partial x^2}\right]_{2s,j,k}^{yz} = \left(13 f_{bc} - 27 [u]_{2s,j,k}^{yz} + 15 [u]_{3s,j,k}^{yz} - 1 [u]_{4s,j,k}^{yz}\right) / \Delta x^2$ (25)

The next unknown is closed by the fourth-order formula

$$\frac{1}{10} \left[ \frac{\partial^2 u}{\partial x^2} \right]_{1s,j,k}^{yz} + \left[ \frac{\partial^2 u}{\partial x^2} \right]_{2s,j,k}^{yz} + \frac{1}{10} \left[ \frac{\partial^2 u}{\partial x^2} \right]_{3s,j,k}^{yz} = -\frac{6}{5\triangle x^2} [u]_{1s,j,k}^{yz} + \frac{6}{5\triangle x^2} [u]_{2s,j,k}^{yz}. \tag{26}$$

Here, we use a similar order reduction as the convection closure.

The walls normal to y-axis exert a shear stress on the u-momentum and the velocity gradient at the wall can be computed by

$$\left[\frac{\partial u}{\partial y}\right]_{is,1s,k}^{z} + 6\left[\frac{\partial u}{\partial y}\right]_{is,2s,k}^{z} = -\frac{5}{3\triangle x}f_{b}c + -\frac{89}{18\triangle x}[u]_{is,1,k}^{yz} + \frac{127}{18\triangle x}[u]_{is,2,k}^{yz} - \frac{4}{9\triangle x}[u]_{is,3,k}^{yz}. \tag{27}$$

The next face is also closed by the compact fourth-order approximation

$$\frac{1}{10} \left[ \frac{\partial u}{\partial y} \right]_{is,1s,k}^{z} + \left[ \frac{\partial u}{\partial y} \right]_{is,2s,k}^{z} + \frac{1}{10} \left[ \frac{\partial u}{\partial y} \right]_{is,3s,k}^{z} = -\frac{6}{5\Delta x} [u]_{is,1,k}^{yz} + \frac{6}{5\Delta x} [u]_{is,2,k}^{yz}. \tag{28}$$

#### 3.6. Pressure gradient

0

The primary role of the pressure is to remove the non-solenoidal component which could be created from the convection term. Thus, it is reasonable to approximate the pressure force using the same method as the convection and diffusion terms. However, doing that might lead to a large stencil in the Poisson equation as mentioned earlier. On staggered grid, an explicit fourth-order pressure treatment can work with a compact fourth-order scheme very well [2]. Thus, it is not necessary to use the same scheme. The pressure treatment just has to be at least comparable to the convection and the diffusion terms. Therefore, in order to explore and find the suitable pressure treatment, we consider three approximations for the pressure gradient:

• The explicit differences:

$$\left[\frac{\partial p}{\partial x}\right]_{is,j,k}^{yz} = \beta_{5,1}[p]_{i-3,j,k}^{xyz} + \beta_{5,2}[p]_{i-2,j,k}^{xyz} + \beta_{5,3}[p]_{i-1,j,k}^{xyz} + \beta_{5,4}[p]_{i,j,k}^{xyz} + \beta_{5,5}[p]_{i+1,j,k}^{xyz} + \beta_{5,6}[p]_{i+2,j,k}^{xyz}$$

$$+ \beta_{5,6}[p]_{i+2,j,k}^{xyz}$$
(29)

with two variants:

- The fourth-order scheme with  $\beta_{5,4} = -\beta_{5,3} = 5/(4\Delta x)$ ,  $\beta_{5,5} = -\beta_{5,2} = -1/(12\Delta x)$  and  $\beta_{5,6} = -\beta_{5,1} = 0$  on a uniform grid.
- The sixth-order scheme with  $\beta_{5,4} = -\beta_{5,3} = 49/(36\Delta x)$ ,  $\beta_{5,5} = -\beta_{5,2} = -5/(36\Delta x)$  and  $\beta_{5,6} = -\beta_{5,1} = 1/(90\Delta x)$  on a uniform grid.
- The compact differences:

$$\alpha_{6,1} \left[ \frac{\partial p}{\partial x} \right]_{i_{5-1,j,k}}^{yz} + \left[ \frac{\partial p}{\partial x} \right]_{i_{5,j,k}}^{yz} + \alpha_{6,2} \left[ \frac{\partial p}{\partial x} \right]_{i_{5+1,j,k}}^{yz} = \beta_{6,1} [p]_{i-2,j,k}^{xyz} + \beta_{6,2} [p]_{i-1,j,k}^{xyz} + \beta_{6,3} [p]_{i,j,k}^{xyz} + \beta_{6,4} [p]_{i+1,j,k}^{xyz}$$

$$(30)$$

with two variants:

- The fourth-order compact difference with  $\alpha_{6,1}=\alpha_{6,2}=1/10$ ,  $\beta_{6,3}=-\beta_{6,2}=6/(5\triangle x)$  and  $\beta_{6,4}=-\beta_{6,1}=0$  on a uniform grid.
- The sixth-order compact difference with  $\alpha_{6,1}=\alpha_{6,2}=2/11$ ,  $\beta_{6,3}=-\beta_{6,2}=51/(44\triangle x)$  and  $\beta_{6,4}=-\beta_{6,1}=3/(44\triangle x)$  on a uniform grid.

The compact approximations are slightly more expensive than the explicit counterpart while greatly improve the accuracy. The coefficients of the explicit gradient on a non-uniform grid are straightforward and those of the compact gradient can be obtained from Eq. (21) and [43]. On the wall-boundary, we assume the Neumann conditions for the pressure and simply reflect the approximation coefficients.

A. Hokpunna et al. / Journal of Computational Physics ••• (••••) •••••

#### 3.7. Approximation of the nonlinear correction

The Finite Surface Method inherits the desirable conservation property of the FVM on the directions tangent to the control surfaces due to the telescoping property. However, it also inherits the nonlinear difficulties at the surfaces where  $[fg]^{x_ix_j} \neq [f]^{x_ix_j} [g]^{x_ix_j}$ . In order to achieve higher-order accuracy, we improve the approximation of the linearized convective flux by a nonlinear correction term as suggested in [2] and [50]. The fourth-order nonlinear corrections for a surface average (NC1) in Eq. (15) and the line average (NC2) in Eq. (18) are

$$NC1 = \frac{h_z^2}{12} \frac{\partial^2 u}{\partial x \partial z} \frac{\partial u}{\partial z} + \frac{h_y^2}{12} \frac{\partial^2 u}{\partial x \partial y} \frac{\partial u}{\partial y} + HOT1$$
(31)

$$NC2 = \frac{h_z^2}{12} \frac{\partial v}{\partial z} \frac{\partial u}{\partial z} + HOT2 \tag{32}$$

Since this correction is second-order, any second-order approximation to the derivatives is sufficient to achieve a fourth-order correction. A recommended practice is to compute the derivatives from the linear fluxes already obtained. A study on choices for the nonlinear correction has been done in [58]. Taylor's expansion can be used to obtain arbitrary order correction. However, this can result in a lengthy formulation. The Taylor's expansion indicates that a sixth-order nonlinear correction for *NC*1 must eliminate 11 terms. Nevertheless, it can be achieved with the following formula:

$$NC1 = NC1_y + NC1_z + HOT_y + HOT_z + HOT_{yz} + O(h^6)$$
(33)

$$NC1_{y} = \frac{1}{48} A_{y,h}(J) \tag{34}$$

$$NC1_{z} = \frac{1}{48} A_{z,h}(J) \tag{35}$$

$$HOT_{y} = \frac{11}{720} \left( \frac{1}{4} A_{y,h}(J) - \frac{1}{16} A_{y,2h} J \right) + \frac{1}{720} A_{y,h}^{2}(J)$$
(36)

$$HOT_{z} = \frac{11}{720} \left( \frac{1}{4} A_{z,h}(J) - \frac{1}{16} A_{z,2h}(J) \right) + \frac{1}{720} A_{z,h}^{2}(J)$$
(37)

$$HOT_{yz} = \frac{1}{2304} E_{z,h} \left( E_{y,h} \left( [u]_{is,j,k}^{yz} \right) \right) E_{z,h} \left( E_{y,h} \left( \left[ \frac{\partial u}{\partial x} \right]_{is,j,k}^{yz} \right) \right)$$
(38)

$$J = \left( [u]_{is,j,k}^{yz}, \left[ \frac{\partial u}{\partial x} \right]_{is,j,k}^{yz} \right) \tag{39}$$

where  $A_{y,h}\left(f_{i,j,k},g_{i,j,k}\right)$  defines a multiplication of the central difference along the y-direction of f and g using h distance from the point of differencing i.e.  $A_{y,h}\left(f_{is,j,k},g_{is,j,k}\right)=E_{y,h}\left(f_{is,j,k}\right)$   $E_{y,h}\left(g_{is,j,k}\right)$ . The operator  $E_{y,h}$  is the central differencing operator i.e.  $E_{y,h}(f_{i,j,k})=f_{i,j+1,k}-f_{i,j-1,k}$ . The square represents the second-order central difference e.g.  $E_{x,h}^2(f_{i,j,k})=f_{i-1,j,k}-2f_{i,j,k}+f_{i+1,j,k}\neq E_{x,h}\left(E_{x,h}(f_{i,j,k})\right)$ . The term  $A_{y,h}^2$  is also the multiplication of the two second-order differences. The first two terms,  $NC1_y$  and  $NC1_z$  are the second-order approximation of the derivatives in Eq. (31). This approximation can be adopted for NC2. This sixth-order nonlinear correction can be used for higher-order FVM as well. It is also possible that there exists a better way to compute a higher-order correction. However, it will be shown later that the nonlinear correction can be omitted in turbulent flow. Thus, we do not exhaustively search for other possibilities.

#### 3.8. Aliasing error management

In smooth laminar flow, the FSM with the convective form is stable and very accurate. In turbulent flow, we found that the solutions are stable on reasonable grids, however they converge to the reference solution in a non-monotonic way. This non-monotonic convergence stems from the aliasing error in the convective term. In spectral methods, this problem is solved by computing the convective term on a larger space and then truncate the result back to the original space. Higher-order methods are known to be strongly affected by aliasing errors [51]. If these aliasing errors are not managed, it can corrupt the accuracy of the calculations or even destabilize the calculation entirely. In non-spectral schemes, this aliasing error can be managed by using fully conservative schemes such that the  $L_2$ -norm of the velocity is bounded, or applying a filter. In this work, we apply a mild low-pass filter before computing the convective term. It is done by using a simple compact interpolation to interpolate the velocity to the cell-center and then interpolate them back to the original positions. Here we use a simple sixth-order compact interpolation (see [1]). The leading complexity of the sixth-order double interpolation is 24N per axis. The transfer function of this double interpolation is displayed as F6 in Fig. 6 along with the resolving efficiency  $e = kh_{max}/\pi$  where  $|1 - T(kh)| \le \varepsilon$ , of other linear terms.

Please cite this article in press as: A. Hokpunna et al., Finite surface discretization for incompressible Navier-Stokes equations and coupled conservation laws, J. Comput. Phys. (2020), https://doi.org/10.1016/j.jcp.2020.109790

a

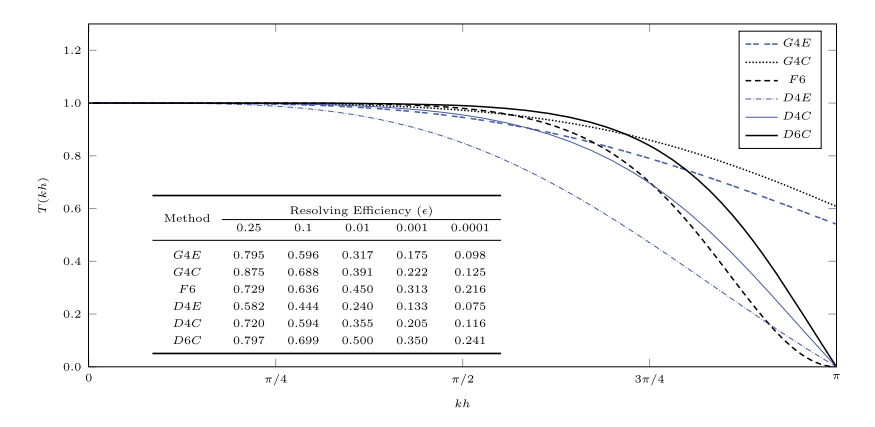


**Fig. 6.** Transfer functions of linear approximations; G4E: explicit fourth-order pressure gradient (Eq. (29)), G4C: compact fourth-order pressure gradient (Eq. (30)), F6: filtering by a sixth-order double interpolation, D4E: explicit fourth-order inter-cell differentiation, D4C: compact fourth-order inter-cell differentiation, D6C: compact sixth-order inter-cell differentiation (Eq. (16)). Note that, the collocated differentiation (Eq. (16)) and the inter-cell deconvolution (Eq. (19)) are equivalent and they are shown here as one (D6C). The D4E and D4C use a reduced form of (Eq. (16)).

#### 4. Mass and momentum conservations decoupling

The projection method [14,15,59] is used to decouple the mass conservation equation from the momentum equation and we solve the NSE using the following steps:

1. Integration of the momentum equation:

$$\mathbf{u}^* = \mathbf{u}^n + \left(\mathcal{H}(\mathbf{u}^n) - \frac{1}{\rho}\mathbf{G}p^n\right)\Delta t \tag{40}$$

2. Projection step:

$$\mathbf{L}\phi = \frac{\rho}{\Delta t}\mathbf{D}\mathbf{u}^* \tag{41}$$

$$\mathbf{u}^{n+1} = \mathbf{u}^* - \frac{\Delta t}{\rho} \mathbf{G} \phi \tag{42}$$

$$p^{n+1} = p^n + \phi \tag{43}$$

where  $\mathcal{H}$  is the net numerical convection and diffusion operator. The above procedures are performed for each RK substep. The projection method (Eq. (41) to Eq. (43)) acts as a projection operator  $\mathbf{P} = \mathbf{I} - \mathbf{G}(\mathbf{L})^{-1}\mathbf{D}$  to  $\mathbf{u}^{n*}$ . This projection requires a solution of Poisson equation in Eq. (41) whose Laplacian is given by  $\mathbf{L} = \mathbf{D}\mathbf{G}$ , the multiplication of the divergence ( $\mathbf{D}$ ) and gradient ( $\mathbf{G}$ ) operators. The choices of these two approximations determine the discrete Laplacian. Additional information on the projection method can be found in [44,59].

Equation (41) can be solved by direct or iterative methods. When a homogeneous direction is present, an application of FFT solver is very efficient. For general domains, one must use an iterative solver. In our code, we use a classic strongly implicit procedure (SIP) [60]. The SIP kernel is a first-order approximation to the second-order accurate discrete Laplacian. It is a very effective smoother for the fourth-order Laplacian. For a very low divergence, multigrid method must be used to solve the system within a reasonable time.

#### 4.1. Discrete Poisson operator

In term of pressure calculation, the first advantage of the finite-surface method over FDM and FVM is that it offers the smallest possible stencil of the projection Laplacian. This is because the divergence operator  $\mathbf{D}_{xi}$  is reduced to a difference operator  $\mathcal{E}_x = [-\delta_{i,j,k} \ \delta_{i+1,j,k}]/\triangle x_i$  and the Laplacian becomes

$$\mathbf{L}_{\mathbf{X}}\boldsymbol{\phi} = \mathcal{E}_{\mathbf{X}}\mathbf{G}_{\mathbf{X}}\boldsymbol{\phi} \tag{44}$$

The 1D Laplacian stencil can be directly constructed from the difference of the two consecutive pressure gradients e.g.  $\left[\left(\frac{\partial p}{\partial x}\right)_{is+1,j,k}^{yz} - \left[\frac{\partial p}{\partial x}\right]_{is,j,k}^{yz}\right]/\triangle x_i$  from Eq. (29). On a uniform grid, the corresponding fourth-order Laplacian in the *x*-direction becomes

$$\mathbf{L}_{4E,x}\phi = \mathcal{E}_{x}\mathbf{G}_{x}\phi = \frac{1}{12\triangle x^{2}} \left( 30 \left[\phi\right]_{i,j,k}^{xyz} - 16 \left[\phi\right]_{i\pm 1,j,k}^{xyz} + \left[\phi\right]_{i\pm 2,j,k}^{xyz} \right). \tag{45}$$

A. Hokpunna et al. / Journal of Computational Physics ••• (••••) •••••

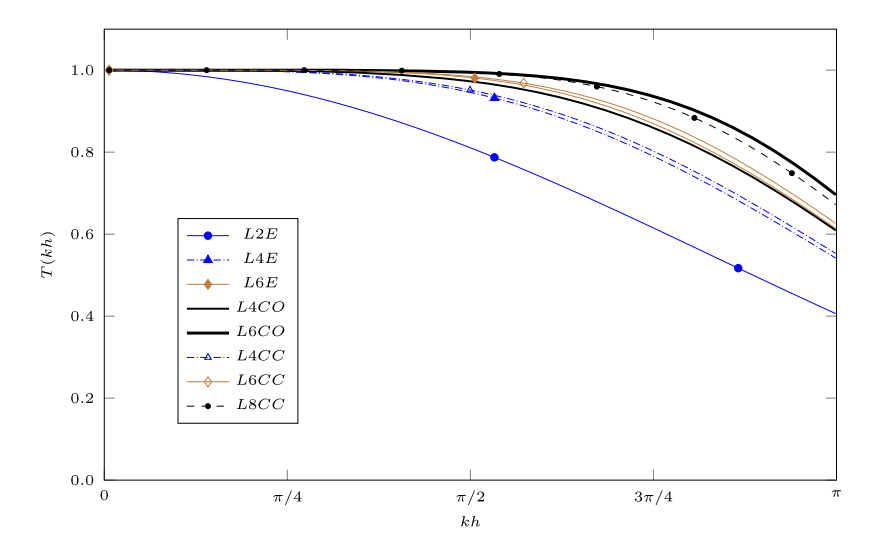


Fig. 7. Transfer functions of the discrete Laplacians; L4E: explicit fourth-order, L6E: explicit sixth-order, L4CO: compact fourth-order, L6CO: compact sixthorder, L4CC: fourth-order cell-centered, L6CC: sixth-order cell-centered, L8CC: eight-order cell-centered.

Table 1 Leading term of the complexity in evaluating 3D discrete Laplacians and their one-dimensional resolving efficiency.  $N_t$  is the number of total pressure cell i.e.  $N_t = N_x N_y N_z$ .

Method	Leading term of	Resolving	efficiency (e)	
	complexity $(N_{op})$	0.1	0.01	0.001
FSM-L2E	13 <i>N</i> <sub>t</sub>	0.356	0.110	0.035
FSM-L4E	$25N_t$	0.596	0.317	0.176
FSM-L6E	$37N_t$	0.706	0.446	0.296
FSM-L4CO	$27N_t$	0.688	0.391	0.222
FSM-L6CO	$39N_t$	0.809	0.555	0.383
FSM-L4CC	$37N_t$	0.611	0.329	0.183
FVM-L6CC	$61N_t$	0.722	0.461	0.307
FVM-L8CC	$85N_t$	0.784	0.545	0.395

Consequently, the number of stencil points in 3D is 13 which is the smallest explicit approximation of the fourth-order accurate Laplacian. Note that this number in the fourth-order projection of FVM and FDM is 25 on collocated grids and 19 on staggered grids.

When the pressure gradient is approximated using a compact differentiation, it is impractical to store a full matrix  $\mathbf{L}_X = \mathcal{E}_X (\mathbf{A}_X^{-1} \mathbf{B}_X)$  where  $\mathbf{A}_X$  and  $\mathbf{B}_X$  is the approximation matrix for the pressure gradient in Eq. (30). However, most of the iterative algorithms solving the multidimensional Poisson equation rarely need the actual form of the discrete Laplacian. It is sufficient to just evaluate the Laplacian of the solution, thus we only need to store the banded matrices  $A_x$  and  $B_x$  and use them to compute the Laplacian of the incremental pressure by solving the RHS of

$$\mathbf{L}_{4CO,x}\phi = \mathcal{E}_{x}\left(\mathbf{A}_{x}^{-1}\mathbf{B}_{x}\phi\right),\tag{46}$$

with Gaussian elimination. Evaluating this equation for a fourth-order compact scheme costs 9N operations on a nonuniform grid for N being the number of cells in x-axis. This is 2N more than Eq. (45). However, on a non-uniform grid the cost of computing  $L_{4E}$  is increased to the same number -9n. Finally, in a 3D non-uniform grid, computing the Laplacian with the compact fourth-order scheme costs 27N while the fourth-order explicit Laplacian costs 25N. The transfer functions of the Laplacians in Fig. 7 show that the cell-centered (CC) Laplacian (on staggered FVM) is slightly more accurate than FSM, at the same order of convergence. The corresponding costs are listed in Table 1 together with the resolving efficiency. It can be argued in terms of performance that, FSM is faster than FVM at the same level of accuracy, but the advantage is marginal. In the next section we demonstrate why the pressure treatment on FSM is better than the staggered FVM, even on the same grid.

#### 5. Combined effects of the Laplacian and divergence operators

The numerical divergence can be written in a discrete form as  $\widetilde{div} = (\mathbf{D}_x + \mathbf{D}_v + \mathbf{D}_z) \mathbf{u}^*$ . The tilde indicates that the variable is an approximation. We can apply the Fourier transformation to Eq. (41) and arrive at:

Table 2
Transfer functions of different discrete Laplacians under finite surface and finite volume methods. L4E: explicit fourth-order, L6E: explicit sixth-order, L4CO: compact fourth-order, L6CO: compact sixth-order, L4CC: fourth-order cell-centered, L6CC: sixth-order cell-centered and L8CC: eight-order cell-centered.

Method	Transfer function $(T_L(kh))$
FSM-L2E	$[2-2\cos{(kh)}]/[k^2h^2]$
FSM-L4E	$[15 - 16\cos(kh) + \cos(2kh)]/[6k^2h^2]$
FSM-L6E	$[245 - 270\cos(kh) + 27\cos(2kh) - 2\cos(3kh)]/[90k^2h^2]$
FSM-L4CO	$[12(1-\cos{(kh)})]/[k^2h^2(\cos{(kh)}+5)]$
FSM-L6CO	$[3(17-16\cos(kh)-\cos(2kh))]/[2k^2h^2(4\cos(kh)+11)]$
FVM-L4CC	$[(27\sin(kh/2) - \sin(3kh/2))^2]/[12kh]^2$
FVM-L6CC	$[(2250\sin(kh/2) - 125\sin(3kh/2) + 9\sin(5kh/2))^{2}]/[960kh]^{2}$
FVM-L8CC	$[-75sin(7kh/2) + 1029sin(5kh/2) - 8575sin(3kh/2) + 128625sin(kh/2)]^2 / [53760kh]^2$

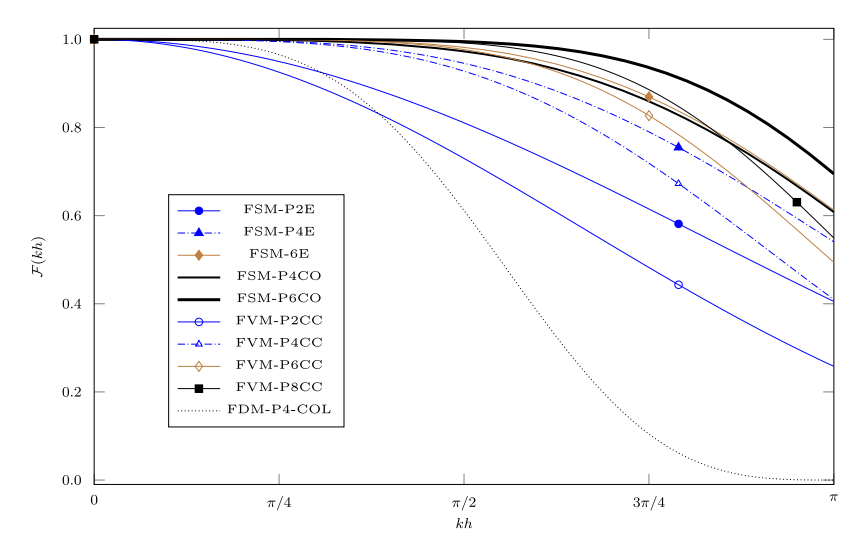


Fig. 8. Mass conservation factor as a function of wave number. Here two additional schemes presented: the second-order cell-center method (2CC) and the explicit fourth-order pressure treatment on collocated grid (FDM-P4-COL). The other schemes are named as in Fig. 7.

$$\widehat{\phi}_{kx,ky,kz} = -\frac{T_{Dx}(k_x) + T_{Dy}(k_y) + T_{Dx}(k_z)}{T_L(k_x)k_x^2 + T_L(k_y)k_y^2 + T_L(k_z)k_z^2} \, \widehat{div}_{kx,ky,kz}. \tag{47}$$

Thus, the accuracy of the mass-conservation and the pressure term is a combination of two parts: (i). the divergence computation and (ii). the approximation of the Poisson operator. If we accept that,  $T_D$  determines the amount of the useful information that will be available from the divergence calculation and  $T_L$  determines how much we could salvage the correct pressure out of the discrete Laplacian. The combination of these two would represent the effective mass conservation and thus we define the *mass-conservation factor* for the projection method as

$$\mathcal{F}_{D,L}(kh) = T_D(kh)T_L(kh). \tag{48}$$

The exactness of the divergence calculation in the FSM improves the overall accuracy of the incremental pressure. First, the  $T_D$  above is unity because it is exact. Second, the transfer function of the Laplacian is actually formed by  $T_L = T_D T_G$ . Therefore, the accuracy of the Poisson equation is improved as well. In finite volume and finite difference methods, the mass-conservation factor is the cubic of the transfer function of the first derivative approximation—provided that the gradient and the divergence are computed with the same scheme. One of the terms comes from the divergence approximation and the other two come from the Laplacian. In FSM, we only approximate the derivative once for the pressure gradient, but the divergence calculation is exact. Thus the only approximation determining the accuracy of the mass conservation and the pressure in FSM is the approximation of the pressure gradient.

We plot the mass-conservation factor in Fig. 8. Note that all of the factors in FSM are the same as the transfer functions shown previously in Fig. 7. The factor of the FVM, on the other hands, drops significantly. The curve of FVM-P2CC is separated from the FSM-P2E whereas they were exactly the same when consider only the Laplacian (L2E in Fig. 7). All of the explicit pressure treatments are clearly better with FSM.

We can define a mass conservation efficiency similar to the resolving efficiency. Thus, let us consider the mass conservation efficiency,  $e_m = kh_{max}/\pi$  where  $|1 - \mathcal{F}_{D,L}(kh)| \le \varepsilon$ . The result is listed in Table 3. This mass conservation efficiency tells us how much of the Nyquist limit, the projection method can cover w.r.t. the given relative error  $\varepsilon$ . In this table, the number in the acronym indicates the order of accuracy. The letters E and CO stand for the explicit and the compact scheme

A. Hokpunna et al. / Journal of Computational Physics ••• (••••) •••••

#### Table 3 Mass conservation efficiency of a selected pressure treatments for FSM and the staggered FVM. Here, the acronym L is replaced by P to represent the overall pressure treatment.

Method	Mass cons	ervation effi	ciency $(e_m)$	
	$\epsilon = 0.25$	$\epsilon = 0.1$	$\epsilon = 0.01$	$\epsilon = 0.001$
FVM-P2CC	0.478	0.291	0.090	0.028
FSM-P2E	0.583	0.356	0.110	0.035
FVM-P4CC	0.722	0.548	0.296	0.165
FSM-P4E	0.795	0.596	0.317	0.176
FSM-P4CO	0.875	0.688	0.391	0.222
FVM-P6CC	0.818	0.666	0.429	0.286
FSM-P6E	0.889	0.706	0.446	0.296
FSM-P6CO	0.959	0.809	0.555	0.383
FVM-P8CC	0.870	0.733	0.514	0.374

under FSM, respectively. CC stands for the cell-centered scheme used exclusively in staggered FVM. The frequency windows for capturing fine scales of the second-order pressure treatment are 22% wider in FSM. This advantage is reduced to 9% and 6% in fourth- and sixth-order, respectively. Note that the costs of evaluating the explicit fourth-, sixth- and eighth-order Laplacians are 48%, 65% and 73% more expensive in FVM, compared to the FSM counterpart. Thus for explicit schemes, the mass conservation is much more efficient with FSM. In contrast to this, the compact treatment of the pressure is even more attractive. FSM-P4CO is more accurate than the sixth-order cell-center treatment (FVM-P6CC) at high wave number. The cost of the pressure treatment in FSM is not only less, the richer information on the mass imbalance allows keeping the velocity solenoidal to a higher degree than in FVM.

The mass-conservation factor at the lowest level ( $\varepsilon = 0.25$ ) is interesting. This level of relative error sounds quite large in general, but in a broad spectrum flow it is inevitable. The resolving efficiency of FSM-P4E at this level is 79.5%, and the accumulated error is less than 4% on a flat spectrum. Also, this resolving efficiency is comparable to the sixth-order approximation of the convective term (D6C) in Fig. 6. At smaller tolerance, this pressure treatment is less accurate. Thus in a broad spectrum flow where the small structures are not fully resolved, the dominant error could be coming mainly from them. In such situation, FSM-P4E can accompany the sixth-order FSM without loosing accuracy. A quantitative analysis of this issue will be given later in section 7.

#### 6. Validation

In this section, we verify the accuracy of the finite surface method using four standard test cases and focus on how the pressure treatment affects the overall accuracy of the compact sixth-order FSM. The convection and the viscous terms are approximated by sixth-order schemes in all test cases and the time-integration is third-order low-storage Runge-Kutta (RK) [61]. The approximations of the pressure gradient considered here are (i), the fourth-order explicit (PE4), (ii), the compact fourth-order (PCO4), and (iii). the compact sixth-order (PCO6) methods. The Poisson equations are solved by a direct FFT solver using a transfer function listed in Table 2. In the domain having both periodic and non-periodic, the eigendecomposition is employed where we solve a banded matrix for each pair of xy-eigenmode. All the simulations in two dimensions are computed with the sixth-order nonlinear correction without any filtering process. The method is implemented on MGLET [2] developed at Technische Universität München.

First a Taylor-Green vortex (TGV) flow is used to investigate the accuracy of the individual components of the momentum equations including the pressure. Next, a double shear layer (DBL) flow is used to verify the convergence in a fully nonlinear flow. The boundary closures are then evaluated using an instability in plane channel flow a and lid-driven cavity flow. The divergence error  $(div \cdot L_{ref}/U_{ref})$  is in the range of 1E-15 for the simple TGV flow and the instabilities in plane channel flow. In the DBL problem, the divergence is in the order of 1E-14 on the coarsest grid and 1E-13 on the finest grid  $(N = 512^2)$ . In the lid-driven cavity flow, an iterative solver is used and the divergence is kept in the vicinity of 1E-11.

#### 6.1. Taylor-Green vortex flow

A family of Taylor-Green vortex flows can be described by

$$u(x, y, t, Re) = c_x - \cos(x - c_x t)\sin(y)e^{\frac{-2t}{Re}}$$
(49)

$$v(x, y, t, Re) = c_y + \sin(x - c_y t)\cos(y)e^{\frac{-2t}{Re}}$$
(50)

$$p(x, y, t, Re) = -\frac{1}{4}(\cos(2(x - c_x t)) + \cos(2(y - c_2 t)))e^{\frac{-2t}{Re}}.$$
 (51)

**Fig. 9.** Convergence of FSM: (a) the initial projected pressure in the inviscid TGV, (b) the convergence of u and p in the traveling TGV at  $t=2\pi$ . Every simulation is performed with CFL=0.013 except for the addition test stated in the graph (CFL=0.2). The y-axis is shared by both graphs.

In this study, the domain is set to  $(x, y) \in [0, 2\pi]^2$  with the periodic boundary conditions. This test case has been widely used in literature. The classical TGV ( $c_x = c_y = 0$ , Re = 100) is a popular tool to demonstrate the convergence of NSE solver. On uniform grids, central schemes from the FDM and FVM produce accidental error cancellations where the convective fluxes are canceled out exactly by the pressure force and the flow will be scaled down by the viscosity. Ultimately, under these conditions, the pressure from the projection method will be exact, regardless of the order of the numerical scheme. FSM does not have that cancellation and the errors thus remain at the local truncation error.

#### 6.1.1. Stationary inviscid TGV

First, we check the accuracy of the pressure treatment using the stationary inviscid TGV:  $c_x = c_y = 0$ ,  $Re = \infty$  by initializing the velocities with exact values but using the wrong pressure. The cell-averaged pressure value is replaced by the pointwise value at the cell center. This mimics the situation when the velocity field is accurately known, but the pressure is less accurate or unknown. This tests the ability to recover the pressure by the different treatments mentioned previously.

All the approximations of the convection and diffusion terms are computed with full sixth-order except for the pressure gradient. We perform just a single time integration to check the recovered pressure. The convergence curves of the new pressures indicate that the explicit fourth-order treatment (PE4) is the least accurate (Fig. 9(a)), as expected. Its error is 2.6 times larger than the compact fourth-order (PCO4) while the sixth-order compact scheme (PCO6) is much more accurate. Both fourth-order treatments are <u>not</u> good enough to formally deliver the sixth-order accurate initial pressure. However, it is possible for the fourth-order schemes to recover the correct initial pressure, similar to that of PCO6. This can be done by iterating the NSE solver for several iterations using a very small time-step, e.g. 1E-6  $L_{ref}/U_{ref}$ . This only need to be done once at the beginning of the simulation. It will be demonstrated later that, if the initial pressure is correct, PE4 and PCO4 will be as good as PCO6.

### 6.1.2. Traveling-viscous TGV

Next, we enable the convection and viscous terms by setting  $c_x = 1.0$ ,  $c_y = 0$ , Re = 100. The time step is adapted such that CFL number is kept at 0.013 to ensure that the time integration errors are smaller than the spatial approximation errors. The initial pressure is initialized exactly using the cell-averaged values. The new TGV is now moving along the x-axis and is scaled down with time. The pressure field is thus traveling and decays along with it. The maximum errors are plotted in Fig. 9(b) at  $t = 2\pi$  when the flow has completed a round-trip and decayed by 12%. At this point, both convection and diffusion have made substantial contributions to the velocity. The differences between the errors in the pressures of PE4 and PCO4 are the same as shown previously. However, their velocities are almost identical (We remove PCO4 for clarity). The number of grid points per wavelength (PPW) in the graph ranges from 10 on the right to 600 on the left.

All treatments deliver a clear sixth-order convergence rates in the velocity. The averaged rate from 10 to 160 PPW is 6.42. At 200 PPW, the error in the velocity at the first time step is 1.2E-15, which is just five times the machine accuracy ( $\epsilon$ ). The solution is thus affected by the accumulated round-off errors and the convergence is halted. The last two errors in the graph are very close to machine accuracy times the number of time steps ( $NT \times \epsilon$ ). The sixth-order convergence rate can be recovered again by switching to quadruple precision (not shown). In our early study, we initialized the pressure using the point value as we did with the inviscid TGV. In that study, we found that PE4 and PCO4 deliver the sixth-order

A. Hokpunna et al. / Journal of Computational Physics ••• (••••) •••••

accurate momentum up to 15 point-per-wave-length (PPW) and the convergence rate degraded to fourth-order. However, once the pressure was initialized correctly, the momentums obtained from all the pressure treatments are virtually the same as shown here.

We attempt to expose whether the fourth-order pressure treatments benefited from the small CFL by redoing the case again with CFL = 0.2. This is a reasonable number for general CFD simulation. The error in the momentum of PE4 is shown by the filled triangles and the end convergence rate is third-order. This is, however, not the deficit of the PE4. The reason for the third-order convergence rate is actually the time-integration scheme which was third-order (accumulated error). Nevertheless, at lower resolutions we see the convergence rate of 5.1 and 4.6 for the first three grids. The PPW of these three grids are: 10, 15 and 20 and the simple sine wave of the velocity can be considered very well resolved at these resolutions. We conclude that at finer grids, the error by the third-order RK becomes dominant at  $CFL \ge 0.2$ . Thus, in order to achieve a full sixth-order, the time-step size must be small enough or a higher-order time-integration should be used.

#### 6.2. Doubly periodic double shear layers flow

This simple two dimensional flow contains Kelvin-Helmholtz instabilities in which the shear layers are perturbed by a sinusoidal disturbance leading to a roll-up of the vortex sheets into a cone-like shape. The periodic domain  $\Omega = [0, 1]^2$  is taken for this study and the initial velocities are given by

$$u = \begin{cases} \tanh(\sigma(y - 0.25)) & \text{for } y \le 0.5, \\ \tanh(\sigma(0.75 - y)) & \text{for } y > 0.5, \end{cases}$$
 (52)

$$v = \gamma \sin(2\pi x). \tag{53}$$

The Reynolds number based on the initial maximum velocity and the length of the computational domain is 10,000. The shear layer parameter ( $\sigma$ ) and the perturbation magnitude ( $\gamma$ ) are set to 30 and 0.05, respectively. This setting is similar to a *thick shear-layer problem* studied in [62]. The number of cells used in this study is  $N=(i\times 64)^2$  for i=1..8. The error is measured against the result of the finest resolution. The time-step size is refined as the number of grid point is increased. The CFL is set in the range of 0.03 < CFL < 0.06, in order to keep the time-integration error low. The overview of the simulations shown in Fig. 10 illustrates how the shear layers get rolled up by the spanwise perturbations at a relatively fast pace. On the  $64^2$ -grid, the numerical artifacts appear everywhere, most notably on the level close to zero vorticity ( $\omega_z=0$ ). However, the tails of the vortex sheet are still clearly preserved. When the grid resolution is tripled in each direction, some artifacts can still be observed at t=0.8, but they have completely disappeared at t=1.2.

Finite volume and finite surface methods suffer additional difficulty due to the nonlinear convective fluxes. A nonlinear correction is a simple method that can solve this problem at a significant cost (in sixth-order context). If its contributions are insignificant, we could turn it off and save some computing resources. Thus we check the contributions of the nonlinear correction at t=0.4. The averaged norms of each contribution are plotted in Fig. 11(a) showing that the contribution of the nonlinear correction ( $\mathcal{NC}$ ) is getting smaller as the grid is refined. At the coarsest grid, the nonlinear correction is about a magnitude smaller than the diffusion and it is five orders of magnitude smaller than the linearized convection term ( $\mathcal{C}$ ). The norm of the nonlinear correction converges at second-order rate which agrees well with the local truncation error. We further check the contribution ratio of the other terms relative to the nonlinear correction at the position of the maximum nonlinear correction (Fig. 11(b)). At this point, the value of  $|\mathcal{C}/NC|$  is in the range of 21 – 475 which means NC contributes at most the second or the third significant digit of the linearized convection. In term of the total change in the momentum, the linearized convection contributes about 73.5% on the finest grid. The diffusion contributes 8% and the pressure's contribution is 18.4%. The nonlinear correction contributes less than 0.1% of the total momentum change on the cell where its value is maximum.

The convergence rate of the global error of the streamwise velocity is plotted in Fig. 12 at t = 0.4. The results of this convergence test demonstrate that the fourth- and sixth-order pressure treatments deliver almost the same convergence rate. The marks of PCO4 fit very well within PCO6's marks while those of PE4 coincide at first and slightly fell off after  $N=192^2$ . The averaged convergence rates ( $R_a$ ) of PCO4 and PCO6 are sixth-order and PE4 follows closely at 5.83. To investigate why the fourth-order pressure treatments can deliver a sixth-order convergence for this flow, we subtract the streamwise velocity of PE4 and PCO4 from PCO6 and plot their norms in Fig. 12. The convergence curves of the differences clearly show that the sixth-order convergence rates of PE4 were possible because the treatment of pressure is more accurate than the convective term at low resolutions. As the resolution increases, the sixth-order convergence of  $\mathcal H$  eventually catches up after  $N = 320^2$ . We see earlier in Fig. 10 that the solution of this flow is already smooth at  $N = 192^2$  and the errors on this grid are already less than  $10^{-5}u_{max}$ . Therefore, the ability of PE4 to accompany the sixth-order schemes of the momentum term up to  $N = 320^2$  is very impressive. Using PE4 can save a lot of effort in upgrading older codes as well as saving computing time because the sixth-order pressure treatment can cost 50% more when the pressure is solved by iterative methods. In an extremely accurate simulation where PE4 is insufficient, PCO4 could still work at a small additional cost. Initially, the convergence rate of  $|u_{co4} - u_{co6}|$  starts at 5.69 and the average rate from  $N = 64^2$  to  $192^2$  is 6.7. After that, the rounding errors interfere. In this particular problem, the difference between PCO4 and PCO6 on very fine grid was actually limited by the machine accuracy instead of the treatment of the pressure.

0.5

0

0.5

х

0.5

0.5

0.5

0.5

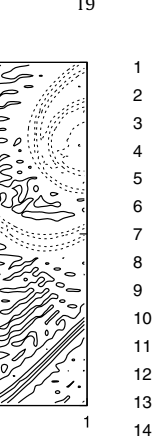
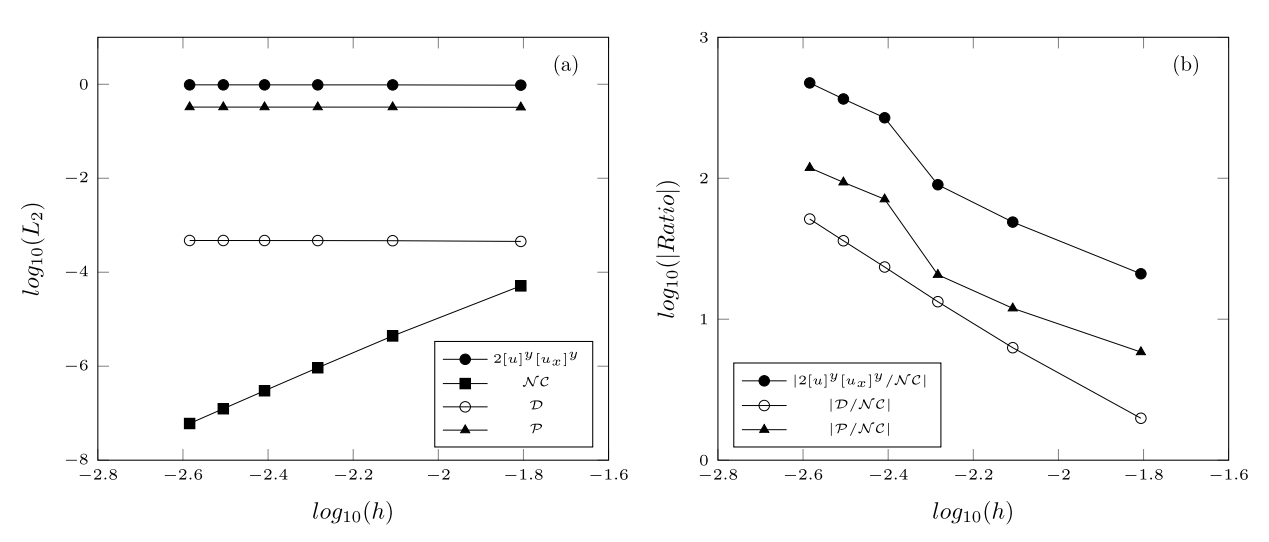




Fig. 10. An overview of the vorticity (-30:6:30) of the double shear layers flow with  $N = 64^2$  (top) and  $192^2$  (bottom) at t = 0.4, 0.8 and 1.2, from left to right respectively. The solid lines represent the positive contours and the dashed line means negative vorticity.

0.5

0.5



**Fig. 11.** The contribution of convection, diffusion and pressure terms at t = 0.4. (a) An averaged  $L_2$  of the linearized convection term  $(2[u]^y[u_x]^y)$ , diffusion term  $(\mathcal{D})$ , the pressure term  $(\mathcal{P})$  and the nonlinear correction  $(\mathcal{NC})$ . (b) The norm of each term in the momentum equation normalized by  $|\mathcal{NC}|$  at the position of  $|\mathcal{NC}|_{\infty}$ .

We continue to evolve the flow to t = 1.2 and check the maximum error globally. In Fig. 13, the errors from every pressure treatment are clustered very closely. The u-convergence of the full sixth-order (PCO6) starts off at R = 3.26 and increases until reaching the end convergence rate at  $R_e = 5.81$  while the end convergence rate of  $\nu$  is slightly lower at  $R_e = 5.74$ . A better number is observed for p with  $R_e = 5.97$ . PCO4 coincides with the POC6's marks. The error in u of PE4 is at most 12% higher than PCO6 while that of the pressure is 10% higher on the coarsest grid and increases to 81% at the finest grid. PE4 also has a lower convergence in p, however, the error level is still significantly below that of the

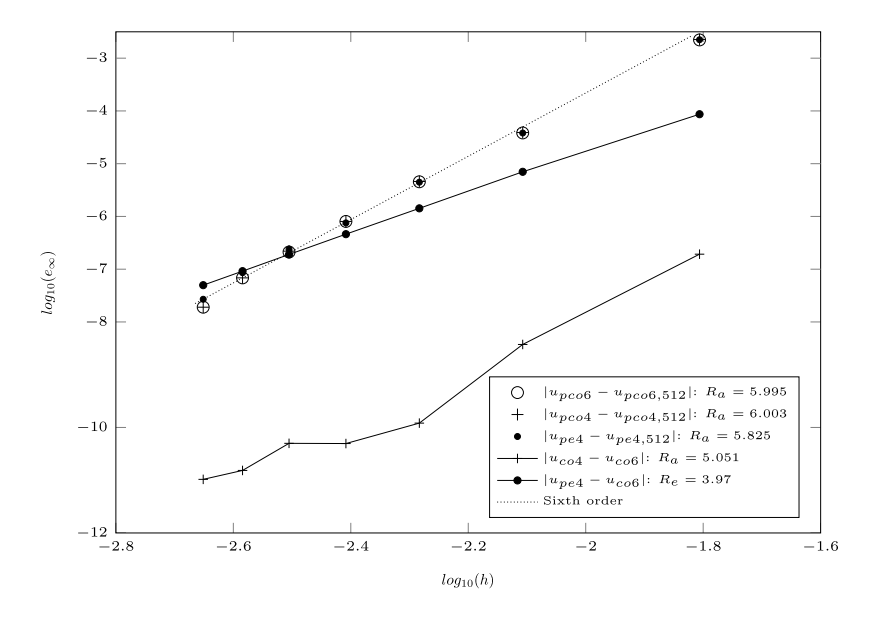


**Fig. 12.** Convergence of global streamwise velocity error in the doubly periodic double shear layers flow at t = 0.4 from different pressure treatments. The symbols are the convergence plot measured against finest grid of the respective pressure treatment. The lines with symbol depict the errors measured against the sixth-order pressure treatment (PCO6). The numerical convergence rates at the beginning  $(R_a)$  and the end  $(R_e)$  are shown in the legend.

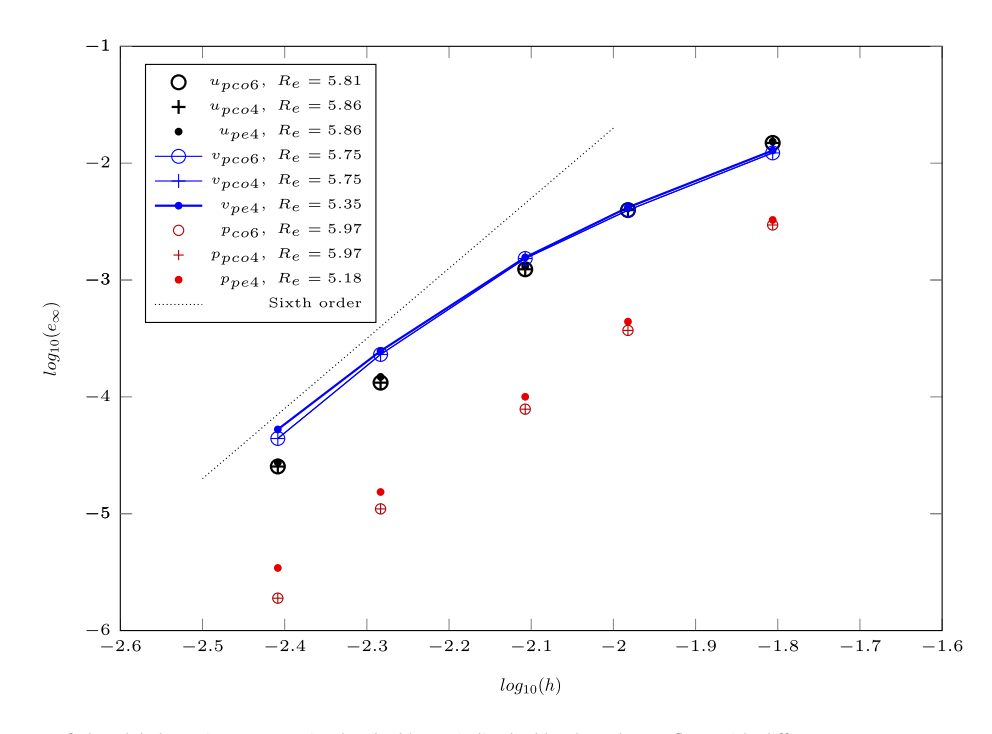


Fig. 13. Convergence of the global maximum error in the doubly periodic double shear layers flow with different pressure treatment at t = 1.2. The fourth-order pressure treatment can deliver a sixth-order apparent convergence rate.

momentum and allows a very accurate velocity. The break-even point between the fourth-order pressure and the sixthorder momentum has not yet been reached in the grids tested here. We checked the differences of PE4 and PCO4 w.r.t. PCO6 on the  $256^2$ -grid and found that u-velocity errors are 5E-6 and 7E-9, respectively. The errors are dominated almost purely by the convective term. FSM can thus advance the solution accurately while using a fourth-order treatment of the pressure and deliver an apparent sixth-order convergence rate. In comparison to other higher-order methods, at t = 0.4, the error of FSM on the coarsest grid is 120-times smaller than the fourth-order FDM [62] on the coarsest grid (2.2E-3 vs. 0.27). The error level of the FSM on our coarse grid is actually just 38% more than the fourth-order FDM [62] with  $N = 256^2$  grid points. At t = 1.2, the error ratio between the fourth-order FVM [2] and the FSM is 1.7 on the coarsest grid increases to

# 

# 

# 

#### 

Table 4

Converge	nce study in y-direction of	of the instability of plane channel flow on uniform	grid with $N_x = 64$ . The table shows
growth-ra	ates of perturbations $(G_n)$ ,	their errors $(\varepsilon_n)$ relative to the linear stability the	ory. The averaged convergence rates
measured	l from the overall range w	hile the final rate measured using the last two grid	s.
Nv	Growth rate	Error	Convergence rate

$N_y$	Growth rate		Error		Converge	nce rate
	Final	Average	Final	Average	Final	Average
64	5.3500E-03	5.1405e-03	8.8004e-04	6.7058e-04	=	_
96	4.5641E-03	4.5356e-03	9.4132E-05	6.5596e-05	5.51	5.73
128	4.4843E-03	4.4786e-03	1.4340E-05	8.5925e-06	5.94	6.29
144	4.4762E-03	4.4734e-03	6.2254E-06	3.4368e-06	6.11	6.50
160	4.4727E-03	4.4713e-03	2.7583E-06	1.3859e-06	6.29	6.75
192	4.4706E-03	4.4704e-03	6.8275E-07	4.5911e-07	6.52	6.63
256	4.4702E-03	4.4704e-03	1.9974E-07	4.5166e-07	5.99	5.27

10 on the finest grid. A projection from the convergence rate suggests that FSM needs a 173<sup>2</sup>-grid to match the FVM on 256<sup>2</sup>-grid. This saves half of the grid points.

So far, we see that PE4 is sufficient to deliver a sixth-order convergence rate. However, would it be enough to do it in a long integration time? This is a valid question since the cases we test so far are short time simulations. In the next section, we check this issue with the presence of wall boundaries.

#### 6.3. Instability of plane channel flow

The instability of a plane channel flow is a common test case used to validate the higher-order accuracy of numerical schemes including the wall treatment. In this test case, the parabolic velocity profile of the channel flow is disturbed by the most unstable eigenfunction  $\psi(y)$  and the respective stream function of the perturbations is  $\Psi(x, y) = \psi(y) exp[i(\alpha x - \omega t)]$ . The initial velocity field is given by

$$u(x, y, t) = (1 - y^{2}) + \varepsilon \frac{\partial \Psi(x, y)}{\partial y}$$
(54)

$$v(x, y, t) = -\varepsilon \frac{\partial \Psi(x, y)}{\partial x} \tag{55}$$

The energy of the perturbation and its growth-rate is computed by:

$$E_d(t) = \int_{\Omega} \left( u(x, y, t) - u(x, y, 0) \right)^2 + \left( v(x, y, t) - v(x, y, 0) \right)^2 dx dy$$
 (56)

$$G_d(t) = 2\omega_i = 2\ln\left(\frac{\partial E_d(t)}{\partial t}\right) \tag{57}$$

Note that only the real part of the perturbations is accepted into the velocities. This test-case is very sensitive to the balance among the terms in the NSE. The viscous term attenuates the perturbation while the convective term transfers energy from the main flow to the perturbations. If the approximation of the diffusion term is accurate and the convective term is under approximated, the growth-rate of the disturbance will be lower than the analytical value. This is a common situation found in finite difference methods applied to this case [63–67]. On the other hand, the growth-rate will be larger than the analytical one when the situation is reversed which is found in some finite volume codes [2] or Fourier B-spline method [68]. Higher-order convergence can only be achieved if every approximation is correctly treated. Therefore, this is a formidable test case for numerical schemes and the boundary closures.

The conditions of this test are set to the same conditions used in [64,68] with Re = 7500,  $\alpha = 1$ ,  $\varepsilon = 0.0001$  and the only unstable mode is  $\omega = 0.24989154 + 0.00223498i$  and the respective analytical growth rate is  $G_n(t) = 2\omega_i = 4.46996E$ -3. In this test case we use the eigenfunction obtained from a Chebyshev collocation with  $N_v = 512$ . The computational domain is set to  $[L_X, L_Y] = [2\pi H, 2H]$  based on the channel half-width H. The periodic conditions are set in the streamwise direction and the no-slip condition is imposed at the top and the bottom walls. The simulations are calculated using double precision and the growth-rate of the perturbation is measured at  $t = 50H/U_c$  where  $U_c$  is the velocity at the center of the channel. We conduct the test on uniform and non-uniform grids. On non-uniform grids, the grid is compressed at the wall and the smallest grid size is set to 1/Ny. The grid is stretched inwards the channel at a constant factor. All the simulations are solved with the explicit fourth-order pressure.

Note that another growth rate  $\omega_i$  can be found in literature which is 0.00223497 [69]. This difference stems from the solution process of the Orr-Sommerfeld equation. The eigenproblem solved by Chebyshev collocation [70] with different number of nodes deliver slightly different solution. The differences are bracketed by  $4 \times 10^{-8}$ , when the number of collocation points is varied from 480 to 1024. This translates to 0.001% relative error. We will explain later that this uncertainty can be one of the limiting factors when measuring the convergence rate of the method on very fine grids.

A. Hokpunna et al. / Journal of Computational Physics ••• (••••) •••••

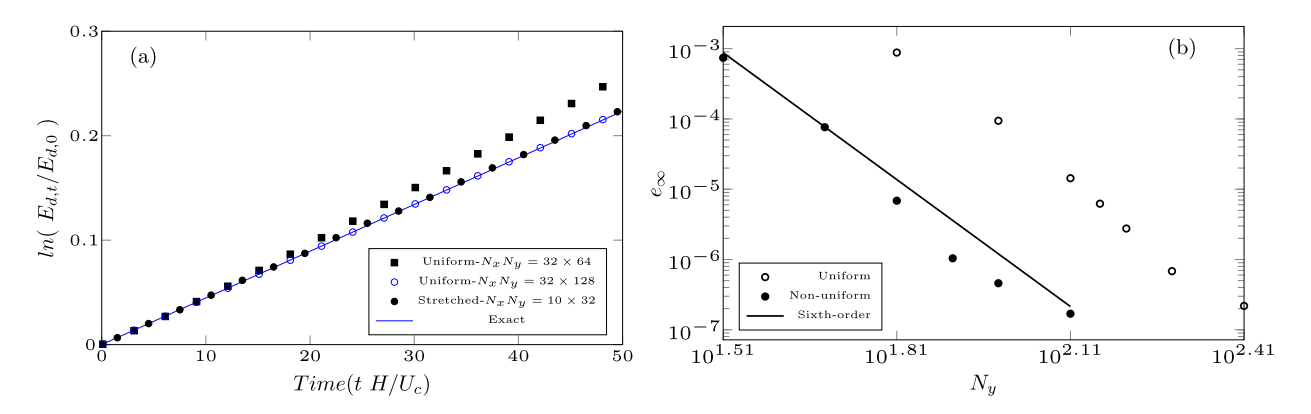


Fig. 14. (a) The growth of perturbations energy in plane channel flow. (b) Convergence rates on uniform- and non-uniform grids.

Fig. 14 shows the evolution of the perturbation energy beside the convergence rates on uniform- and non-uniform grids. It is evident that the proposed method delivers a clear sixth-order convergence rate on both type of grids. The geometric grid stretching allows the method to capture near-wall structures accurately and it delivers a comparable result to the uniform grid having twice resolutions. It is possible to optimize the grid distribution such as the one plotted in Fig. 14(a). There, the growth rate on a nonuniform grid  $(N_x N_y = 10 \times 32)$  is virtually identical to the analytical curve. The uniform grid needs 128 cells in y to get the same growth rate. In Table 4 we list the values of the growth rates, errors and convergence rates for a refinement in y-direction when  $N_x$  is fixed at 64. Two measurements of convergence rates are displayed, the averaged- and the final-growth rates.

We also perform another set of simulations using the compact fourth-order pressure (the results are not shown here). The differences are found in the eighth to tenth significant digits which can be rated as insignificant. Therefore, the sixth-order FSM can be used together with the fourth-order explicit pressure without a loss of accuracy in this test case. As we have seen earlier that LCO4 is comparable to LAG6, thus the prospect of using LAG6 to improve the solution is low.

It should be pointed out that, on the finest grid (Table 4), the convergence rate slows down to 5.27. This reduction can be explained by the approximate nature of the linear instability theory in which the perturbation consists of only a single mode. The Navier-Stokes equations are generating other modes as well due to their nonlinear nature and these nonlinear modes will affect the actual growth rate. We checked the energy of these additional modes at  $t = 2\pi/\omega_r$  and found that energy contained in these modes is 0.3%. In fact, the Fourier-Chebyshev spectral method [64] predicts  $G_d = 4.4714 \times 10^{-3}$  in average. The relative error of 0.001% mentioned earlier translates to the uncertainty in the last digit here.

Thus we can conclude that the Navier-Stokes equations simply converge to another growth rate than what linear stability theory predicted. The slight deviation on the finest grid is thus natural.

#### 6.4. Lid-driven cavity flow

Lid-driven cavity is one of the well-known benchmarks. We use the data published in [49] as a reference for our simulations. Here, we consider three Reynolds numbers: 1000, 5000, and 7500 of the cubical cavity  $(x, y) \in [0, L] \times [0, L]$ . Three simple uniform meshes with  $N = 50^2$ ,  $100^2$  and  $128^2$  are paired with the respective Reynolds number, in ascending order. The boundary conditions are set to  $u(x, L) = U_L$ , and the no-slip conditions are set everywhere else. This case contains two singularities at the top corner which require special treatment in some numerical methods. Here we do not use any type of stabilization, including filtering or dealiasing. We have seen from the previous cases that PE4 is sufficient, thus we use it in this test case. Note that the grid resolutions we use here are much coarser than those reported in the literature.

We first start with *RE*1000. All variables are set to zero initially and the flow is let to develop until it reaches the steady-state. Since we are not interested in the evolution and seek only the stable steady-state solution, we interpolate this solution to the other Reynolds number. Each case is then carried out until the steady-state solution is reached (change in the kinetic energy is less than  $10^{-10}$  per  $L/U_L$ . The final vertical profiles of the horizontal velocity are displayed in Fig. 15 including the primary core vorticity from the reference and the one from [71]. The FSM profiles of the two lower *Re* agree very well with the reference. FSM solution still agrees reasonably with the reference at the highest *Re*, but the deviations become larger. The magnitude of the primary core vorticity ( $|\omega_c|$ ) of the lowest *Re* is within 0.3% of the reference values (2.0721 vs. 2.0677). In comparison, Boersma [18] applies a compact sixth-order FDM to this flow and obtains the vorticity  $|\omega_c| = 2.02622$ , 2.05889, and 2.0666 on 32°, 64°, and 128° grids. Bruneau and Saad [71] report that three third-order upwind schemes deliver  $|\omega_c| = 2.0538$  and 2.0638 in averaged on 128° and 256° grids, respectively. Nishida et al. [48] apply a sixth-order scheme on a 129°-grid and obtain 2.05715. We refer the reader to [49] for an extensive comparison among different methods.

The magnitude of the primary core vorticity on RE7500 still follows the reference closely, but the deviation in the core vorticity is increased to 1.8%. It should be pointed out that the RE7500 is a formidable test case. In the reference, Erturk et al. employ 3 grids for this case and they found that the vorticity on the lowest resolution ( $N = 401^2$ ) differs from the

Fig. 15. Horizontal velocity at the center-plane (x = L/2) and the vorticity at the primary core ( $\omega_c$ ). The velocity in Re = 5,000 and 7,500 are shifted 0.5 $U_L$  and  $U_L$ , respectively. The reference solution ECG is from [49] and BS is from [71].

reference value by 2.5%. Doubling the total number of grid points, only reduces this error to 1.1%. Thus, it is satisfactory that the FSM can deliver similar predictions using a much coarser grid.

#### 7. Applicable range of *n*-th apparent convergence rate with lower-order pressure treatment

In the previous sections, we have seen the performance of the explicit fourth-order pressure treatment (PE4). Evidently, the pressure treatment PE4 can support the sixth-order accuracy of the FSM. Based on the formal truncation error, however, we cannot expect PE4 to deliver the sixth-order convergence rate in every situation. If the flow spectrum is broad, the error in the small scales from the convective term could be dominant dwarfing all other errors. On the other hand, if the flow lacks high frequency parts, the fourth-order error of the pressure would be exposed as we have seen in the benchmarks applied so far. The next natural question is "In what situation PE4 can accommodate the sixth-order FSM?". This section is dedicated to answer this question.

In actual turbulent flows, the spectrum is broad. The dominant error of a numerical simulation is determined by the combination of the transfer function of the overall numerical schemes and the complexity of the flow. In a homogeneous turbulent flow, Kolmogorov's theory predicted the -7/3 law for the pressure spectra and the -5/3 law for the velocity spectra. In different regimes of turbulent flows, the pressure and velocity spectra can have different slopes. In boundary layer flows, the slopes of the pressure spectra  $E_{pp}$  are found between -1 and -7/3 while the slopes of velocity spectra are close to -5/3 [72]. In this section, we use a synthesis spectrum to check for the range of the decay rate in which we can use a lower-order pressure treatment to support the sixth- and eighth-order NSE solver. We neglect the damping function of the spectrum and consider a one-dimensional analysis by assuming that u and p follow the following the same spectrum:

$$E(kh) = (kh)^{-a}. (58)$$

Let us recall the semi-discrete form of the momentum equation in Eq. (7), rewrite it in a vector form and apply a discrete Fourier transform ( $\mathfrak{F}$ ) to it, and strip the subscripts and superscripts for clarity:

$$\mathbf{A} \cdot \mathfrak{F} \frac{\partial \mathbf{u}}{\partial t} = -\mathfrak{F} \mathcal{C} + \nu \mathfrak{F} \mathcal{D} - \frac{1}{\rho} \mathfrak{F} \mathcal{P}. \tag{59}$$

The numerical approximations alter the above equation to

$$\mathbf{A} \cdot \mathfrak{F} \frac{\partial \widetilde{\mathbf{u}}}{\partial t} = -\mathfrak{F} \widetilde{\mathcal{C}} + \nu \mathfrak{F} \widetilde{\mathcal{D}} - \frac{1}{\rho} \mathfrak{F} \widetilde{\mathcal{P}}. \tag{60}$$

The difference between the RHS Eq. (59) and Eq. (60) is the error that will affect the evolution of the velocity. The diffusion term is usually very accurate and thus we neglect it along with the density. The error in the evolution equation becomes

$$\mathbf{E}_{\widehat{u}} = -\left(\mathfrak{F}\mathcal{C} - \mathfrak{F}\widetilde{\mathcal{C}}\right) - \left(\mathfrak{F}\mathcal{P} - \mathfrak{F}\widetilde{\mathcal{P}}\right) \tag{61}$$

Let  $\mathbf{EC}_{\widehat{u}}$  and  $\mathbf{EP}_{\widehat{u},p}$  be the error from the convection and the pressure. The error from the convection can be further decomposed in to each direction. Let us consider the error norm due to the convection in x-direction:

A. Hokpunna et al. / Journal of Computational Physics ••• (••••) •••••

$$\left| EC_{\widehat{u},x}(\kappa) \right| = \left| \mathfrak{F} \left( \mathcal{C}_{x} - \widetilde{\mathcal{C}}_{x} \right) \right| = \left| \mathfrak{F} \left( \left[ \frac{\partial uu}{\partial x} \right]^{yz} - \left[ \frac{\partial uu}{\partial x} \right]^{yz} \right) \right|$$
(62)

A simple Fourier analysis can show that an error in the nonlinear convection is larger than the linear one, therefore

$$\left| \mathfrak{F} \left( \left[ \frac{\partial u}{\partial x} \right]^{yz} - \widetilde{\left[ \frac{\partial u}{\partial x} \right]^{yz}} \right) \right| \le \left| EC_{\widehat{u},x} \left( \kappa \right) \right| = \left| \mathfrak{F} \left( \left[ \frac{\partial uu}{\partial x} \right]^{yz} - \widetilde{\left[ \frac{\partial uu}{\partial x} \right]^{yz}} \right) \right|. \tag{63}$$

Note that the indices are dropped for clarity.

Thus, the normalized cumulative error in the convection of  $u_i$  due to the deficiency in the transfer function is bounded on the left by

$$\Psi_{u}(\pi) = \frac{1}{|\widehat{u}_{\kappa}|_{2}} \int_{0}^{\pi} |1 - T_{C}(\kappa)| \, \widehat{u}_{\kappa} \, d\kappa, \tag{64}$$

where  $T_C$  is the transfer function of the linear convection in Eq. (16). This is the total error in the resolvable Fourier space. Likewise, the cumulative normalized error in the pressure gradient reads

$$\Psi_p(\pi) = \frac{1}{|\widehat{p}_{\kappa}|_2} \int_0^{\pi} |1 - T_G(\kappa)| \ \widehat{p}_{\kappa} \ d\kappa, \tag{65}$$

where  $T_G$  is the inter-cell differentiation for the pressure gradient such as Eq. (29) and Eq. (30). Note that we neglect the superposition and the cancellation of the other two convection directions. Only the contribution from the x-direction is kept in  $\Psi_{u}(\pi)$ .

Next, let us assume that the spectrum of the pressure and the velocity are the same, that is  $\widehat{u}_{\kappa} = \widehat{p}_{\kappa}$ . Then, we pair the convection schemes with a different pressure scheme and plot the ratio of the normalized error  $|\Psi_p(\pi)/\Psi_u(\pi)|$  against the decaying rate of the spectrum (a) in Fig. 16. The ratio larger than one means the pressure error is larger than the convection error, and vice versa. For the flat spectrum  $(a \to 0)$ , the field is very rough and the lower-order pressure gradient ((n-2)-th) is superior to the higher-order convection (n-th) as expected. As a increases, the flows become smoother and the error of the lower-order gradients grows faster due to the larger LTE. For decay rates larger than a = 2.71, the ratio is larger than one. This rate is already outside the range found in turbulent boundary layer. For such a rapidly decaying spectrum, the flow should appear very well resolved on the grid. The compact version of the fourth-order pressure (G4C) is more accurate than the sixth-order approximation of the momentum (D6C) for all decay rates considered here. This trend is carried on to the eight-order FSM as well. Both sixth-order approximations of the pressure are more accurate than the eighth-order convection approximation, throughout the range (a < 5). Furthermore, the compact fourth-order scheme (G4C) would be able to support the eighth-order convection (D8C) up to a = 4.36. It is very likely that the fourth-order compact pressure can support the eighth-order scheme very well. Thus, the high resolving power of the compact scheme is extremely useful. This should be applicable to other methods on staggered grid as well. However, at a lower applicable range, It is worth noting that, P2CC can deliver around third-order convergence rate when paired with the compact fourth-order FVM [44]. In another study, we found that the P4CC can deliver a fifth-order convergence rate when paired with the compact sixth-order FVM.

We revisit the double shear layer problem ( $N = 512^2$  and t = 1.2) and plot pressure and velocity profiles on the horizontal center line including their spectra in Fig. 17. The flow is very smooth and is over resolved by the grid as we can see that the energy of the modes  $kh > 2\pi/3$  drops to machine accuracy. The modes  $kh > \pi/2$  are already very small. The decay rate in  $\pi/3 > kh > 2\pi/3$  is roughly 10 which is larger than the predicted break-even point. The magnitude of the error on this grid can be extrapolated from the error on  $N = 256^2$  in Fig. 13 to be 4E-7. The solutions of PE4 and PE6 on this grid differ from PCO6 by 3.2E-7 and 2.8E-10, respectively. Thus, even for such a steep decay spectra, PE4 is still accurate enough to accommodate the sixth-order FSM down to 512<sup>2</sup>-grid which is already overresolved.

It should be noted that, our prediction for the break-even point here is very conservative and thus it cannot be used to predict the precise point. The main message, however is, the explicit fourth-order pressure can be used with the compact sixth-order FSM in practical fluid flows. The less resolved the flow is, the smaller is the contribution of the pressure error to the overall error.

#### 8. Application to turbulent channel flow

In this section we investigate the accuracy and the performance of the newly developed scheme in turbulent channel flow. This type of flow has been used extensively for turbulence research and modeling as well as benchmarking numerical schemes. Results of numerical simulations using spectral codes from several authors [73-77] are publicly available for comparison. Numerical simulations using other classes of approximations should converge to these data. The previous results suggest that the benefits of PCO4 and PE6 over PE4 will only show at an extremely well resolved flow. In the following

a

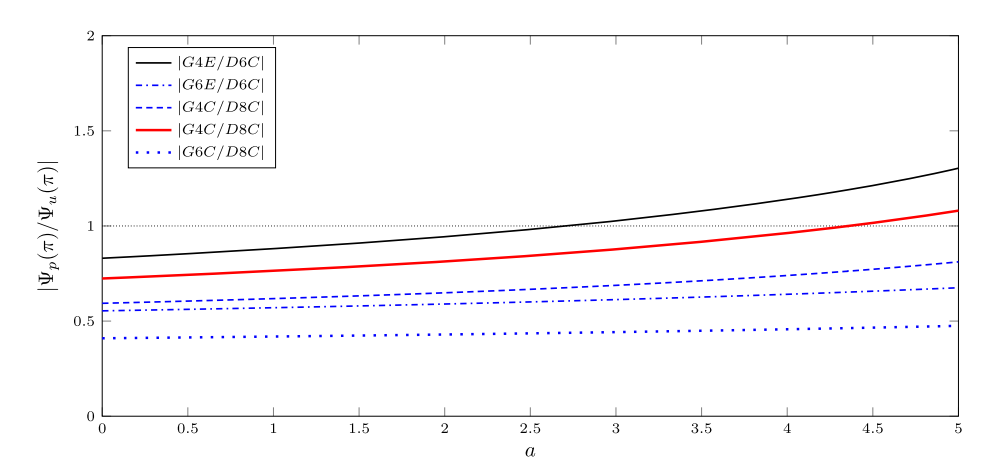


**Fig. 16.** Comparison of total errors of from the pressure gradient and the differentiation in the convective term. The less accurate pressure gradients (4 and 6) are compared with a more accurate differentiation (6 and 8). The G stands for inter-cell deconvoluted differentiation for the pressure gradient and D stands for collocated differentiation for the convection term. E and C is for the explicit and the compact schemes. The break-even points of G4E/D6C and G4C/D8C are g=2.71 and g=4.71 and

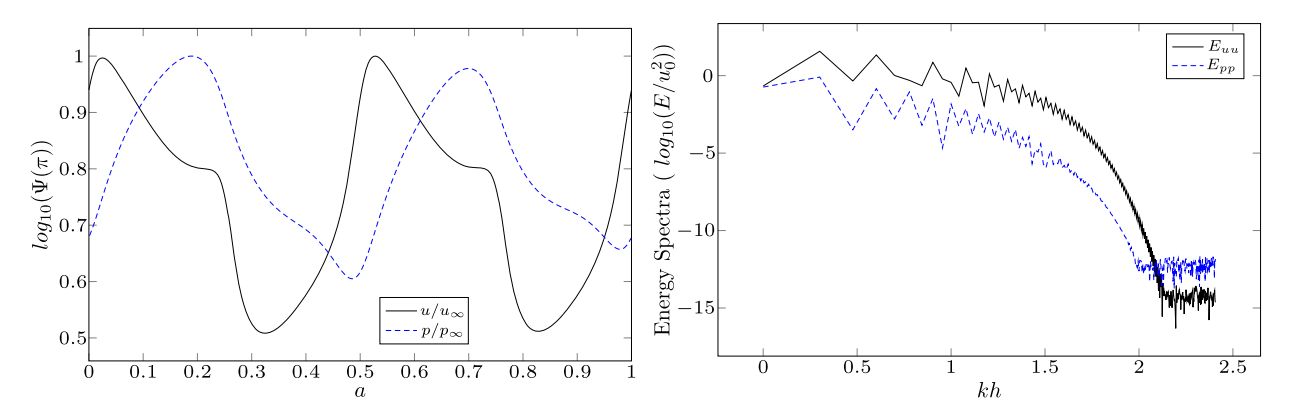


**Fig. 17.** The energy spectra of u and p in the double shear layer flow at t = 1.2 with  $N = 512^2$ . The spectra show that the flow is over resolved and the spectra of u are more complex than the pressure's.

simulations, we use only the fourth-order explicit pressure (PE4) and keep all the other terms at sixth-order, except the nonlinear correction which is removed. We filter the transported velocity to a temporary array before performing the convection. The original velocity is kept unfiltered and the final  $du_i$  is added to  $u_i$  during the time integration without filtering. The projection method is then applied and the process repeated again for the next time step. The filtering is thus applied directly and only to the convective term. We do not consider this dealiasing to be turbulence modeling because the viscous diffusion is not altered in any way. This is unlike the high-wave artificial viscosity, or filtering the velocity field, which can be rewritten in a diffusion form. The filtering process we used, acts in the same way as the dealiasing in spectral codes.

The dealiasing is applied in both homogeneous directions. The wall-normal direction is sufficiently well resolved and does not need filtering. Effectively, the leading complexity of the convective term and the pressure gradient becomes 115N per momentum per time step. The cost of the filtering is very demanding. It now costs 42% of the convective term. The result is compared against the spectral database and the compact fourth-order FVM of [2]. Note that we turn off the NC in the FVM as well and the respective complexity is 95N. When adding the diffusion term, the sixth-order FSM costs 17% more operations than the fourth-order FVM.

In the first part of this section, we investigate  $Re_{\tau} = 180$  and establish the relationship between the error in the bulk flow velocity and the normalized grid spacing. The grid resolution requirement found in this section is then used to design two new grids for the two additional Reynolds numbers,  $Re_{\tau} = 590$  and 950.

#### 8.1. Friction Reynolds number 180

Sagaut [78] suggests that, for the turbulent channel flow, the grid resolution in the streamwise, spanwise and the wall-normal directions should be  $[\triangle x, \triangle y_{wall}, \triangle y_{max}, \triangle z] = [15^+, 1^+, 10^+, 5^+]$  which are corresponding to the physical size of the smallest relevant scales. The flow is usually driven by a pressure gradient added as a source term in the streamwise velocity. The driving force could be determined a priori using Dean's correlation between the Reynolds number based on

A. Hokpunna et al. / Journal of Computational Physics ••• (•••) •••••

**Table 5**Grid parameters and mean flow variables of the standard grids used in this validation compared to the references. The domain sizes are normalized by the channel half-width *H*. Grid sizes are in wall-unit. The first 8 rows are the simulations using FSM presented in this paper.

Simulation	Domai	n	Reynolds	number	Grid spa	cing			Velocity r	atio
	$L_x$	Lz	Reb	$Re_{\tau}$	$\triangle x^+$	$\triangle z^+$	$\triangle y_{wall}^+$	$\triangle y_{max}^+$	$u_c/u_\tau$	$u_b/u_\tau$
32 <sup>3</sup>			5,127	177.53	69.7	23.2	5.4	18.4	16.87	14.94
48 <sup>3</sup>			5,323	177.90	46.6	15.5	3.0	13.6	16.87	14.96
56 <sup>3</sup>			5,402	180.05	40.4	13.5	2.5	11.9	17.39	15.00
64 <sup>3</sup>	$4\pi$	$4\pi/3$	5,472	178.24	35.0	11.7	2.2	10.5	17.86	15.39
$70^{3}$	411	411/3	5,529	178.01	31.9	10.6	1.8	10.3	17.94	15.53
$80^{3}$			5,562	179.24	28.0	9.3	1.6	9.1	18.12	15.52
100 <sup>3</sup>			5,624	178.05	22.4	7.5	1.2	7.5	18.36	15.75
128 <sup>3</sup>			5,605	178.25	17.5	5.8	0.89	5.2	18.30	15.69
144 <sup>3</sup>			5,606	178.50	15.6	5.2	0.40	5.2	18.27	15.73
KMM1987 [73]	$4\pi$	$2\pi$	5, 600	180.00	11.8	7.1	0.054	4.4	18.20	15.63
MKM1999 [74]	$4\pi$	$4\pi/3$	5, 529	178.13	17.7	5.9	0.054	4.4	18.30	15.52
VK2014 [76]	$4\pi$	$4\pi/3$	5, 616	180.00	5.9	2.9	0.024	3.9	18.28	15.60

the friction  $(Re_{\tau})$  and the bulk flow  $(Re_b)$  velocities:  $Re_{\tau}=0.09Re_b^{0.88}$ . This force can be fixed or controlled. Fixing the pressure gradient will fix  $u_{\tau}$  and  $Re_{\tau}$  up to sampling error. The numerical interactions will determine the bulk flow. For example, when the numerical scheme predicts low turbulent interactions and diffusion, the bulk flow would be higher than the correct value, and vice versa. On the other hand, adjusting the pressure gradient to fix the bulk flow or  $(Re_b)$  will result in an error of the friction factor. In this work we fix the pressure gradient and let the bulk flow adjusts itself according to the numerical interactions.

The parameters of the numerical grids and the computational domain used in this study are listed in Table 5 along with the three spectral simulations which are used for comparison. In our simulations, the streamwise, spanwise and wall-normal directions are set to x, y and z accordingly. The computational box is  $[L_x, L_y, L_z] = [4\pi H, 4/3\pi H, 2H]$  which is the same domain used in [74,76].

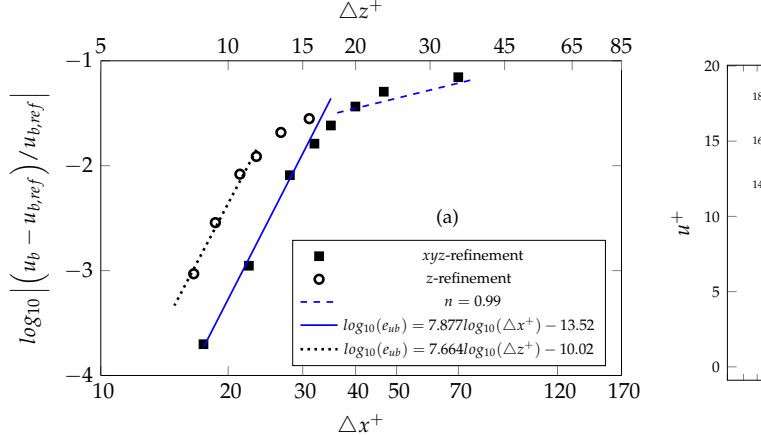
Homogeneity is assumed in streamwise and spanwise directions and thus periodic boundary conditions are applied. The top and the bottom walls are treated by no-slip boundary conditions. The flow is driven by a constant pressure gradient which is added as a source term in the momentum equation of the streamwise velocity. There is no control of mass flow within the simulations. The initial velocity field is obtained by imposing a random perturbation on the logarithmic velocity profile with a Tollman-Schlichting wave. We integrate the solution in time using  $CFL \approx 0.2$  for 32 < N < 64 to mimic actual conditions that the DNS code would be mostly used. After that resolution, we are forced to reduce the CFL number to  $\approx 0.05$  in order to keep the time-integration error low. The statistically steady state is assumed when the bulk flow velocity is not changed more than  $0.5\%U_b$  over a period of  $10L_x/U_b$ . After the statistically steady state is reached, the flow was further advanced for  $10L_x/U_b$  before the sampling started. The sampling time is set to  $500H/U_b$  together with the averaging in the homogeneous directions. In order to find a correlation between the normalized grid spacing and the accuracy of the simulation we perform a convergence study using numerical grids listed in Table 5, starting from a very coarse grid up to the one slightly finer than the spectral solution in [74].

#### 8.1.1. Mean flow statistics

Turbulent channel flows have been studied extensively and the shape of the mean profile in the viscous sublayer and the outer layer are well understood. Dean's correlations for the channel flow are very accurate and they agree well with many respectable direct numerical simulations. In Table 5, we list two mean velocities ratios: the center line and bulk velocities per friction velocity,  $u_c/u_\tau$  and  $u_b/u_\tau$ . It is clear that the FSM converges to the spectral solution as the grid resolution increases. The ratio  $u_b/u_c$  on the coarse grid is 1.146 and it is increased to 1.165 on 64³-grid which is within the 0.1% of the final value (1.164) on 128³-grid. This final value is exactly same as KMM1987 [73]. Thus, FSM should already produce a correct shape of the mean velocity starting from  $N = 64^3$  grid. According to the table, mean flow parameters are monotonically approaching the reference value until  $100^3$ -grid. However, for the finer grids, the parameters oscillate near the reference value. These small deviations ( $\approx 0.2\%$ ) can be attributed to the statistical uncertainty (discussed later).

In transient simulations of turbulent flow, it is very important to use a good numerical grid. This means the relevant structures of the flow must be properly resolved. This is usually translated to using grid sizes in the range of Kolmogorov's or Taylor's length-scales. In DNS, it is very costly to follow this strict interpretation. In some cases, numerical simulations are performed on grids coarser than the theoretical resolution. Such numerical simulations are usually called coarse DNS, when no explicit or implicit modelings are involved. It is very useful to know the grid resolutions needed to achieve the desired accuracy.

Thus, we investigate the convergence rate of the mean bulk flow in Fig. 18(a), where the error of the bulk flow velocity is plotted against normalized grid spacings. The overview of the velocity profile on some grids is shown beside in Fig. 18(b). Two convergence studies are conducted, the simultaneous refinement on all directions (xyz-refinement) and the spanwise refinement (z-refinement). In the xyz-refinement, we plot  $\triangle x^+$  against the  $u_b$ -error w.r.t. the result on the  $144^3$ -grid.



JID:YJCPH AID:109790 /FLA

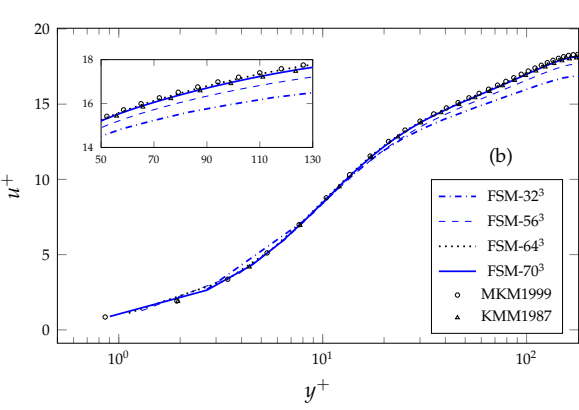


**Fig. 18.** The convergence of the bulk flow velocity against the three-dimensional refinement (xyz-refinement) and the refinement in the spanwise direction (z-refinement) w.r.t. 144<sup>3</sup>-grid and the error estimations for the convergent regime (a). Mean velocity profiles compared to two spectral solutions from [73] and [74] (b).

The error curve exhibits two convergence rates, the underresolved and the resolved rates. In the underresolved region, the convergence rate is approximately one. Starting from  $\triangle x^+ = 40$  ( $N = 56^3$ ), the flow is sufficiently resolved and a convergence rate of order 7.88 is obtained.

Next, we fix the number of grid in the streamwise and wall-normal directions ( $N_x = N_y = 100$ ) and check the convergence rate in the spanwise direction (z-refinement). The mean velocity error is plotted against the spanwise grid spacing using the secondary axis on the top ( $\Delta z^+$ ). The convergence curve exhibits two regions similar to the simultaneous refinement. In the resolved region, a convergence rate of 7.66 is obtained. The errors of the bulk flow rate on  $64^3$  and  $100^3$  grids are 2.4% and 0.1%, respectively. The relative error in  $u_b/u_\tau$  here is intended as a quick performance indicator which can be easily generated and compared to other methods. The low error in  $u_b/u_\tau$  does not necessarily mean that the profile is accurate to the same error level. In order to quantify the error in the profile, we compute the deviation of these two profiles from the reference [74]. The maximum deviations on these two grids are 2.5% and 0.5% which is comparable to the previous numbers. Thus, the error in  $u_b/u_\tau$  is a reasonable indicator for the error in the mean velocity profile. Vreman and Kuerten [76] analyzed several turbulent channel flow databases and found that the differences in the mean profiles from spectral simulations can be up to 0.4% which is just slightly lower than the error level on our  $100^3$ -grid. They also analyze the maximum statistical relative error when sampling the flow over  $T = 200H/u_\tau$  (equals to 3,  $216H/u_b$  in our outer time unit). The maximum values in their mean velocity profiles are in the range of 0.1 - 0.8%. Thus, it can be concluded that, the sampling error is the dominant part beyond  $100^3$  grid.

In order to determine the relationship between the error and the grid spacings, we fitted estimations for the relative errors in the mean bulk flow. The equations for the convergence regimes are shown in the graph. However, an estimation with a wider range is

$$\log_{10}\left(\frac{er_{ub}}{u_b}\right) = -9.342X_{l10p}^2 + 33.05X_{l10p} - 30.41,\tag{66}$$

with  $X_{l10p} = log_{10}(\triangle x^+)$ . This relation is valid on  $10^{-4} < er_{ub} < 10^{-1}$ . Therefore the streamwise grid spacings  $(\triangle x^+)$  needed to achieve 3%, 1%, and 0.1% error are 38, 30 and 21, respectively. Likewise, the respective spanwise grid spacings are  $\triangle z^+ = 16$ , 11 and 8.3. If the structures in turbulent channel flow scale similarly, these estimations should hold for other Reynolds numbers too. It is also worth noting that, the ratio  $\triangle x/\triangle y$  is about 2.5, which is slightly smaller than the ratio recommended (3) in [78]. Thus, from this study we can conclude that for the homogeneous directions, FSM can achieve 3% errors in the mean profile using a grid 2.5-times larger than the recommended resolutions. A 1%-error can be achieved with a factor two. For a one-per-mille error, FSM can achieve with factor 1.4. The necessary resolution in the wall-normal direction will be presented later.

Fig. 18(b) displays the mean streamwise velocity profiles along with the two reference data from [73,74]. The result from the 32<sup>3</sup> grid captures the flow relatively well, considered that wall-normal cell at the wall is  $5.3y^+$  which is a bit larger than the viscous sublayer. Doubling the resolution in every direction pushes the profile within the two spectral solutions. Increasing the number of grid points further to  $70^3$  does not change the mean profile in a significant way. Thus, the profile must have already converged as the  $u_b/u_\tau$ -ratio suggested earlier. When compared to a compact fourth-order FVM [2], a similar equation for Eq. (66) can be formed. The ratio of the necessary grid size between FVM and FSM ( $\triangle x_{FVM}^+/\triangle x_{FSM}^+$ ) is approximately 1.25, for the error levels considered here.



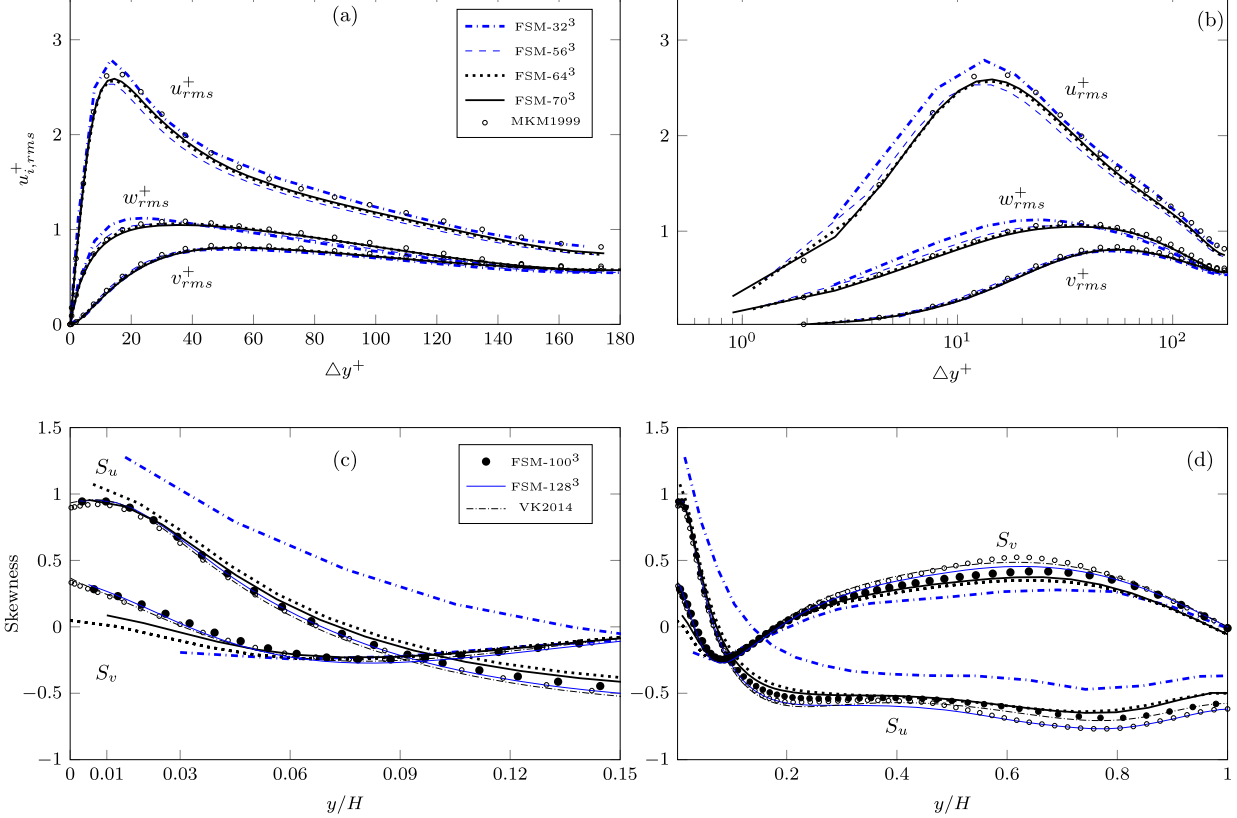
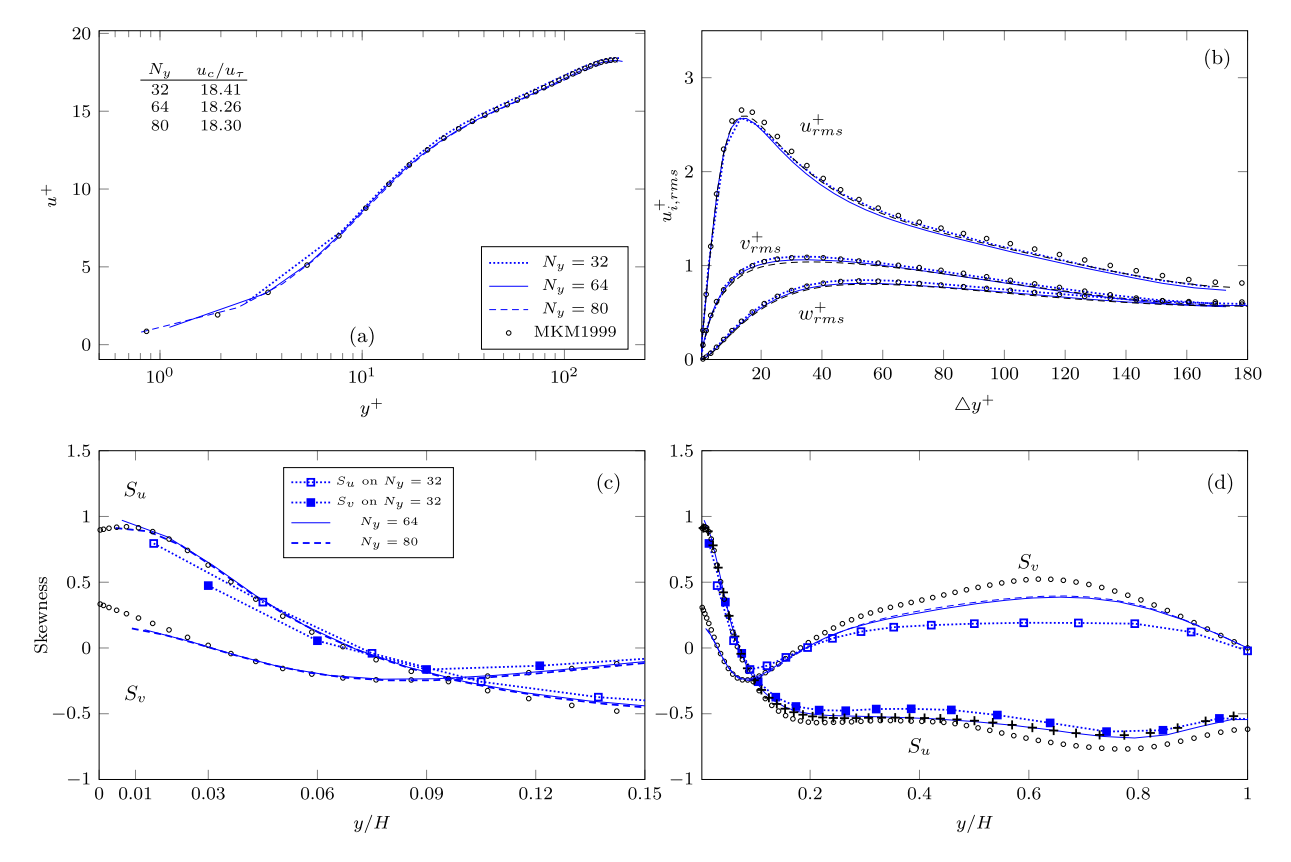


Fig. 19. RMS of the velocity fluctuations in linear (a) and in logarithmic scales (b). Skewness of the streamwise and wall-normal components near the wall (c) and in the first half of the channel (d). Legends are listed in (a) and (c). The line styles are consistent for all graphs. For clarity, the skewness from 563-grid and the RMS from 1003- and 1283-grids are not plotted.

#### 8.1.2. Second- and third-order statistics

The second- and third-order statistics are plotted in Fig. 19(a). The values plotted here are the statistics of the faceaveraged fluctuations and the horizontal axis positions are the face center. They are not expected to be the same value as the pointwise data from the reference solution, but they should be close. The differences are in the order of  $O(\triangle v^2)$  and the differences should be contracting as the grid is refined. At the coarsest resolution, the peak  $u_{rms}$  overshoots to 2.79 which is 5% higher than the reference solutions. For finer grids, the RMS profiles of FSM approach the spectral solution from below. This means the flow is heavily underresolved on the 32<sup>3</sup>-grid. A good agreement of an RMS with the reference on this grid at the channel center is purely coincidental. The RMS from  $64^3$  and  $70^3$  grids are very similar and they are closer to the reference than the one of the  $56^3$ -grid. The *u*-rms on  $70^3$ -grid peaks at 2.588 which is 2.6% lower than MKM1999 (2.66) indicating a convergence in the second-order statistics. Still, to put the RMS curves within 1% error of the spectral solutions, FSM needs 128<sup>3</sup>. We do not show this profile on the graph to stress the accuracy of the RMS on 64<sup>3</sup> and 70<sup>3</sup> grids. On the  $128^3$ -grid, the peak of  $u_{rms}$  is 2.658, while the peak cell-averaged from MKM1999 is 2.65. The peak  $u_{rms}$  from VK2014 is 2.67 and the one from MKM1987 is 2.63. The overall relative error (except the first cell) w.r.t. MKM1999 is 3.3% which is on the same level as the differences among the spectral codes [76]. The  $u_{rms}$  on the first cell, however, differs from the reference by 13%. This could be probably contributed to the difference in the type of the data statistics: the face-averaged against the pointwise data. That is  $\langle [u]'[u]' \rangle \neq \langle u'u' \rangle \neq [\langle u'u' \rangle]$ , especially at the first cell where the gradient is

Next, we consider the skewness of the velocities fluctuations. The skewness measures the asymmetry of the probability density function (PDF). Positive values mean that the tail of the PDF is on the right and the positive fluctuations are stronger in magnitude, but less frequent. Here we consider the skewness of u and v in Fig. 19(b). The value of  $S_w$  is close to zero because of the flow symmetry and thus not considered here. The coarsest grid predicts  $S_u$  much higher than the correct level and the profile seems to be shifted at a constant factor upward. The profile of  $S_v$  agrees well with the other grid in the center. However, it predicts a negative value near the wall which is opposite to the reality. Increasing the resolution, improves the accuracy of the solutions. Near the wall, the result from [74] indicates that  $S_u$  starts from 0.897 and reaches the peak value 0.922 at 0.00752H (1.34 $y^+$ ). On our 64 $^3$ -grid, the first cell size is 2.2 $y^+$ . This grid over predicts  $S_u$  slightly (1.07). This overshoot disappears when the size of the first cell is refined to  $1.8y^+$  on the  $70^3$ -grid. In order to have an excellent agreement on  $S_v$  near the wall, the size of the first-cell must be comparable to this peak's distance which is



**Fig. 20.** Profiles of flow statistics under wall-normal refinement: (a) mean streamwise velocity, (b) RMS of velocity fluctuations, (c) skewness near the wall, and (d) skewness over half of the channel. Legends are listed in (a) and (c). The line styles are consistent for all graphs. The skewness of u is marked by open square for  $N_V = 32$  to help distinguish it from  $S_V$  which is marked by filled rectangles.

achieved on the  $100^3$ -grid (two cells enclosing the peak). As moving away from the wall, the skewness of FSM's solutions deviates slightly from the reference solution, however, it is clear that the grid refinement brings the profiles closer to those from the references. The skewness profiles from the  $128^3$ -grid are very close to the other two spectral solutions and the differences among the three profiles are comparable. For example, near y/H = 0.6, MKM1999 overpredicts the peak  $S_v$  from VK2014 by a comparable level that FSM-128<sup>3</sup> underpredicts it (7% vs. 8%).

#### 8.1.3. Wall-normal grid resolution effects

In comparison to other higher-order methods applied to turbulent channel flow, our result on  $64^3$  (DOF = 0.26M) is more accurate than the implicit LES from discontinuous Galerkin method [79] on 1M DOF and it is comparable to the result with 8.4M DOF. FSM on this grid predicts the same value of the peak  $u_{rms}$  as the optimized sixth-order compact [80] with 1.39M grid. Traditionally for DNS, it is recommended to have the first cell at one wall-unit. This guideline is applicable to wall-resolved LES as well and the standard resolutions used in the wall-bounded flow are usually set to  $\Delta x^+ \approx 50 \sim 130$  and  $\Delta z^+ \approx 15 \sim 30$ . The lower values of these ranges are very close to the 3%-resolution established earlier ( $\Delta x^+ = 40$  and  $\Delta z^+ = 14$ ). Rezaeiravesh and Liefvendahl [81] recently investigated the effect of grid resolution on LES of turbulent channel flow using OpenFOAM and they recommend that  $\Delta x^+ < 18$ ,  $\Delta z^+ < 12$  and  $\Delta y^+_{wall} < 2$  are sufficient to produce low errors in the flow statistics. Since our grid resolution requirement in the homogeneous directions is much more relaxed, it is interesting to see the new resolution requirement in the wall-normal direction.

Physically, the wall-normal grid size is responsible for two important effects. First it must capture small-scaled interactions near the wall, especially the impingement of high momentum fluid from the outer layer and the formation of streamwise and spanwise vortices. Second, it must be able to capture the correct shear force of the streamwise velocity profile which is very steep near the wall. A grid too coarse will destabilize the numerical boundary closures leading to a simulation failure. In order to shed some light on this issue, we take the  $100^3$ -grid and perform a coarsening in the wall-normal direction by reducing the number of cells to 64 and 32. The wall-normal grid distributions are taken directly from the previous cases ( $64^3$  and  $32^3$  in Table 5). The mean and the RMS profiles are plotted in Fig. 20. Unlike our expectation, the results imply that the wall-normal grid size almost does not affect the mean and the RMS profiles, as long as the simulation is stable. The differences however appear in the skewness where we get an unusually high value of  $S_v$  near the wall. The curve on  $N_z = 32$  follows  $S_u$  instead of the correct curve. The high positive value here indicates that ejection events

A. Hokpunna et al. / Journal of Computational Physics ••• (••••) •••••

Table 6 Sequential CPU-time per time-step on Intel Xeon 8168 and three performance indices of FSM: i. Million grid points per second (MPS), ii. MPS per TeraFLOPS of LINPACK 1000D (MPTF<sub>1000D</sub>) and iii. MPS per TeraFLOPS of HPL. The FSM, FVM and the two benchmarks are compiled using Intel compiler with -O3 -xCORF-AVX512

Method	CPU-time	per time st	ep (s)	FSM per	formance index	
	FVM4	FSM6	FSM6/FVM4	MPS	$MPTF_{1000D}$	$MPTF_{HPL}$
32 <sup>3</sup>	0.018	0.017	0.975	1.88	293.7	20.6
$48^{3}$	0.068	0.064	0.976	1.74	272.0	19.1
$56^{3}$	0.128	0.123	0.963	1.37	214.9	15.0
$64^{3}$	0.189	0.187	0.992	1.39	214.4	15.2
$70^{3}$	0.363	0.360	0.986	1.25	195.6	13.7
$80^{3}$	0.395	0.398	1.007	1.23	193.0	13.5
$128^{3}$	2.065	2.029	0.983	0.93	148.8	10.2
144 <sup>3</sup>	3.154	3.202	1.018	0.95	145.7	10.0

become much stronger near the wall. Later at  $y \approx 0.1H \approx 18y^+$ ,  $S_v$  resumes the usual value. This means  $\triangle y_{wall} = 5.3y^+$ is not enough to resolve the near-wall dynamics correctly, but it still can provide an equivalent momentum transfer for the early buffer layer and the outer layer.

We also tried pairing a very fine wall resolution and with a coarser grid in the homogeneous directions and found that the resolutions in the homogeneous directions dictate the bulk flow rate. Specifically, all the wall-normal resolution we used here, when paired with  $N^2$ -grid in the wall-parallel directions, would generate essentially the same mean flow as the corresponding  $N^3$ -grid reported in Table 5. Unfortunately, when the first grid cell is larger than  $6y^+$ , the simulations become unstable. Thus, for an accurate prediction of the first- and second-order statistics, the first grid cell should not go beyond the viscous sublayer  $(\triangle y_{wall} \le 5y^+)$  and we recommend  $4y^+$  as the maximum size. It should be mentioned that this near-constant flow rate behavior is observed on the fourth-order FVM as well, but the wall-normal grid size must be 25% finer than in FSM to achieve the same effects. Coupled with the resolving power improvement in the wall-parallel direction, FSM only needs half of the grid points  $(N_t/2)$  to match the compact fourth-order FVM on  $N_t$ -grid.

According to the result with  $N_V = 32$ , grid spacing at the center in this case should be sufficient to resolve the flow there. This is highly possible because the flow in the center is almost isotropic. Thus, the size of  $\triangle x^+$  should be applicable in the wall-normal direction as well. This preliminary resolution ( $\Delta y^+ = 30$ ) will be tested using the other two Reynolds numbers later.

#### 8.1.4. CPU-time

In two-dimensional laminar flows, FSM does not require the filter and the momentum calculation is 30-60% faster than the fourth-order FVM. However, when we use the filter on convective terms, the finite surface slows down significantly. We measured the computational time in the previous turbulent channel flow simulations. Note that, we use a direct solver with FFT in the homogeneous directions to solve the Poisson equation. The third-order RK time-integration of the FSM takes 0.18 s on the coarsest grid and 3.15 s on the finest (Table 5). The detail on CPU-time is listed in Table 6. On average, FSM with filter is slightly faster than the fourth-order FVM on the same grid. This falls within the expectation, because FVM needs more memory transfer which offsets the lower number of floating point operations. The CPU-time of both methods is increasing as a logarithmic function of the number of grid points due the Nlog(N) complexity of the FFT. This eventually becomes the leading cost as N increases. Taking the performance of the fourth-order FVM in the table, together with the grid point requirement, we can conclude that for all the levels of accuracy considered in this paper (0.1 - 3%), FSM can deliver a solution 2.8-times faster than the fourth-order FVM. Coupled with the improvement factor of the FVM, the sixthorder FSM is 28X faster than the classical second-order schemes, at the same level of accuracy. This result is obtained with a sixth-order dealiasing.

When one starts a numerical investigation, it is useful to know how many grid points are needed and how much CPUtime is needed. The above timing can be used as a rough guide to predict the runtime for the processor on the same class by using the number of million grid points per second (MPS). However, it is difficult to translate it to other processors. Thus, we need a relative performance index. In this table we list three performance indices: (i). Million Points per Second (MPS), (ii). MPS per TeraFlops of LINPACK 1000D ( $MPTF_{1000D}$ ) and (iii). MPS per TeraFlops of High-Performance LINPACK. The MPS is a simple measurement which is specific to a machine. In order to estimate it on other machines, we need to relate with a standard benchmark which is also available on the machines of interest. The first benchmark is a classic 1000D LINPACK [82] which is a standard FORTRAN code available publicly. However, the problem size is too small for current machines and the embedded code may not be fully optimized by the compiler. Thus, the number of floating points operation obtained by 1000D is a rather pessimistic estimation of the machine performance. The High-Performance LINPACK (HPL) [83], on the other hand, is highly dependent on the performance of the Mathematics library (BLAS and LAPACK). When the optimized libraries are used, the number obtained usually represents the best performance one can get out of the machine. We run both benchmarks on a single core of Intel Xeon 8168 (parallel threads disabled). The MPS is gradually reduced from 1.88 down to about half of this value on the finest grid. The logarithmic complexity is responsible for about 40% of the increase in the computing time and the rest is coming from the caching effects. On the first two grids, the data needed for the

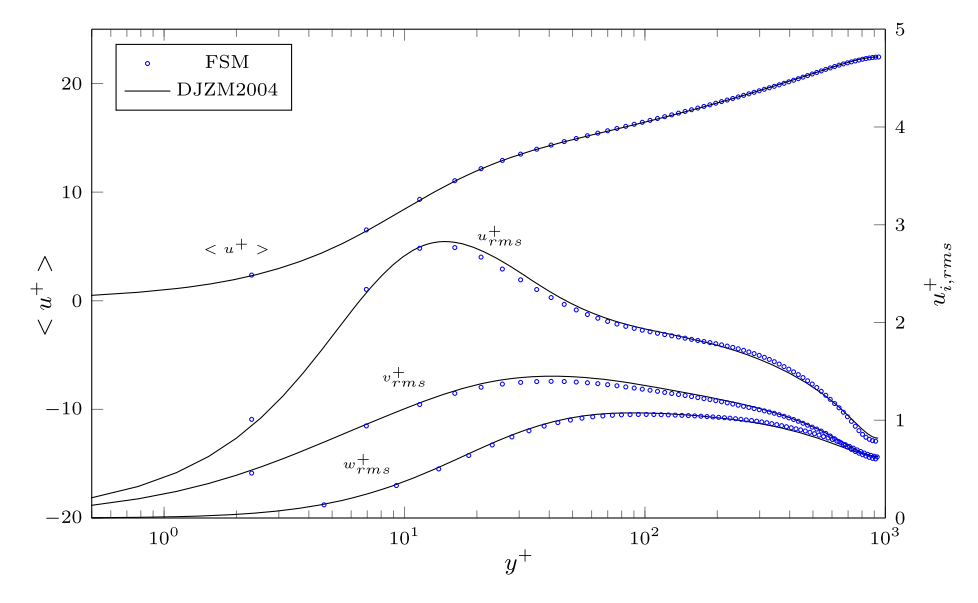


Fig. 21. Mean streamwise velocity and the RMS of velocities fluctuations on RE950 from the grid designed to meet 1% error in the mean profile:  $[\triangle x^+, \triangle y^+_{wall}, \triangle y^+_{max}, \triangle z^+] = [34.5, 4.7, 27.1, 12.6]$ . The grid density used here is 42.5 less dense than the reference.

compact scheme can stay on the level 2 cache, and other variables used in the momentum and the pressure calculation can be fitted within the level 3 cache, thus the performance is very good. On the finest grid, the level 3 cache can barely contain the two arrays used in the compact scheme. Therefore the performance drops a lot compared to the rest. The 1000D achieves about 6.3 GFlops while the HPL peaks at 91.3 GFlops with the leading dimension 20,480 on a single core. Therefore, the index  $MPTF_{1000D}$  is higher. According to these indices, we could expect a machine having 1 TeraFlops (HPL) to complete a time-step of 10.0 - 20.6 million grid points in a second. The open question, however, is the performance on a massive parallel architecture.

#### 8.2. Friction Reynolds number 590 and 950

In this section we evaluate the error estimations (Eq. (66)) when applied to higher Reynolds numbers:  $Re\tau = 590$  and 950, denoted as RE590 and RE950, respectively The forcing and the methods are the same as the previous case. The nominal forcing is set to  $Re_{\tau} = 587.19$  and 935.0 to match the exact Reynolds number in the references [74,77]. The computational domains on RE590 case is set to the same one used in the reference [74]. The spanwise width on RE950 is shortened to save the computing time. Del Alamo et al. [77], conducted numerical experiments on two domains. The large domain is  $8\pi H$  long (streamwise) and  $3\pi H$  wide (spanwise) and the smaller domain is  $\pi H$  long and  $\pi H/2$  wide. According to their data, the spanwise width of the smaller domain is quite close to the necessary length, but the streamwise length is too short. This too small domain cannot produce the correct turbulent shear stress and results in a wrong mean profile. Our previous study shows that the domain four-times larger  $(2\pi \times \pi)$  than the smaller domain is sufficient to capture the flow statistics of RE950 accurately. The result from this domain shows that the autocorrelations in the spanwise direction are close to zero at  $\pi H/2$  except near the center where shear stresses are very low. Li and Tsubokura [84] used this narrow spanwise width  $(\pi H/2)$  and obtained a very good agreement with the larger domain in the reference [77]. Thus, we set the streamwise-spanwise domain to  $(2\pi \times \pi)$  for RE590 matching to the reference, but reduce it to  $\pi H/2$  on RE950. Due to the faster decay of the autocorrelations, this domain is large enough to compare a 1% difference in the firstand second-order statistics.

We designed two grids such that the resolutions are close to the 1%-margin developed earlier. The effective grid resolutions  $[\triangle x^+, \triangle y^+_{wall}, \triangle y^+_{max}, \triangle z^+]$  are [29.0, 4.7, 29.4, 12.9] and [34.5, 4.7, 27.1, 12.6] with the total number of cells equal to 1.47M(RE590) and 2.67M(RE950). The actual mean flow variables obtained on RE590 are  $Re_b = 21,874$  (21,609),  $Re_{\tau} = 590.35$  (587.19),  $u_{\tau}/u_{\tau} = 21.05$  (21.26),  $u_{h}/u_{\tau} = 18.40$  (18.65). The numbers in the parentheses are processed from the reference data [74]. The mean flow parameters are well within a 1% error. The maximum and the average of the local relative errors in the time-averaged profile w.r.t. the filtered DNS solution are 2.1% and 1.4%, respectively. This is in line with the previous behavior on RE180 with the  $64^3$ -grid. Note that the local errors here are defined as  $\left|\left(u_{fsm}(y)-u_{ref}(y)\right)/u_{ref}(y)\right|$ . The large errors are observed within the viscous sublayer and the buffer layer. Outside, they are almost constant at the level close to the average error. We plot the mean profile and the RMS of the fluctuations for RE950 in Fig. 21 for visual inspection. Note that the grid density  $(N_t/(L_xL_yL_z))$  used in this case is 42.5-times less dense than the reference's grid. Here we reverted the symbol and the lines designations. The open circle symbols now belong to FSM and the solid line is the reference. This is done to highlight that this grid only has 3 cells before the peak of the

A. Hokpunna et al. / Journal of Computational Physics ••• (••••) •••••

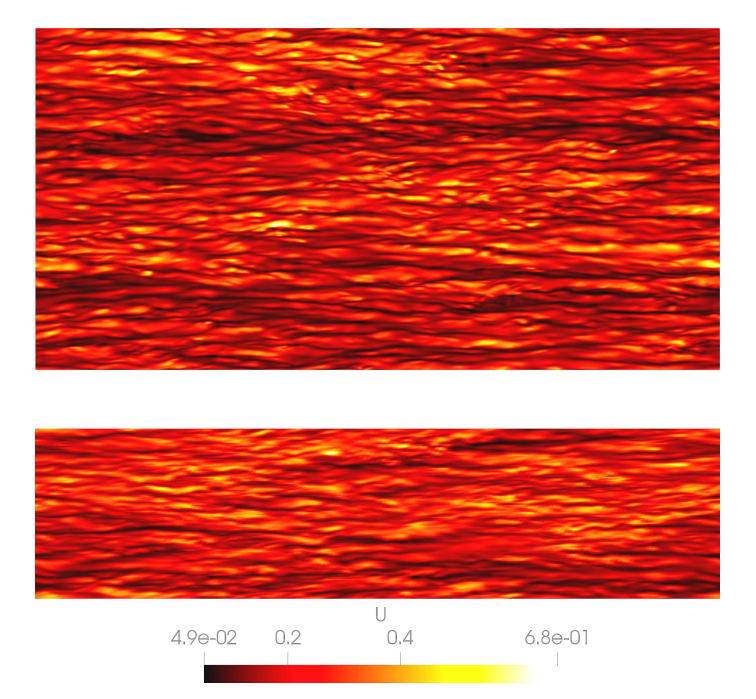


Fig. 22. A snapshot of u-contour at  $5y^+$  from RE950 (bottom) compared to the result from FVM on a larger domain (top). Similar structures can be seen on both simulations despite FSM having a grid density 11.4-times less. Note that the size of the wall cell with FSM simulation is  $4.7y^+$  and this plane is just above the top of this cell.

 $u_{rms}$ . Note that in the graph, u and v are positioned differently. The first point of u and v are at the center of the first cell  $(2.34y^+)$  while the first point of  $w_{rms}$  is located at the top of the first cell  $(4.68y^+)$ . The figure indicates that the profiles on this tailored grid follow the reference solution closely. Next, we consider a snapshot of the wall-normal plane ( $y^+=5$ ) in Fig. 22 along with the result from the fourth-order FVM [44]. The FSM on the smaller domain produces similar structures as obtained on the larger domain having 61.4M cells.

In comparison to other methods, Li and Tsubokura [84] solve the truncated compressible NSE [84] on 10.5M-grid using a low-Mach-fix for Roe's approximation [85] and their automatic dissipation adjustment model (ADA). The simulation there without ADA is much less accurate than the present work while the solution with ADA has a comparable accuracy. The mean profile here is comparable to an implicit LES based on DGM [86] with 3.5M DOFs ( $2\pi \times \pi$  domain), but the RMS profiles here are more accurate. Thus, our coarse DNS results are on par with some higher-order large-eddy simulations, without using any turbulence modeling, numerical damping, penalty terms or the direct filtering to the velocities.

#### 9. Conclusion and outlook

We have presented a new discretization aiming specially at coupled conservation problems. The discretization conserves the discrete mass analytically. Its high resolving power is a result of the spatial arrangement of the discrete variables which allows the analytical mass flux calculation. Formally, this method asymptotically halves the size of the stencil of the Laplacian for the projection method. The sixth-order compact schemes for convection and diffusion terms are validated together with three pressure treatments. The explicit fourth-order pressure treatment is sufficient to deliver the apparent sixth-order convergence rate. Consequently, the sixth-order FSM can use the 13-point Laplacian stencil, instead of the 31point.

The grid resolutions needed to obtain a 1%-error in the mean profile of turbulent channel flow simulation are  $[\triangle x^+, \triangle y^+_{wall}, \triangle y^+_{max}, \triangle z^+] = [30, 4, 30, 11]$ , for the proposed method. At high Reynolds numbers, this resolution translates to total grid points of  $(Re_{\tau}/22)^3$  per cubic of channel half-width  $(H^3)$ . When the grid resolutions are the same as the spectral solutions, the predictions are as good as the other spectral schemes. In terms of accuracy, the sixth-order FSM should not differ much from other sixth-order methods. However, in terms of performance, FSM should be faster than FVM and FDM. Two performance indices of the NSE solvers: the 1%-error resolutions and the  $MPTF_{HPL}$  are proposed.

The finite surface discretization itself is a natural spatial discretization that sits between FVM and FDM. For coupled conservation problems, FSM is very competitive. The mass conservation equation in FSM is exact and it only approximates the momentum equations. Other coupled problems such as Magnetohydrodynamics and scalar transport should be greatly benefited from the FSM as well. The conserved quantities (mass, chemicals, magnetic fields) can be defined on the controlled volume while the transporting variables (momentums, velocities, ion fluxes) can live on the surface of the controlled volume.

a

[m3G; v1.292; Prn:27/08/2020; 7:19] P.33 (1-36)

The surface-averaged flux can serve as a new type of DOF for existing methods. Effectively, a sixth-order FSM can deliver a comparable solution 28-times faster than the second-order FVM.

It would be interesting to extend FSM to other coordinate systems including curvilinear coordinates, or apply it to nonorthogonal and unstructured grids. To enable the full potential of the discretization, a time integration method should be more accurate than the third-order Runge-Kutta. The current dealiasing filter costs about 42% of the convection. A more efficient filter is needed to improve the overall performance of the scheme. Lastly, the method has been run in serial. For large-scale turbulent simulations, effective methods for solving systems of the compact stencil on massively parallel computer need to be implemented.

#### **CRediT authorship contribution statement**

**Arpiruk Hokpunna:** Conceptualization, Methodology, Coding, Investigation, Visualization, Writing - original draft preparation, Review & Editing. Takashi Misaka: Conceptualize, Methodology, Discussion. Shigeru Obayashi: Conceptualization & Resources. Somchai Wongwises: Review & editing. Michael Manhart: Conceptualization, Discussion, Review & Editing.

#### **Declaration of competing interest**

The authors declare that they have no known competing financial interests or personal relationships that could have appeared to influence the work reported in this paper.

#### Acknowledgements

This research is partially funded by Thailand Research Fund under contract number MRG 5380279. The later part of this research is partially funded by Chiang Mai University under the center of excellence scheme and the Institute of Fluid Science, Tohoku University under Collaborative Research Project No. 116078. The first author would like to thank Prof. Feng Xiao from Tokyo Institute of Technology, for comments during the preparation of the manuscript and answering questions on multi-moment and active fluxes methods. The first author thanks Thailand National e-Science Infrastructure Consortium for providing computing facility.

#### References

- [1] S.K. Lele, Compact finite difference schemes with spectral-like resolution, J. Comput. Phys. 103 (1) (1992) 16-42.
- [2] A. Hokpunna, M. Manhart, Compact fourth-order finite volume method for numerical solutions of Navier-Stokes equations on staggered grids, J. Comput. Phys. 229 (20) (2010) 7545-7570, https://doi.org/10.1016/j.jcp.2010.05.042.
- X. Liu, L. Xuan, Y. Xia, H. Luo, A reconstructed discontinuous Galerkin method for the compressible Navier-Stokes equations on three-dimensional hybrid grids, Comput. Fluids 152 (2017) 217-230, https://doi.org/10.1016/j.compfluid.2017.04.027.
- [4] R. Knikker, Study of a staggered fourth-order compact scheme for unsteady incompressible viscous flows, Int. J. Numer. Methods Fluids 59 (2009) 1063-1092.
- N.A. Kampanis, J.A. Ekaterinaris, A staggered grid, high-order accurate method for the incompressible Navier-Stokes equations, J. Comput. Phys. 215 (2) (2006) 589-613.
- T. Hashimoto, I. Tanno, T. Yasuda, Y. Tanaka, K. Morinishi, N. Satofuka, Higher order numerical simulation of unsteady viscous incompressible flows using kinetically reduced local Navier-Stokes equations on a GPU, Comput. Fluids 110 (2015) 108-113, https://doi.org/10.1016/j.compfluid.2014.09.013, parCFD 2013.
- G. Kozyrakis, A. Delis, N. Kampanis, A finite difference solver for incompressible Navier-Stokes flows in complex domains, Appl. Numer. Math. 115 (2017) 275-298, https://doi.org/10.1016/j.apnum.2016.07.010.
- B. Cockburn, G.E. Karniadakis, C.-W. Shu, Discontinuous Galerkin Methods: Theory, Computation and Applications, 1st edition, Springer Publishing Company, Incorporated, 2011.
- L. Jameson, High order schemes for resolving waves: number of points per wavelength, J. Sci. Comput. 15 (4) (2000) 417-439, https://doi.org/10.1023/A: 1011180613990.
- [10] F. Schwertfirm, J. Mathew, M. Manhart, Improving spatial resolution characteristics of finite difference and finite volume schemes by approximate deconvolution pre-processing, Comput. Fluids 37 (9) (2008) 1092-1102, https://doi.org/10.1016/j.compfluid.2007.06.005.
- J. Gullbrand, An evaluation of a conservative fourth order DNS code in turbulent channel, Tech. rep., Center for Turbulence Research, Stanford University,
- [12] O. Shishkina, C. Wagner, A fourth order finite volume scheme for turbulent flow simulations in cylindrical domains, Comput. Fluids 36 (2) (2007)
- [13] A. Meri, H. Wengle, A. Dejoan, E. Védy, R. Schiestel, Applications of a 4th-Order Hermitian Scheme for Non-equidistant Grids to LES and DNS of Incompressible Fluid Flow, Springer, Berlin, Germany, 1998, pp. 110-127.
- [14] A.J. Chorin, Numerical solution of the Navier-Stokes equations, Math. Comput. 22 (104) (1968) 745-762, https://doi.org/10.2307/2004575.
- [15] J. Kim, P. Moin, Application of a fractional-step method to incompressible Navier-Stokes equations, J. Comput. Phys. 59 (2) (1985) 308-323, https:// doi.org/10.1016/0021-9991(85)90148-2.
- [16] R.V. Wilson, A.O. Demuren, Higher-order compact schemes for numerical simulation of incompressible flows, part II: applications, Numer. Heat Transf., Part B, Fundam, 39 (2001) 231-255.
- [17] A.O. Demuren, R.V. Wilson, M. Carpenter, Higher-order compact schemes for numerical simulation of incompressible flows, part I: theoretical development, Numer. Heat Transf., Part B, Fundam. 39 (3) (2001) 207-230.
- B.J. Boersma, A 6th order staggered compact finite difference method for the incompressible Navier-Stokes and scalar transport equations, J. Comput. Phys. 230 (12) (2011) 4940-4954, https://doi.org/10.1016/j.jcp.2011.03.014.
- [19] M. Piller, E. Stalio, Finite-volume compact schemes on staggered grids, J. Comput. Phys. 197 (1) (2004) 299-340.

A. Hokpunna et al. / Journal of Computational Physics ••• (••••) •••••

- [20] M. Meinke, W. Schroeder, E. Krause, T. Rister, A comparison of second- and sixth-order methods for large-eddy simulations, Comput. Fluids 31 (2002) 695–718 (24).
- [21] R. Hu, L. Wang, P. Wang, Y. Wang, X. Zheng, Application of high-order compact difference scheme in the computation of incompressible wall-bounded turbulent flows, Computation 6 (2) (2018), https://doi.org/10.3390/computation6020031.
- [22] W. Rojanratanangkule, A. Hokpunna, Performance of high-order schemes on collocated and staggered grids, J. Res. Appl. Mech. Eng. 3 (1) (2015) 22-28.
- [23] V. Marcel, Y. Maurice, Finite-surface method for the Maxwell equations in generalized coordinates, in: Aerospace Sciences Meetings, American Institute of Aeronautics and Astronautics, 1993, https://doi.org/10.2514/6.1993-463.
- [24] M. Vinokur, M. Yarrow, Finite-surface method for the Maxwell equations in generalized coordinates, https://arc.aiaa.org/doi/abs/10.2514/6.1993-463.
  - [25] J. Fang, Finite-surface method for solving RCS problems of arbitrary cross-section PEC cylinder coated with dielectric medium, in: 1999 International Conference on Computational Electromagnetics and Its Applications, Proceedings, ICCEA '99, 1999, pp. 581–584.
  - [26] R. Tramel, M. Turowski, A. Przekwas, J. Schultz, R. Frey, Modeling of electromagnetic fields in high speed electronic interconnects using a least squares FD-TD algorithm, in: Technical Proceedings of the 2001 International Conference on Modeling and Simulation of Microsystems, 2001, pp. 602–605, www.nstj.org/proces/MSM2001/12/T6708
  - [27] Kane Yee, Numerical solution of initial boundary value problems involving Maxwell's equations in isotropic media, IEEE Trans. Antennas Propag. 14 (3) (1966) 302–307.
  - [28] B.V. Leer, Towards the ultimate conservative difference scheme. IV. A new approach to numerical convection, J. Comput. Phys. 23 (3) (1977) 276–299, https://doi.org/10.1016/0021-9991(77)90095-X.
  - [29] T.A. Eymann, P.L. Roe, Multidimensional active flux schemes, https://arc.aiaa.org/doi/abs/10.2514/6.2013-2940.
  - [30] P.L. Roe, J.B. Maeng, D. Fan, Comparing active flux and discontinuous Galerkin methods for compressible flow, https://arc.aiaa.org/doi/abs/10.2514/6. 2018-0836.
  - [31] F. Xiao, Unified formulation for compressible and incompressible flows by using multi-integrated moments I: one-dimensional inviscid compressible flow, J. Comput. Phys. 195 (2) (2004) 629–654, https://doi.org/10.1016/j.jcp.2003.10.014.
  - [32] F. Xiao, R. Akoh, S. Ii, Unified formulation for compressible and incompressible flows by using multi-integrated moments II: multi-dimensional version for compressible and incompressible flows, J. Comput. Phys. 213 (1) (2006) 31–56, https://doi.org/10.1016/j.jcp.2005.08.002.
  - [33] B. Xie, F. Xiao, A multi-moment constrained finite volume method on arbitrary unstructured grids for incompressible flows, J. Comput. Phys. 327 (C) (2016) 747–778, https://doi.org/10.1016/j.jcp.2016.09.054.
  - [34] N. Nguyen, J. Peraire, B. Cockburn, A hybridizable discontinuous Galerkin method for Stokes flow, Comput. Methods Appl. Mech. Eng. 199 (9) (2010) 582–597, https://doi.org/10.1016/j.cma.2009.10.007.
  - [35] B. Cockburn, B. Dong, J. Guzmán, M. Restelli, R. Sacco, A hybridizable discontinuous Galerkin method for steady-state convection-diffusion-reaction problems, SIAM J. Sci. Comput. 31 (5) (2009) 3827–3846, https://doi.org/10.1137/080728810.
  - [36] J.P. Sheldon, S.T. Miller, J.S. Pitt, A hybridizable discontinuous Galerkin method for modeling fluid-structure interaction, J. Comput. Phys. 326 (2016) 91–114, https://doi.org/10.1016/j.jcp.2016.08.037.
  - [37] A.S. Almgren, J.B. Bell, W.Y. Crutchfield, Approximate projection methods: part I. Inviscid analysis, SIAM J. Sci. Comput. 22 (4) (2000) 1139-1159.
  - [38] S. Adjerid, M. Baccouch, The discontinuous Galerkin method for two-dimensional hyperbolic problems. Part I: superconvergence error analysis, J. Sci. Comput. 33 (1) (2007) 75–113, https://doi.org/10.1007/s10915-007-9144-x.
  - [39] A. Montlaur, S. Fernandez-Mendez, J. Peraire, A. Huerta, Discontinuous Galerkin methods for the Navier-Stokes equations using solenoidal approximations, Int. J. Numer. Methods Fluids 64 (5) (2010) 549-564, https://doi.org/10.1002/fld.2161.
  - [40] B. Klein, F. Kummer, M. Oberlack, A simple based discontinuous Galerkin solver for steady incompressible flows, J. Comput. Phys. 237 (2013) 235–250, https://doi.org/10.1016/j.jcp.2012.11.051.
  - [41] M. Tavelli, M. Dumbser, A staggered space–time discontinuous Galerkin method for the three-dimensional incompressible Navier–Stokes equations on unstructured tetrahedral meshes, J. Comput. Phys. 319 (2016) 294–323, https://doi.org/10.1016/j.jcp.2016.05.009.
  - [42] E. Ferrer, D. Moxey, R.H.J. Willden, S.J. Sherwin, Stability of projection methods for incompressible flows using high order pressure-velocity pairs of same degree: continuous and discontinuous Galerkin formulations, Commun. Comput. Phys. 16 (3) (2014) 817–840, https://doi.org/10.4208/cicp. 290114.170414a.
  - [43] M.H. Kobayashi, On a class of Pade finite volume methods, J. Comput. Phys. 156 (1) (1999) 137-180.
  - [44] A. Hokpunna, Compact fourth-order scheme for numerical simulations of Navier-Stokes equations, Dissertation, Technische Universität München, München, 2009.
  - [45] F. Bertagnolio, O. Daube, Three-dimensional incompressible Navier-Stokes equations on non-orthogonal staggered grids using the velocity-vorticity formulation, Int. J. Numer. Methods Fluids 28 (6) (1998) 917–943.
  - [46] T. Heister, M.A. Olshanskii, L.G. Rebholz, Unconditional long-time stability of a velocity-vorticity method for the 2D Navier-Stokes equations, Numer. Math. 135 (1) (2017) 143–167, https://doi.org/10.1007/s00211-016-0794-1.
  - [47] G. Pascazio, M. Napolitano, A staggered-grid finite volume method for the vorticity-velocity equations, Comput. Fluids 25 (4) (1996) 433–446, https://doi.org/10.1016/0045-7930(96)00004-7.
  - [48] H. Nishida, N. Satofuka, Higher-order solutions of square driven cavity flow using a variable-order multi-grid method, Int. J. Numer. Methods Eng. 34 (2) (1992) 637–653, https://doi.org/10.1002/nme.1620340215.
  - [49] E. Erturk, T.C. Corke, C. Gökçöl, Numerical solutions of 2-D steady incompressible driven cavity flow at high Reynolds numbers, Int. J. Numer. Methods Fluids 48 (7) (2005) 747–774, https://doi.org/10.1002/fld.953.
  - [50] J.M.C. Pereira, M.H. Kobayashi, J.C.F. Pereira, A fourth-order-accurate finite volume compact method for the incompressible Navier-Stokes solutions, J. Comput. Phys. 167 (1) (2001) 217–243.
  - [51] A.G. Kravchenko, P. Moin, On the effects of numerical errors in large eddy simulations of turbulent flows, J. Comput. Phys. 131 (1997) 310-322.
  - [52] Y. Morinishi, T.S. Lund, O.V. Vasilyev, P. Moin, Fully conservative higher order finite difference schemes for incompressible flow, J. Comput. Phys. 143 (1) (1998) 90–124.
- [53] O.V. Vasilyev, High order finite difference schemes on non-uniform meshes with good conservation properties, J. Comput. Phys. 157 (2) (2000) 746–761.
- 52 [54] R.W.C.P. Verstappen, A.E.P. Veldman, Symmetry-preserving discretization of turbulent flow, J. Comput. Phys. 187 (1) (2003) 343–368.
  - [55] P. Moin, Fundamentals of Engineering Numerical Analysis, 2nd edition, Cambridge University Press, 2010.
  - [56] A. Tyliszczak, High-order compact difference algorithm on half-staggered meshes for low Mach number flows, Comput. Fluids 127 (2016) 131–145, https://doi.org/10.1016/j.compfluid.2015.12.014.
  - [57] M.H. Carpenter, D. Gottlieb, S. Abarbanel, Time-stable boundary conditions for finite-difference schemes solving hyperbolic systems: methodology and application to high-order compact schemes, J. Comput. Phys. 111 (2) (1994) 220–236.
  - [58] A. Hokpunna, Compact fourth-order scheme for numerical simulations of Navier-Stokes equations, Ph.D. thesis, Hydromechanik, Technische Universität München, 2009.
  - [59] F.M. Denaro, On the application of the Helmholtz-Hodge decomposition in projection methods for incompressible flows with general boundary conditions, Int. J. Numer. Methods Fluids 43 (1) (2003) 43–69.
  - [60] H.L. Stone, Iterative solution of implicit approximations of multidimensional partial differential equations, SIAM J. Numer. Anal. 5 (3) (1968) 530–558, https://doi.org/10.1137/0705044, arXiv:https://doi.org/10.1137/0705044.

JID:YJCPH AID:109790 /FLA [m3G; v1.292; Prn:27/08/2020; 7:19] P.35 (1-36)

A. Hokpunna et al. / Journal of Computational Physics ••• (••••) •••••

[61] J.H. Williamson, Low-storage Runge-Kutta schemes, J. Comput. Phys. 35 (48) (1980) 48-56.

a

0

- [62] D.L. Brown, Performance of under-resolved two-dimensional incompressible flow simulations, J. Comput. Phys. 122 (1) (1995) 165-183.
- [63] S. Chakravorty, I. Mathew, A high-resolution scheme for low Mach number. Int. I. Numer. Methods Fluids 46 (3) (2004) 245-261.
  - [64] M. Malik, T. Zang, M. Hussaini, A spectral collocation method for the Navier-Stokes equation, J. Comput. Phys. 61 (1985) 64-88.
  - [65] M.M. Rai, P. Moin, Direct simulation of turbulent flow using finite-difference schemes, I. Comput. Phys. 96 (1991) 15-53.
  - [66] G. Alfonsi, G. Passoni, L. Pancaldo, D. Zampaglione, A spectral-finite difference solution of the Navier-Stokes equations in three dimensions, Int. J. Numer, Methods Fluids 28 (1) (1998) 129-142.
- [67] J.M.A. Das, Direct numerical simulation of turbulent spots, Comput. Fluids 30 (2001) 533-541, https://doi.org/10.1016/S0045-7930(01)00004-4.
  - [68] A. Kravchenko, P. Moin, R. Moser, Zonal embedded grids for numerical simulations of wall-bounded turbulent flows, J. Comput. Phys. 127 (2) (1996) 412-423, https://doi.org/10.1006/jcph.1996.0184.
  - [69] C. Canuto, M.Y. Hussaini, A. Quarteroni, T.A. Zang, Spectral Methods: Fundamentals in Single Domains (Scientific Computation), 1st edition, Springer,
  - [70] T.A. Driscoll, N. Hale, L.N. Trefethen, Chebfun Guide, First edition, 2014, https://www.chebfun.org/docs/guide/chebfun\_guide.pdf
  - [71] C.-H. Bruneau, M. Saad, The 2D lid-driven cavity problem revisited, Comput. Fluids 35 (3) (2006) 326-348, https://doi.org/10.1016/j.compfluid.2004.12.
  - [72] S.S. Patwardhan, O.N. Ramesh, Scaling of pressure spectrum in turbulent boundary layers, J. Phys. Conf. Ser. 506 (1) (2014) 012011, http://stacks.jop. org/1742-6596/506/i=1/a=012011.
  - [73] J. Kim, P. Moin, R.D. Moser, Turbulence statistics in fully developed channel flow at low Reynolds number, J. Fluid Mech. 177 (1987) 133-166.
  - [74] R. D. Moser, J. Kim, N. N. Mansour, Direct numerical simulation of turbulent channel flow up to  $Re_{\tau}$  = 590, Phys. Fluids 11 (1) (1999) 943–945.
  - [75] Z.W. Hu, Wall pressure and shear stress spectra from direct simulations of channel flow, AIAA J. 44 (7) (2006) 1541-1549.
  - [76] A.W. Vreman, J.G.M. Kuerten, Comparison of direct numerical simulation databases of turbulent channel flow at  $Re_{\tau}$  = 180, Phys. Fluids 26 (1) (2014) 015102, https://doi.org/10.1063/1.4861064.
  - J.C. Del Álamo, J. Jiménez, P. Zandonade, R.D. Moser, Scaling of the energy spectra of turbulent channels, J. Fluid Mech. 500 (2004) 135-144, https:// doi.org/10.1017/S002211200300733X.
  - P. Sagaut. Large-Eddy Simulation for Acoustics, thirteenth edition, 2007, pp. 89–127.
  - B. Krank, N. Fehn, W.A. Wall, M. Kronbichler, A high-order semi-explicit discontinuous Galerkin solver for 3D incompressible flow with application to DNS and LES of turbulent channel flow, I. Comput. Phys. 348 (2017) 634-659, https://doi.org/10.1016/j.icp.2017.07.039.
  - S. Laizet, E. Lamballais, High-order compact schemes for incompressible flows: a simple and efficient method with quasi-spectral accuracy, J. Comput. Phys. 228 (2009) 5989-6015, https://doi.org/10.1016/j.jcp.2009.05.010.
  - S. Rezaeiravesh, M. Liefvendahl, Effect of grid resolution on large eddy simulation of wall-bounded turbulence, Phys. Fluids 30 (5) (2018) 055106, https://doi.org/10.1063/1.5025131.
  - [82] J. Dongarra, P. Luszczek, A. Petite, The Linpack benchmark: past, present and future, Concurr. Comput. 15 (9) (2003) 803-820, https://doi.org/10.1002/ cpe.728.
  - [83] A. Petitet, J.D.R.C. Whaley, A. Cleary, HPL a portable implementation of the high-performance Linpack benchmark for distributed-memory computers, www.netlib.org/benchmark/hpl. 2018.
  - C.-G. Li, M. Tsubokura, An implicit turbulence model for low-Mach Roe scheme using truncated Navier-Stokes equations, J. Comput. Phys. 345 (2017) 462-474, https://doi.org/10.1016/j.jcp.2017.05.032.
  - [85] F. Rieper, A low-Mach number fix for Roe's approximate Riemann solver, J. Comput. Phys. 230 (13) (2011) 5263-5287, https://doi.org/10.1016/j.jcp.
  - C. Carton de Wiart, K. Hillewaert, L. Bricteux, G. Winckelmans, Implicit LES of free and wall-bounded turbulent flows based on the discontinuous Galerkin/symmetric interior penalty method, Int. J. Numer. Methods Fluids 78 (2015), https://doi.org/10.1002/fld.4021.

Sponsor names

Do not correct this page. Please mark corrections to sponsor names and grant numbers in the main text.

**Thailand Research Fund**, country=Thailand, grants=MRG 5380279

Chiang Mai University, country=Thailand, grants=

Institute of Fluid Science, Tohoku University, country=Japan, grants=

Please cite this article in press as: A. Hokpunna et al., Finite surface discretization for incompressible Navier-Stokes equations and coupled conservation laws, J. Comput. Phys. (2020), https://doi.org/10.1016/j.jcp.2020.109790

Journal of Computational Physics ••• (••••) ••••••



## Contents lists available at ScienceDirect

# **Journal of Computational Physics**

www.elsevier.com/locate/jcp



### Graphical abstract

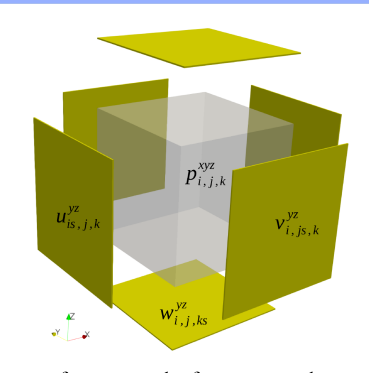
#### Finite surface discretization for incompressible Navier-Stokes equations and coupled conservation laws

Journal of Computational Physics ••••, •••,

Arpiruk Hokpunna<sup>a,b,\*</sup>, Takashi Misaka<sup>c</sup>, Shigeru Obayashi<sup>d</sup>, Somchai Wongwises<sup>e,f</sup>, Michael Manhart<sup>g</sup>

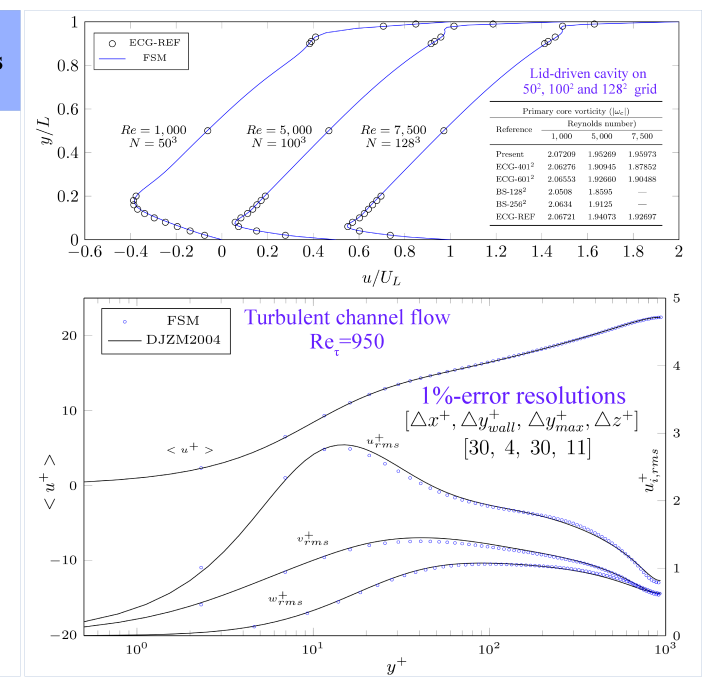
- a Department of Mechanical Engineering, Faculty of Engineering, Chiang Mai University (CMU), Chiang Mai 50200, Thailand
- <sup>b</sup> Advanced Research Center for Computational Simulation, Chiang Mai University (CMU), Chiang Mai 50200, Thailand
- <sup>c</sup> National Institute of Advanced Industrial Science and Technology (AIST), Tokyo 135-0064, Japan
- d Institute of Fluid Science, Tohoku University, Sendai 980-8577, Japan
- e Department of Mechanical Engineering, Faculty of Engineering, King Mongkut's University of Technology Thonburi (KMUTT), Bangkok 10140, Thailand
- <sup>f</sup> National Science and Technology Development Agency (NSTDA), Pathum Thani 12120, Thailand
- Fachbebiet Hydromechanik, Technische Universität München (TUM), München 80333, Germany

## Finite Surface Discretization for **Incompressible Navier-Stokes Equations** and Coupled Conservation Laws



Pressure surfaces store the face-averaged normal velocity.

- The mass balance is computed exactly.
- The projection Laplacian is most compact.
- 60 momentum can be used with 40 pressure.
- Runtime per grid point is the same as a fourth-order FVM



Please cite this article in press as: A. Hokpunna et al., Finite surface discretization for incompressible Navier-Stokes equations and coupled conservation laws, J. Comput. Phys. (2020), https://doi.org/10.1016/j.jcp.2020.109790

## Highlights

- The new finite-surface discretization conserves the exact discrete mass.
- The Laplacian from the projection method is smallest under this discretization.
- The sixth-order convergence rate can be achieved with an explicit fourth-order approximation of the pressure.
- The sixth-order FSM costs the same as a fourth-order FVM.
- FSM can match a fourth-order FVM solution using one-half number of total grid points.
- At the same level of accuracy, the proposed FSM is 28-times faster than the classic second-order FVM.

### 6 Research Outputs

### 1.International Journal Publication

A. Hokpunna, T. Misaka, S. Obayashi, S. Wongwises, M. Mahart. *Finite surface discretization for incompressible Navier-Stokes equations and coupled conservation laws*. Journal of Computational Physics (in Press).

#### 2.International Conference

A. Hokpunna. SIP-Multigrid method in Fourth-Order Finite Volume Method for Navier-Stokes Equations. International Conference on Computational Methods (ICCM2012), Gold Coast, Australia

A. Hokpunna, T. Misaka, S. Obayashi. *Development of two dimensional Finite Surface Discretizationfor Fluid Flows.*The 7th International Conference on Advanced Computational Methods in Engineering 2017, Ghent University, Ghent, Belgium

#### 3.Computer Software

1.FSM-FLOW: A scalable finite surface method for direct numerical simulation of fluid flow

# <u>แบบสรุปปิดโครงการวิจัย (จัดทำแยกต่างหากจากรายงานฉบับสมบูรณ์)</u>

<b>สัญญาเลขที่</b> MRG5380279 <b>ชื่อโครงการ</b> การวิเคราะห์พลศาสตร์ของการไหลและการถ่ายเทความร้อนในการไหลแบบ
ปั่นป่วนในท่อที่มีลอนภายในโดยใช้แบบจำลองแบบลาร์จอ้ดดี้ <b>หัวหน้าโครงการ ดร.อาภิรักษ์ หกพันนา หน่วยงาน</b>
มหาวิทยาลัยเทคโนโลยีพระจอมเกล้าธนบุรี <b>โทรศัพท์</b> 02-470-9122 <b>โทรสาร 02-470-9111 อีเมล์</b> arpiruk@gmail.com
สถานะผลงาน 🔲 ปกปิด 🗹 ไม่ปกปิด

# ความสำคัญ / ความเป็นมา

.การถ่ายเทความร้อนภายในท่อของอุปกรณ์แลกเปลี่ยนความร้อน (heat exchanger) เป็นปัญหาพื้นฐานที่มีความสำคัญต่ออุตสาหกรรม หลายๆชนิด อาทิเช่น เครื่องปรับอากาศ เครื่องทำความเย็น อุปกรณ์ถ่ายเทความร้อน อุตสาหกรรมการกลั่นน้ำมัน และอุตสาหกรรม อาหาร ในปี 2551 การส่งออกของอุตสาหกรรมเครื่องปรับอากาศและเครื่องทำความเย็นของไทยมีมูลค่ากว่า 140,000 ล้านบาท [1] และมีการส่งออกเป็นอันดับสองของโลก [2] การถ่ายเทความร้อนภายในท่อเป็นปัจจัยหนึ่งที่มีความสำคัญอย่างยิ่งในการกำหนดขนาด และประสิทธิภาพของอุปกรณ์แลกเปลี่ยนความร้อน หากการถ่ายเทความร้อนดังกล่าวสามารถทำได้อย่างมีประสิทธิภาพ ขนาดของ อุปกรณ์ก็จะสามารถลดลงได้ ซึ่งนำไปสู่การลดค่าใช้จ่าย และพลังงานที่ใช้ในการผลิต รวมไปถึงพลังงานที่ใช้ในการขับเคลื่อนสารทำความ เย็น การเพิ่มความสามารถในการถ่ายเทความร้อนภายในท่อจึงมีความสำคัญอย่างยิ่งต่อความสามารถในการแข่งขันของอุตสาหกรรม ปรับอากาศและเครื่องทำความเย็น และอุตสาหกรรมเกี่ยวเนื่องต่างๆ ของไทย

# วัตถุประสงค์ของโครงการ

- 1. เพื่อศึกษาพลศาสตร์ของไหลแบบแยกชั้น (laminar flow) และการไหลแบบปั่นป่วน (turbulent flow) ภายในท่อที่มีลอน ภายใน
- 2. เพื่อศึกษาความไม่เสถียร (instabilities) และโครงสร้างภายในการไหล (flow structure) อันนำไปสู่การลดความหนาของชั้น ขอบ (boundary layer) ซึ่งเป็นปัจจัยสำคัญในการเพิ่มความสามารถถ่ายเทความร้อนในท่อที่มีลอนภายใน
- 3. เพื่อศึกษากลไกการถ่ายเทความร้อนสู่ของไหลภายในท่อที่มีลอนภายใน แบบหนึ่งสถานะและแบบสองสถานะ
- 4. เพื่อพัฒนาระเบียบวิธีสำหรับการจำลองการไหลแบบปั่นป่วนที่มีประสิทธิภาพ

#### ผลการวิจัย

จากผลการวิจัยตลอดโครงการนั้น ผู้ทำการวิจัยได้พัฒนาเทคนิคด้านการจำลองเชิงตรง (Direct Numerical Simulation) เพื่อการ จำลองการถ่ายเทความร้อนในท่อทรงขรุขระ โดยมีความก้าวหน้าทางวิชาการดังนี้

- 1. ระเบียบวิธีการถ่ายเทความร้อนและมวลด้วยวิธีไฟในต์โวลุ่มลำดับสูง
- 2. พัฒนาวิธี Multigrid สำหรับการแก้สมการ Poisson ที่เกิดจากปัญหาทางการไหลแบบบีบอัดตัวไม่ได้
- 3. สร้างวิธีการไฟในต์เซอร์เฟส สำหรับการจำลองสมการคู่ควบ

โดยโครงสร้างด้านระเบียบวิธีเชิงตัวเลขที่สร้างขึ้น สามารถนำไปใช้แก้ปัญหาการถ่ายเทความร้อนในรูปทรงต่างๆ ได้ทันที และ ระเบียบ วิธีไฟในต์เซอร์เฟส (FSM) นั้น เป็นวิธีการจำลองแบบใหม่ ที่มีศักยภาพในการเข้ามาแทนที่ระเบียบวิธีไฟในต์โวลุ่ม (FVM) ได้ ซึ่งเมื่อ เปรียบเทียบระหว่าง วิธี FSM ความแม่นยำลำดับ 6 ที่พัฒนาขึ้นในโครงการวิจัยนี้ กับ ระเบียบวิธีไฟในต์โวลุ่ม ความแม่นยำลำดับ 4 ที่ ผู้วิจัยพัฒนาขึ้นระหว่างศึกษาปริญญาเอก นั้น ระเบียบวิธี FSM นี้ จะใช้เวลาการคำนวณใกล้เคียงกับวิธี FVM แต่เนื่องจากระเบียบวิธี FSM มีความแม่นยำสูงกว่า ทำให้ต้องการ กริด เพียง ครึ่งเดียวของ วิธี FVM ระเบียบวิธี FSM จึงให้การจำลองที่มีความแม่นยำเท่ากัน เร็วกว่า 2.8 เท่า และใช้ทรัพยากรการคำนวน (แกนการคำนวณ หน่วยความจำ) เพียงครึ่งเดียว ซึ่งทำให้สามารถทำการจำลองที่เลขเรย์ โนลดส์ และ เลขชมิดท์ สูง มีความเป็นไปได้ในทรัพยากรการคำนวณที่จำกัดของไทย

ผลวิจัย ต่อเนื่องจากโครงการนี้พบว่าการจัดการ aliasing error ที่เกิดใน convection term จะช่วยเพิ่มประสิทธิภาพการจำลองจาก 2.8 เท่า ขึ้นไปถึง ประมาณ 80 เท่า เมื่อเทียบกับซอฟท์แวร์การจำลองเดิมที่ใช้ ณ มหาวิทยาลัยเทคโนโลยีแห่งมิวนิก (Technische Universität München) ดังนั้นระเบียบวิธีที่พัฒนาขึ้นในโครงการวิจัยนี้ สามารถ เพิ่มความเร็วในการจำลองได้อย่างมาก ซึ่งจะช่วยให้ วิทยาการด้านการจำลองเชิงตัวเลของไทย ก้าวหน้าได้ทัดเทียมกับต่างประเทศ ถึงแม้ว่าทรัพยากรด้านการจำลองจะต่างกันอย่างมาก การขายยผลของระเบียบวิธีไฟในต์เซอรเฟส ไปยังสมการอนุพันธุ์คู่ควบอื่นๆ จะช่วยเพิ่มผลกระทบของงานวิจัยนี้ และ ช่วยพัฒนา เทคโนโลยีการจำลองเชิงวิทยาศาสตร์ วิศวกรรม และ อุตสาหกรรมของไทย และ ของโลกให้ก้าวหน้าไปอีกระดับ

การถ่ายเทความร้อนในท่อ, การจำลองลาร์จเอ้ดดี้, ระเบียบวิธีไฟไนต์โวลุ่ม, ระเบียบวิธีลำดับสูง, ระเบียบวิธีไฟไนต์เซอร์เฟส
o മ <b>യ    തു യ</b>    <b>マ</b> රු o o w
การนำผลงานวิจัยไปใช้ประโยชน์ (ดูคำจำกัดความ และตัวอย่างด้านหลังแบบฟอร์ม)
☑ ด้านวิชาการ โดยใคร Prof. Michael Manhart from TU-Muenchen, Germany
มีการนำไปใช้อย่างไร
มีการวางแผนและเตรียมข้อเสนอโครงการวิจัย ในการนำผลจากงานวิจัยนี้ไปขยายผลให้สามารถทำงานบนเครื่องซุปเปอร์คอมพิวเตย
ขนาดใหญ่ได้ เพื่อทำการวิจัยด้านการไหลและการถ่ายเทความร้อนต่อไป
<ul> <li>ยังไม่มีการนำไปใช้ (โปรดกรอกในกรอบถัดไป)</li> </ul>
<u>(กรณีที่ยังไม่มีการใช้ประโยชน์)</u> ผลงานวิจัยมีศักยภาพในการนำไปใช้ประโยชน์
🗆 ด้านนโยบาย 🗆 ด้านสาธารณะ 🗆 ด้านชุมชนและพื้นที่ 🗆 ด้านพาณิชย์ 🗆 ด้านวิชาการ
ข้อเสนอแนะเพื่อให้ผลงานถูกนำไปใช้ประโยชน์
การเผยแพร่/ประชาสัมพันธ์ (กรณาให้รายละเอียด พร้อมแนบหลักฐาน)
การเผยแพร่/ประชาสัมพันธ์ (กรุณาให้รายละเอียด พร้อมแนบหลักฐาน)  1. สิ่งพิมพ์ หรือสื่อทั่วไป
1. สิ่งพิมพ์ หรือสื่อทั่วไป
1. สิ่งพิมพ์ หรือสื่อทั่วไป
1. สิ่งพิมพ์ หรือสื่อทั่วไป ่ □ หนังสือพิมพ์ □ วารสาร □ โทรทัศน์ □ วิทยุ □ เว็บไซต์ □ คู่มือ/แผ่นพับ □ จัดประชุม/อบรม □ อื่น •
<ol> <li>สิ่งพิมพ์ หรือสื่อทั่วไป</li> <li>หนังสือพิมพ์  วารสาร  โทรทัศน์  วิทยุ  เว็บไซต์  คู่มือ/แผ่นพับ  จัดประชุม/อบรม  อี่น ง</li> <li>สิ่งพิมพ์ทางวิชาการ</li> <li>A. Hokpunna. SIP-Multigrid method in Fourth-Order Finite Volume Method for Navier-Stokes Equations.</li> </ol>
<ol> <li>สิ่งพิมพ์ หรือสื่อทั่วไป  □</li></ol>
<ol> <li>สิ่งพิมพ์ หรือสื่อทั่วไป</li> <li>ผนังสือพิมพ์ □ วารสาร □ โทรทัศน์ □ วิทยุ □ เว็บไซต์ □ คู่มือ/แผ่นพับ □ จัดประชุม/อบรม □ อื่น จัดประชุม/อบรม □ อี่น อี่น อี่น อี่น อี่น อี่น อี่น อี่น</li></ol>
<ol> <li>สิ่งพิมพ์ หรือสื่อทั่วไป</li> <li>□ หนังสือพิมพ์ □ วารสาร □ โทรทัศน์ □ วิทยุ □ เว็บไซต์ □ คู่มือ/แผ่นพับ □ จัดประชุม/อบรม □ อื่น จัดประชุม/อบรม □ อี่น อี่น อี่น อี่น อี่น อี่น อี่น อี่น</li></ol>
<ol> <li>สิ่งพิมพ์ หรือสื่อทั่วไป</li> <li>ผนังสือพิมพ์ □ วารสาร □ โทรทัศน์ □ วิทยุ □ เว็บไซต์ □ คู่มือ/แผ่นพับ □ จัดประชุม/อบรม □ อื่น จัดบระชุม/อบรม □ อี่น จัดบริชาการ</li> <li>สิ่งพิมพ์ทางวิชาการ</li> <li>1. A. Hokpunna. SIP-Multigrid method in Fourth-Order Finite Volume Method for Navier-Stokes Equations.</li> <li>The 4th International Conference on Computational Methods, 2012, Gold coast, Australia. Electronics</li> <li>Proceeding ISBN 978-1-921897-54-2.</li> <li>2. A. Hokpunna, T. Misaka, S. Obayashi. Development of two dimensional Finite Surface Discretizationfor</li> </ol>
<ol> <li>สิ่งพิมพ์ หรือสื่อทั่วไป</li> <li>ผนังสือพิมพ์ □ วารสาร □ โทรทัศน์ □ วิทยุ □ เว็บไซต์ □ คู่มือ/แผ่นพับ □ จัดประชุม/อบรม □ อื่น ๑</li> <li>สิ่งพิมพ์ทางวิชาการ</li> <li>A. Hokpunna. SIP-Multigrid method in Fourth-Order Finite Volume Method for Navier-Stokes Equations. The 4th International Conference on Computational Methods, 2012, Gold coast, Australia. Electronics Proceeding ISBN 978-1-921897-54-2.</li> <li>A. Hokpunna, T. Misaka, S. Obayashi. Development of two dimensional Finite Surface Discretization for Fluid Flows. The 7th International Conference on Advanced Computational Methods in Engineering, 2017</li> </ol>
<ol> <li>สิ่งพิมพ์ หรือสื่อทั่วไป</li> <li>ผนังสือพิมพ์ □ วารสาร □ โทรทัศน์ □ วิทยุ □ เว็บไซต์ □ คู่มือ/แผ่นพับ □ จัดประชุม/อบรม □ อื่น ข้าน ข้าน ข้าน ข้าน ข้าน ข้าน ข้าน ข้า</li></ol>